공학박사학위논문

Synthesis and Characterization of Ion-Conducting Polymers and Multifunctional Fillers for Lithium Rechargeable Battery Applications

이온 전도성 고분자와 다기능성 충진제의 합성과 분석, 그리고 리튬 이차 전지로의 응용

2017년 8월

서울대학교 대학원

화학생물공학부

심 지 민

Synthesis and Characterization of Ion-Conducting Polymers and Multifunctional Fillers for Lithium Rechargeable Battery Applications

by

Jimin Shim

Adviser: Professor Jong-Chan Lee, Ph. D.

Submitted in Partial Fulfillment
of the Requirements for the Degree of
DOCTOR OF PHILOSOPHY

August, 2017

School of Chemical and Biological Engineering
College of Engineering
Graduate School
Seoul National University

Abstract

Synthesis and Characterization of

Ion-Conducting Polymers and Multifunctional Fillers

for Lithium Rechargeable Battery Applications

심 지 민 **(Jimin, Shim)**

공과대학 화학생물공학과 **(Chemical and Biological Engineering)**

고분자 합성 전공 **(Polymer Synthesis)**

The Graduate School

Seoul National University

This study presents synthesis and characterization of ion-conducting polymers and multifunctional fillers, and their applications to polymer electrolytes for lithium rechargeable batteries. Firstly, organic/inorganic hybrid branched-graft copolymers comprising poly(ethylene glycol) methyl ether methacrylate (PEGMA) and methacrylisobutyl polyhedral oligomeric silsesquioxane (MA-POSS) were synthesized by reversible addition-fragmentation chain transfer (RAFT) polymerization and used as solid polymer electrolytes (SPEs). Linear-graft copolymers comprising PEGMA and MA-POSS were

also synthesized to study the effect of polymer structure on physical and electrochemical properties of the electrolytes. The SPEs maintained their dimensional stability and storage modulus even at elevated temperature due to reinforcing effect of the POSS. The SPE based on the organic/inorganic hybrid branched-graft copolymer exhibited an ionic conductivity of 1.6×10^{-4} S/cm at 60 ^{o}C, which is about three times higher than that of its linear-graft counterparts. It is attributed to free volume provided by the branched structure, resulting in good chain mobility.

Second, a series of branched polysiloxane derivatives containing ion-conducting poly(ethylene oxide) crosslinked by natural terpenes, limonene and geraniol, were synthesized by acid-catalyzed hydrolysis/condensation and thiol-ene click reaction and used as SPEs. The effects of structure of terpene crosslinker, physical state of the electrolytes, and morphology of lithium metal anode on various electrochemical properties of the SPEs were studied. The ionic conductivity of SPE having a linear geraniol crosslinker is higher than that of SPE having a cyclic limonene crosslinker, because linear structure of geraniol provides reduced steric hindrance compared to cyclic limonene with a ring strain. The combination of SPE and

lithium powder anode gives synergistic effect on cycle performance due to suppressed lithium dendrite growth.

Third, core-shell silica particles with ion-conducting poly(ethylene glycol) and anion-trapping boron moiety were prepared to be used as filler materials for the SPE. The effects of filler content and boron moieties on various physical and electrochemical properties of the SPEs were studied. The core-shell silica particles were found to improve mechanical strength and thermal stability of the polymer matrix. The boron moiety in the shell layer increases both ionic conductivity and lithium transference number, because lithium salt can be easily dissociated by the anion-trapping effect of the boron. Interfacial compatibility with lithium metal anode was also improved, because well-dispersed core-shell silica particles serve as a protective layer against interfacial side reaction.

Finally, perfluoropolyether (PFPE)-functionalized two-dimensional boron nitride (FBN) was prepared by sonication-assisted noncovalent functionalization and used as a multifunctional filler for gel polymer electrolyte (GPE). Pores are automatically generated by phase separation among polymer matrix, filler, and solvent even without addition of any porogen or non-solvent. By introducing a small

amount (0.5 wt%) of FBN into the GPE, ionic conductivity, lithium transference number, and mechanical modulus were significantly enhanced as compared to those of FBN-free GPE and conventional polyolefin separator. The formation and growth of lithium dendrites were effectively suppressed by the FBN and it is attributed to synergistic combination of the improved mechanical modulus and electrochemical properties, eventually resulting in excellent cycle performance. The GPE containing FBN exhibited unprecedentedly long short circuit time of 1940 h at a high current density of 1 mA cm^{-2}.

Keywords: lithium rechargeable battery, solid polymer electrolyte, gel polymer electrolyte, RAFT, polyhedral oligomeric silsesquioxane, terpenes, thiol-ene click reaction, lithium dendrite, core-shell silica, boron, boron nitride

Student Number: 2013-30986

TABLE OF CONTENTS

Chapter 3

Dendrite Suppression by Synergistic Combination of Solid Polymer Electrolyte Crosslinked with Natural Terpenes and Lithium Powder Anode for Lithium Metal Batteries

Chapter 4

Polymer Composite Electrolytes Having Core-Shell Silica Fillers with Anion-Trapping Boron Moiety in the Shell Layer for All-Solid-State Lithium-Ion Batteries

Chapter 5

Gel Polymer Electrolyte Containing 2D Boron Nitride Nanoflakes as a Multifunctional Additive for Safe Lithium Metal Batteries

List of Tables

List of Figures

Chapter 1

Introduction

1.1. Current Challenges of Lithium Rechargeable Batteries

Lithium rechargeable batteries have been intensively studied during several decades, because they are the most promising power sources for various applications including portable electronics, electric vehicles, and energy storage system.[1, 2] Despite the continuous developments from the first commercialization of lithium-ion batteries in 1991, present system comprising 'lithium metal oxide and carbon' based on intercalation mechanism cannot fulfill current requirements of high capacity and long cycle life of the battery system.[3] Among various progress in recent years in the development of next-generation lithium rechargeable battery system, utilization of electrode materials generating high capacity such as sulfur and oxygen has been received a great deal of attention.[4] Since lithium metal should be used for the source of lithium ion to introduce such unlithiated cathode materials, lithium metal batteries (LMBs), which utilize metallic lithium as the anode, have received considerable attention as an attractive alternative to conventional lithium-ion batteries for meeting the requirements of high performance of battery system.[5, 6]

Lithium metal, as the lightest metal among all the metallic elements, generates high theoretical capacity (3860 mAh/g) and lowest redox potential (-3.04 V *vs*. standard hydrogen electrode) compared to most of the other electrode materials, thereby achieving high energy density.[6] However, several disadvantages of the LMBs ascribed from the nature of lithium metal itself have hindered their practical applications in the energy systems.[6-8] Since the lithium metal is very reactive with almost all of the chemical species in battery components, inhomogeneous solid-electrolyte interphase (SEI) layer is easily formed on the lithium metal during cycling.[6-8] Furthermore, lithium dendrites are inevitably formed and grown on the surface of lithium metal, because current density is localized at the inhomogeneous SEI layer.[7] The lithium dendrites eventually penetrate through the separator immersed with liquid electrolyte leading to an internal short-circuit of the battery, thereby causing overheat and thermal runaway.[6-8]

1.2. Electrolytes in Lithium Rechargeable Batteries

To resolve the current challenges of the LMBs as aforementioned,

various strategies have been suggested for several decades. Among them, development of polymer electrolytes has been considered as very effective and promising approaches.[9] Until now, conventional liquid electrolytes comprising lithium salt and carbonate-based organic solvents have been generally used in commercialized battery system due to their high ionic conductivity at ambient condition. However, serious safety problems such as explosion and fire can be easily occurred when the liquid electrolytes are used, because the organic solvents have high volatility and flammability.[10, 11] Furthermore, polyolefin-based separators which should be introduced to physically separate the cathode and anode have a thermal shrinkage issues at elevated temperature, thereby eventually causing an internal short circuit.[12]

To overcome the drawbacks of current electrolyte system, solid polymer electrolytes (SPEs) based on ion-conducting poly(ethylene oxide) (PEO) derivatives have been intensively studied.[9] Since the Wright *et al*. discovered the ion conduction of PEO complexes with alkali metal salts, PEO derivatives have been utilized as representative lithium ion conducting materials in energy system.[13] Since the SPEs based on PEO derivatives do not contain any liquid components, good

safety even at elevated temperature can be ensured, thereby realizing the high-temperature applications such as electric vehicles and energy storage system.[9] However, PEO itself could not be directly utilized for practical applications due to its low ionic conductivity originating from suppressed segmental mobility of PEO in crystalline phase.[9] As a consequence, cycle performance of all-solid-state lithium rechargeable batteries containing the SPEs has not been satisfactory especially under high C-rate, possibly due to their low ionic conductivity and large interfacial resistance.

Gel polymer electrolytes (GPEs) comprising swollen polymer matrix by the liquid electrolyte have been suggested as alternatives for both liquid electrolyte and SPEs, because the GPEs combine the advantages of liquid electrolyte and SPEs such as reliable safety and reasonably high ionic conductivity.[14] Poly(methyl methacrylate) (PMMA), poly(acrylonitrile) (PAN), poly(vinylidene fluoride) (PVDF), and PEO have been used as polymer matrices for the GPEs, because the functional groups in these polymers interact with lithium ions and liquid electrolytes.[14] Since the “gel” state possesses both cohesive properties of the solid and diffusive properties of the liquid, GPEs exhibit higher ionic conductivity than the SPEs and greatly enhanced

safety than the liquid electrolytes. However, GPEs still have safety problems originating from the presence of liquid electrolytes.

1.3. Polymeric Materials for Electrolytes in Lithium Rechargeable Batteries

Among various strategies to develop the polymer electrolytes exhibiting good physical and electrochemical properties including mechanical stability, ionic conductivity, lithium transference number, and cycle performance, four main strategies will be introduced in the following.

1.3.1. Organic/Inorganic Hybrid Polymer Electrolytes Containing Polyhedral Oligomeric Silsesquioxane (POSS)

SPEs based on the PEO derivatives exhibit poor mechanical strength due to low glass transition temperature (T_g) of the PEO group.[9] Furthermore, comb-like or low molecular weight PEO derivatives cannot be directly used as the SPEs, because they are normally obtained as a waxy state due to the low T_g value.[15] To improve the

dimensional stability of the polymers having PEO derivatives, organic/inorganic hybrid polymers having polyhedral oligomeric silsesquioxane (POSS) have been suggested as polymer matrix for the SPEs.[16-18] POSS is a nano-sized organic/inorganic hybrid materials containing a silicon/oxygen framework functionalized with various organic groups at each corner (Figure 1.1), and has been widely used as a nanofiller for polymer composites due to its excellent mechanical strength.[19-21] POSS also provides additional free volume to the polymer matrix due to steric effect originating from its bulky structure, resulting in enhanced chain mobility of the polymers.[19, 22] There have been reports that dimensionally stable free-standing films can be obtained from copolymer having PEO and POSS side groups.[15-17] Furthermore, the T_g values of the polymers are not increased much with the incorporation of the POSS despite the rigid feature of the POSS due to the free volume effect.[15-17] Thus, it could be expected that the POSS in the SPEs maintain the chain mobility of the PEO segments as well as increase the overall mechanical strength. The mechanical stability

1.3.2. Crosslinked Polymer Electrolytes

Crosslinking technologies have been used in wide range of applications to improve the mechanical properties including insolubility, mechanical strength, stiffness, and rigidity of the polymers.[23] There are three types of crosslinking methods; chemical, physical, and biological crosslinking. Among them, chemical crosslinking methods by free radical or condensation have been developed for industrial scale due to the formation of stable crosslinked network by primary forces like covalent bonds compared to other methods.[23]

The poor mechanical stability of the PEO derivatives for the SPEs as well as ion-conducting polymer matrices for the GPEs can be also enhanced by introduction of the crosslinked structure. There have been reports on such crosslinked SPEs and GPEs exhibiting reasonable ionic conductivity and good mechanical stability.[24-27] However, ionic conductivity of the electrolytes continuously decreases with the increase in content of crosslinkers, because the increased crosslinking density decreases chain mobility of the ion-conducting segments.[28] Thus, it is important to find critical amount of crosslinkers that does not deteriorate the ion conduction as well as forms robust crosslinked network with good mechanical strength.

Meanwhile, there also have been trials to utilize the renewable resources from nature having unsaturated carbon-carbon bonds as cross-linkable moieties.[29-31] Although it is also desirable to use such natural resources as crosslinkers for the SPEs and GPEs to realize eco-friendly and low-cost battery system, such trials have not been reported many times in the field of energy system yet.

1.3.3. Polymer Composite Electrolytes Containing Filler Materials

Polymer composite electrolytes comprising polymer matrix and dispersed filler materials have been attracted considerable attention in that the introduction of filler materials improves both ionic conductivity and mechanical stability of the polymer matrix.[32] Furthermore, surface-functionalized filler materials can impart additional functionalities as well as enhance the dispersion behavior of the fillers. There have been reports on the polymer composite electrolytes containing inert inorganic fillers such as SiO_2, Al_2O_3, and TiO_2.[32-34] These inorganic fillers interact with the ion-conducting polymer matrix and the lithium salt by Lewis acid-base interactions through surface

functional groups such as hydroxyl and carboxyl moieties, which promote the dissociation of the lithium salt.[35] Moreover, mechanical stability is also reinforced by incorporating such inorganic fillers.[32] In addition, carbon-based fillers such as carbon nanotube (CNT) and graphene oxide (GO) were found to be effective to enhance the physical and electrochemical properties of the electrolytes.[36, 37] Especially in case of the electrolytes for LMBs, the fillers in the polymer composite electrolytes act as physical barrier against the formation and growth of lithium dendrites.[38] Moreover, they prevent further side reactions of reactive lithium metal anode, thereby forming stable SEI layer.[39] However, in most cases, introduction of large amount of fillers also sacrifices the ion-conducting properties, because aggregated fillers deteriorate the well-defined ion-conducting path.[36] Furthermore, mechanical properties might be also decreased with the filler content, because inhomogeneous dispersion of the fillers forms a mechanically weak domain.[38] Thus, there is optimum filler content to obtain the polymer composite electrolytes with high ionic conductivity and good mechanical strength.

1.3.4. Polymer Electrolytes Containing Anion-Trapping

Boron Moieties

Since boron has an empty p-orbital that can interact with basic anion of lithium salt, chemical additives having boron moieties have been known to increase lithium transference number (t_{Li+}) of the electrolyte system as shown in Figure 1.2.[40] The lithium transference number (t_{Li+}) is defined as relative amount of the lithium ion transport compared to that of the counter-anion, and the t_{Li+} value is considered as a critical parameter to expect the cycle performance.[41] Although the t_{Li+} value is desirable to be close to unity, most electrolytes have t_{Li+} values lower than 0.5 due to concentration polarization of ions during repetitive charge-discharge cycles, resulting in deterioration of long-term cycle performance.[42] The introduction of the boron moieties into the electrolytes can improve the electrochemical properties, because they effectively trap anions in the lithium salts through Lewis acid-base interaction between the vacant p orbital of the boron and basic anions of the lithium salt.[40] Furthermore, the boron moieties can also enhance electrochemical stability of the electrolytes by strong complexation between the boron and the anion retards the decomposition of the anion at high voltage.[43] Thus, a series of

researches have been reported to prepare polymers or low molecular weight compounds containing anion-trapping boron moieties as electrolytes or additive materials to improve electrochemical properties and cycle performance of the battery systems.[43-46]

1.4. Motivation

Based on the understanding of current challenges of lithium rechargeable battery systems and polymer electrolytes with various functionalities, we designed solid/gel types of polymer electrolytes based on organic/inorganic hybrid structure containing POSS, crosslinked structure by natural resources such as terpenes, polymer composites containing functionalized filler materials such as silica and boron nitride having boron moieties (Figure 1.3). The various derisable physical and electrochemical properties of the polymer electrolytes lead to realize safe and stable lithium metal battery system.

1.5. References

[1] N. S. Choi, Z. Chen, S. A. Freunberger, X. Ji, Y. K. Sun, K. Amine,

G. Yushin, L. F. Nazar, J. Cho and P. G. Bruce, *Angew. Chem. Int. Ed.* **2012**, 51, 9994-10024.

[2] V. Etacheri, R. Marom, R. Elazari, G. Salitra and D. Aurbach, *Energy Environ. Sci*. **2011**, 4, 3243-3262.

[3] B. Scrosati, J. Hassoun and Y. K. Sun, *Energy Environ. Sci*. **2011**, 4, 3287-3295.

[4] P. G. Bruce, S. A. Freunberger, L. J. Hardwick and J.-M. Tarascon, *Nat. Mater*. **2012**, 11, 19-29.

[5] K. Zhang, G. H. Lee, M. Park, W. J. Li and Y. M. Kang, *Adv. Energy Mater.* **2016**, *6*, 1600811.

[6] W. Xu, J. L. Wang, F. Ding, X. L. Chen, E. Nasybutin, Y. H. Zhang and J. G. Zhang, *Energy Environ. Sci.* **2014**, *7*, 513-537.

[7] X. B. Cheng, R. Zhang, C. Z. Zhao, F. Wei, J. G. Zhang and Q. Zhang, *Adv. Sci*. **2016,** *3*, 1500213.

[8] Z. Li, J. Huang, B. Y. Liaw, V. Metzler and J. B. Zhang, *J. Power Sources* **2014,** *254*, 168.

[9] Z. Xue, D. He and X. Xie, *J. Mater. Chem. A* **2015**, 3, 19218-19253.

[10] A. M. Stephan and K. S. Nahm, *Polymer* **2006**, 47, 5952-5964.

[11] W. H. Meyer, *Adv. Mater*. **1998**, 10, 439-448.

[12] H. Lee, M. Yanilmaz, O. Toprakci, K. Fu and X. Zhang, *Energy Environ. Sci*. **2014**, 7, 3857-3886.

[13] D. E. Fenton, J. M. Parker and P. V. Wright, *Polymer* **1973**, 14, 589.

[14] A. M. Stephan, *Eur. Polym. J*. **2006**, 42, 21-42.

[15] J. Shim, D.-G. Kim, J. H. Lee, J. H. Baik and J.-C. Lee, *Polym. Chem*. **2014**, 5, 3432-3442.

[16] D.-G. Kim, H.-S. Sohn, S.-K. Kim, A. Lee and J.-C. Lee, *J. Polym. Sci., Part A: Polym. Chem*. **2012**, 50, 3618–3627.

[17] S.-K. Kim, D.-G. Kim, A. Lee, H.-S. Sohn, J. J. Wie, N. A. Nguyen, M. E. Mackay and J.-C. Lee, *Macromolecules*, **2012**, 45, 9347-9356.

[18] H. J. Zhang, S. Kulkarni and S. L. Wunder, *J. Electrochem. Soc.* **2006**, 153, A239-A248.

[19] F. Wang, X. Lu and C. He, *J. Mater. Chem*. **2011**, 21, 2775-2782.

[20] B. H. Tan, H. Hussain, Y. W. Leong, T. T. Lin, W. W. Tjiu and C. B. He, *Polym. Chem*. **2013**, 4, 1250-1259.

[21] J. Pyun and K. Matyjaszewski, *Macromolecules* **2000**, 33, 217-220.

[22] J. Wu, T. S. Haddad and P. T. Mather, *Macromolecules* **2009**, 42,

1142-1152.

[23] S. Mane, S. Ponrathnam and N. Chavan, *Can. Chem. Trans*. **2015**, 3, 473-485.

[24] K. H. Choi, S. J. Cho, S. H. Kim, Y. H. Kwon, J. Y. Kim and S. Y. Lee, *Adv. Funct. Mater*. **2014**, 24, 44-52.

[25] H. J. Ha, E. H. Kil, Y. H. Kwon, J. Y. Kim, C. K. Lee and S. Y. Lee, *Energy Environ. Sci*. **2012**, 5, 6491-6499.

[26]Y. Kang, W. Lee, D. H. Suh and C. Lee, *J. Power Sources* **2003**, 119, 448-453.

[27] J. Shim, J. S. Lee, J. H. Lee, H. J. Kim and J.-C. Lee, *ACS Appl. Mater. Interfaces* **2016**, 8, 27740-27752.

[28] Y. K. Kang, J. Lee, J. I. Lee and C. Lee, *J. Power Sources* **2007**, 165, 92-96.

[29] S. Q. Ma, Y. H. Jiang, X. Q. Liu, L. B. Fan and J. Zhu, *RSC. Adv.* **2014**, 4, 23036-23042.

[30] C. Aouf, H. Nouailhas, M. Fache, S. Caillol, B. Boutevin and H. Fulcrand, *Eur. Polym. J.* **2013**, 49, 1185-1195.

[31] J. Qin, H. Liu, P. Zhang, M. Wolcott and J. Zhang, *Polym. Int.* **2014,** 63, 760-765.

[32] L. Long, S. Wang, M. Xiao and Y. Meng, *J. Mater. Chem. A* **2016**,

4, 10038-10069.

[33] F. Croce, L. Persi, F. Ronci and B. Scrosati, *Solid State Ionics*, **2000**, 135, 47-52.

[34] S. H. Chung, Y. Wang, L. Persi, F. Croce, S. G. Greenbaum, B. Scrosati and E. Plichta, *J. Power Sources*, **2001**, 97-98, 644-648.

[35] X. L. Hu, G. M. Hou, M. Q. Zhang, M. Z. Rong, W. H. Ruan and E. P. Giannelis, *J. Mater. Chem*. **2012**, 22, 18961-18967.

[36] C. Tang, K. Hackenberg, Q. Fu, P. M. Ajayan and H. Ardebili, *Nano Lett*. **2012**, 12, 1152-1156.

[37] D. Zhou, X. Mei and J. Ouyang, *J. Phys. Chem. C* **2011**, 115, 16688-16694.

[38] H. T. T. Le, D. T. Ngo, R. S. Kalubarme, G. Cao, C.-N. Park and C.-J. Park, *ACS Appl. Mater. Interfaces* **2016**, 8, 20710-20719.

[39] H. J. Walls, J. Zhou, J. A. Yerian, P. S. Fedkiw, S. A. Khan, M. K. Stowe and G. L. Baker, *J. Power Sources* **2000**, 89, 156-162.

[40] H. S. Lee, X. Q. Yang, C. L. Xiang, J. Mcbreen and L. S. Choi, *J. Electrochem. Soc.* **1998**, 145, 2813-2818.

[41] P. G. Bruce, J. Evans and C. A. Vincent, *Solid State Ionics* **1988**, 28, 918-922.

[42] C. S. Kim and S. M. Oh, *Electrochim. Acta* **2000**, 45, 2101-2109.

[43] Y. M. Lee, J. E. Seo, N. S. Choi and J. K. Park, *Electrochim. Acta* **2005**, 50, 2843-2848.

[44] K. L. Mathews, A. M. Budgin, S. Beeram, A. T. Joenathan, B. D. Stein, U. Werner-Zwanziger, M. Pink and L. A. Baker, *J. Mater. Chem. A* **2013**, 1, 1108-1116.

[45] T. Mizumo, K. Sakamoto, N. Matsumi and H. Ohno, *Electrochim. Acta* **2005**, 50, 3928-3933.

[46] L. F. Li, H. S. Lee, H. Li, X. Q. Yang and X. J. Huang, *Electrochem. Commun*. **2009**, 11, 2296-2299.

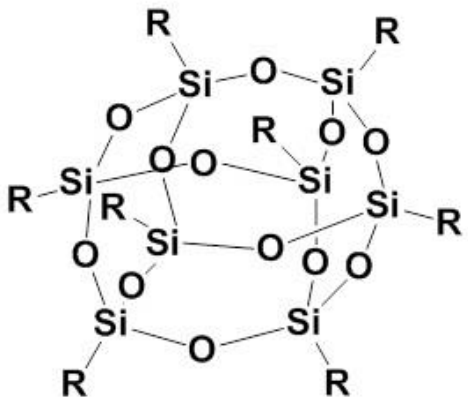

Figure 1.1. Structure of polyhedral oligomeric silsesquioxane (POSS).

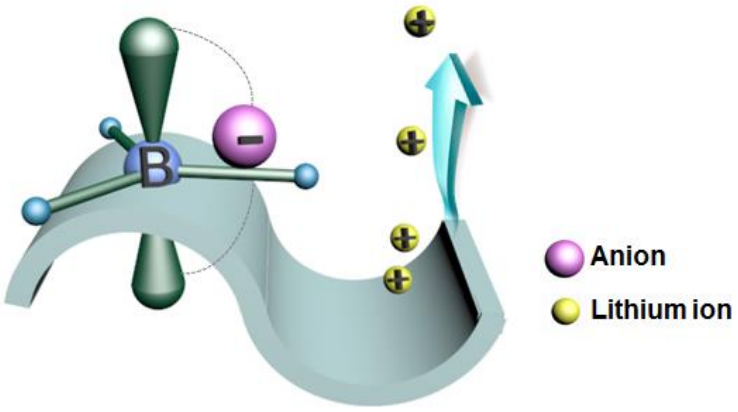

Figure 1.2. Anion-trapping ability of boron.

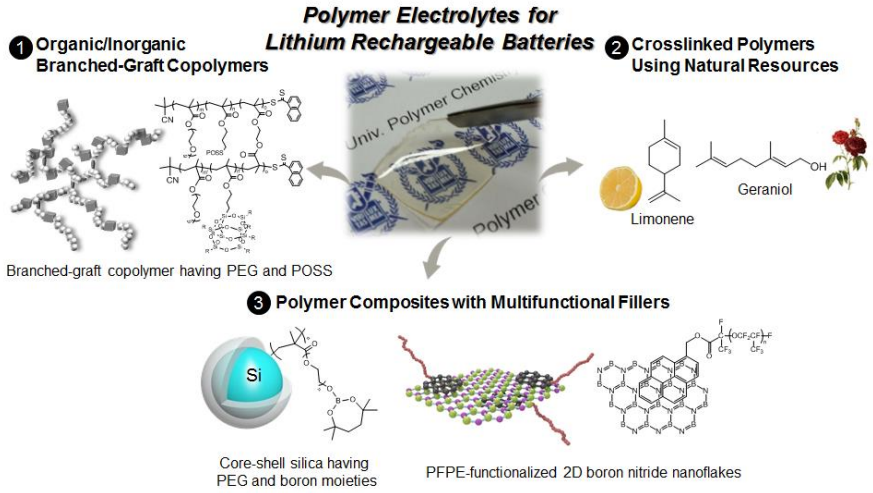

Figure 1.3. Polymer electrolytes for lithium rechargeable batteries.

Chapter 2

Synthesis and Properties of Organic/Inorganic Hybrid Branched-Graft Copolymers and Their Applications to Solid-State Electrolytes for High-Temperature Lithium-Ion Batteries

2.1. Introduction

Solid polymer electrolytes (SPEs) for lithium-ion battery applications have attracted great attention in recent years due to the safety issues of the conventional liquid electrolytes.[1-3] Organic liquid electrolytes commonly used for most of the commercialized lithium-ion batteries can cause serious safety problems especially at high-temperature due to their high volatility and flammability. In order to widen the applications of lithium-ion batteries to high-temperature such as electric vehicle or surplus electricity storage system at night, the development of high-temperature tolerant SPEs exhibiting good thermal stability, dimensional stability, and high ionic conductivity is required. Linear poly(ethylene oxide) (PEO) has been studied intensively as a matrix for SPEs owing to its ability to conduct lithium ions.[1-3] However, it could not be utilized directly for the practical lithium-ion battery applications, due to the low ionic conductivity that originates from the suppressed segmental motions of PEO in the crystalline phase.[4, 5] In order to overcome this shortcoming of the linear PEO-based SPEs, many efforts have been attempted to develop novel polymer matrices with amorphous state having very small

content of the crystalline domains.[6-8] For example, comb-like polymers having short PEG side chains have been used, though they also cannot be used directly for SPEs since they are normally not dimensionally-stable with wax state due to their low glass transition temperatures.[9, 10] To improve the dimensional stability of polymers having short PEG side chains, several approaches using various polymers such as block copolymers[11-13], interpenetrating network polymers[14, 15], and composite polymers containing nanofillers have been proposed as polymer matrices for the SPEs.[16, 17]

Polyhedral oligomeric silsesquioxane (POSS) is a nano-sized organic/inorganic hybrid material containing a silicon/oxygen framework functionalized with various organic groups at each corner and has been widely used as a nanofiller for polymer composites owing to its superior mechanical strength.[18-20] POSS also provides additional free volume to the polymer matrix due to the steric effect, resulting in a high chain mobility of the polymers.[18, 21, 22] In our previous studies, dimensionally-stable free-standing films were obtained from copolymers having POSS and PEG side groups.[12, 23-25] It was revealed that the glass transition temperatures (T_gs) did not increase much with the incorporation of POSS side groups into the

polymers having PEG side groups despite the rigidity of the POSS groups. SPEs containing PEG functionalized POSS were also reported by Wunder *et al*., achieving enhanced ionic conductivity compared to high molecular weight PEO.[26, 27] Therefore, it could be expected that the POSS side groups in SPEs maintain the chain mobility of PEG segments as well as increase the dimensional stability of the polymers.

Branched polymers have been studied as possible polymer materials for SPEs owing to their amorphous nature, high processability, and the presence of many branch-ends that facilitate lithium-ion conduction.[28-32] Furthermore, they have larger free volume than the linear counterpart, which results in increased chain mobility.[33, 34] Although there have been many reports on branched polymers for SPEs, their ionic conductivities have mostly been quite low due to the existence of rigid aromatic groups and their syntheses also require several steps and tedious purification procedures.[29, 30, 33-39]

In this study, a series of branched-graft copolymers containing POSS side groups for dimensional stability and PEG side groups for lithium-ion conduction were synthesized *via* one-step RAFT polymerization and applied to SPEs for high-temperature lithium-ion batteries. Linear-graft copolymers with POSS and PEG side groups were also

synthesized for comparison. The effects of the POSS content and branched structure on the dimensional stability, thermal properties, and ionic conductivity were systematically investigated. By incorporating the POSS side groups into the wax-state branched poly(poly(ethylene glycol) methyl ether methacrylate) (P(PEGMA)), dimensionally-stable free-standing electrolyte films exhibiting reasonably high ionic conductivity could be prepared. The branched-graft copolymer electrolytes exhibited higher ionic conductivity than the linear-graft copolymer electrolytes when they had the same monomer composition.

2.2. Experimental

2.2.1. Materials

2,2'-Azobis(isobutyronitrile) (AIBN, Junsei) was recrystallized from ethanol prior to use. Poly(ethylene glycol) methyl ether methacrylate (PEGMA, average M_n = 475 g mol^{-1}) and ethylene glycol dimethylacrylate (EGDMA) was purchased from Aldrich and passed through an alumina column prior to polymerization. Methacrylisobutyl

POSS® (3-(3,5,7,9,11,13,15-heptaisobutyl-pentacyclo[9.5.1.1^{3,9}.1^{5,15}.1^{7,13}]octasiloxane-1-yl)propyl methacrylate, MA-POSS) was purchased from Hybrid Plastics (product no. MA0702) and used as received. Tetrahydrofuran (THF) was freshly distilled from sodium/benzophenone under a nitrogen atmosphere. Lithium bis(trifluoromethane sulfonyl)imide (LiTFSI, >98%, TCI) was dried under high vacuum at 130 ^{o}C for 24 h and subsequently placed in an argon filled glove box. The chain transfer agent (CTA), 2-cyanoprop-2-yl-1-dithionaphthalate (CPDN), was synthesized as previously described.[40-42] All other reagents and solvents were obtained from reliable commercial sources and used as received.

2.2.2. Synthesis of branched-graft poly(poly(ethylene glycol) methyl ether methacrylate-*r*-methacrylisobutyl-POSS) (BCP)

Branched-graft poly(poly(ethylene glycol) methyl ether methacrylate-*r*-methacrylisobutyl-POSS) is abbreviated to BCP. BCP21 containing 21 mol % of MA-POSS and 79 mol % of PEGMA monomeric units were synthesized *via* RAFT polymerization as follows. PEGMA (5.4 g, 11.3 mmol), MA-POSS (3.02 g, 3.0 mmol), EGDMA

(0.045 g, 0.023 mmol), CPDN (0.031 g, 0.11 mmol), and AIBN (0.006 g, 0.034 mmol) were dissolved in 14 mL of distilled THF and the resultant solution was added to a 100 mL Schlenk flask equipped with a magnetic stirring bar and a condenser. The solution was degassed by three consecutive freeze-pump-thaw cycles to remove oxygen and the reaction was performed in an oil bath thermostated at 85 ^{o}C for 21 h under nitrogen atmosphere. After the flask was removed from the oil bath, it was exposed to air and diluted with THF to quench the reaction. The unreacted monomers were removed by precipitation in hexane three times. After dried under vacuum at room temperature several days, pink rubbery solid product was obtained with 68 % yield. Other BCPs were also prepared from the same synthetic procedure with different monomer feeding ratios as shown in Table 2.1. ^{1}H NMR [300 MHz, $CDCl_3$, δ (ppm), TMS ref] of BCP21: 4.08 (CH_2-O-C(O)), 3.48-3.85 (CH_2-CH_2-O), 3.38 (CH_3-O), 1.85 (isobutyl, C*H*), 1.53-2.05 (methacrylate backbone, CH_2-C(CH_3)(C=O)), 0.95 (isobutyl, CH_3), 0.6 (isobutyl, CH_2), 0.78-1.11 (methacrylate backbone, CH_2-C(CH_3)(C=O)).

2.2.3. Synthesis of linear-graft poly(poly(ethylene glycol) methyl ether methacrylate-*r*-methacrylisobutyl-POSS) (LCP)

Linear-graft poly(poly(ethylene glycol) methyl ether methacrylate-*r*-methacrylisobutyl-POSS) is abbreviated to LCP. LCP21 containing 21 mol % of MA-POSS and 79 mol % of PEGMA monomeric units were synthesized *via* RAFT polymerization as follows. PEGMA (5.4 g, 11.3 mmol), MA-POSS (3.02 g, 3.0 mmol), CPDN (0.031 g, 0.11 mmol), and AIBN (0.006 g, 0.034 mmol) were dissolved in 14 mL of distilled THF and the resultant solution was added to a 100 mL Schlenk flask equipped with a magnetic stirring bar and a condenser. The solution was degassed by three consecutive freeze-pump-thaw cycles to remove oxygen and the reaction was performed in an oil bath thermostated at 85 ^{o}C for 21 h under nitrogen atmosphere. After the flask was removed from the oil bath, it was exposed to air and diluted with THF to quench the reaction. The unreacted monomers were removed by precipitation in hexane three times. After dried under vacuum at room temperature several days, pink rubbery solid product was obtained with 71 % yield. Other LCPs were also prepared from the same synthetic procedure with different monomer feeding ratios (Table 2.1). ^{1}H NMR [300 MHz, $CDCl_3$, δ (ppm), TMS ref] of LCP21: 4.1 (CH_2-O-C(O)), 3.48-3.85 (CH_2-CH_2-O), 3.38 (CH_3-O), 1.85 (isobutyl, C*H*), 1.53-2.05

(methacrylate backbone, CH_2-C(CH_3)(C=O)), 0.95 (isobutyl, CH_3), 0.6 (isobutyl, CH_2), 0.78-1.11 (methacrylate backbone, CH_2-C(CH_3)(C=O)).

2.2.4. Preparation of solid polymer electrolytes (SPEs)

The solid polymer electrolytes containing LiTFSI and polymers in various blend compositions were prepared by a solution casting technique. Doping levels are defined as the ratio of the number of lithium cations (Li^+) to that of ethylene oxide (EO) repeating unit in the polymers ([Li]/[EO]). 0.1 g of polymers and the given amounts of LiTFSI were dissolved in 0.5 mL of THF and homogeneous solution was obtained. After that, the solution was cast onto a Teflon plate (2 x 2 cm^2) and dried at room temperature for overnight. Subsequently, it was further dried under high vacuum at room temperature for 24 h. Finally, the film was peeled off from the Teflon plate and the resultant film was placed in a high vacuum condition for a week at 80 ^oC prior to measure the ionic conductivities of the solid polymer electrolytes. The thickness of the films measured by a micrometer (Mitutoyo, 293-330 IP 65 water resistant) was in the range of 200-300 μm.

2.2.5. Cell fabrication and electrochemical characterization

The electrochemical stability of BCP21 was evaluated using linear sweep voltammetry (LSV). The cell was assembled by sandwiching BCP21 electrolyte between stainless steel (working electrode) and lithium metal (reference electrode) in 2032 coin cell. The cell was swept in the potential range from 1 V to 7 V (versus Li/Li^+) at scan rate of 1 mV/s at 60 ^oC. Charge/discharge test of all-solid-state lithium-ion battery was performed at cutoff voltages of 2.0 ~ 3.8 V versus Li/Li^+ at 60 ^oC with current density of 0.1 C. V_2O_5 (60 wt%) was used as cathode active material and dispersed in N-methyl-2-pyrrolidone (NMP) with carbon black (20 wt%) and PVDF (20 wt%). The resultant slurry was deposited and cast onto Aluminium current collector using doctor blade. The residual NMP was completely dried under vacuum condition at 100 ^oC for 1 day. The obtained cathode sheet, lithium metal, and solid polymer electrolyte (SPE) were punched into disk and assembled together in 2032 coin cell to form Li/SPE(BCP21)/V_2O_5 cell. All components were prepared in argon filled glove box (H_2O < 0.5 ppm, O_2 < 0.5 ppm).

2.2.6. Characterization

^{1}H nuclear magnetic resonance (NMR) spectra were recorded on an Ascend^{TM} 400 spectrometer (300 MHz) using $CDCl_3$ (Cambridge Isotope Laboratories) as the solvent at room temperature with tetramethylsilane (TMS) as a reference. ^{13}C and ^{29}Si NMR spectra were recorded on JeolJNM-LA400 spectrometer (400 MHz) using $CDCl_3$ (Cambridge Isotope Laboratories) as the solvent at room temperature. Molecular weights (M_n, M_w) and polydispersity index (PDI) were analyzed by gel permeation chromatography (GPC). Relative molecular weight was measured by GPC equipped with a Waters 515 HPLC pump and three columns including PLgel 5.0 μm guard, MIXED-C, and MIXED-D from Polymer Laboratories in series with a Viscotek LR125 laser refractometer. The system with a refractive index (RI) detector was calibrated using polystyrene standards from Polymer Laboratories. The resulting data was analyzed using the Omnisec software. Absolute molecular weights of polymers were analyzed using a Waters 515 HPLC pump equipped with three columns including PLgel 5.0 μm guard, MIXED-C, and MIXED-D from Polymer Laboratories in series with a Wyatt Technology MiniDAWN^{TM} triple-angle light scattering

detector and a Wyatt Technology Optilab DSP interferomeric refractometer. HPLC grade THF (J. T. Baker) was used as the eluent at a flow rate of 1.0 mL min^{-1} at 35 ^{o}C. The thermal transition temperatures of the polymers were examined by differential scanning calorimetry (DSC) using TA Instruments DSC-Q1000 under a nitrogen atmosphere. Samples with a typical mass of 3-7 mg were encapsulated in sealed aluminium pans. The samples were first heated to 150 ^{o}C and then quenched to -80 ^{o}C. This was followed by a second heating scan from -80 ^{o}C to 150 ^{o}C at a heating rate of 10 ^{o}C min^{-1}. The thermal stability of the polymers was investigated by thermogravimetric analysis (TGA) using TA Instruments TGA Q-5000IR under nitrogen atmosphere. The samples were maintained at 130 ^{o}C for 10 min to remove residual water molecules, and then heated to 700 ^{o}C at a heating rate of 10 ^{o}C min^{-1}. Transmission electron microscopy (TEM) was performed on a LIBRA 120 with an accelerating voltage of 120 kV. TEM specimens were prepared by drop casting of 1 wt% polymer solutions in THF on carbon-coated copper grid. Temperature-resolved rheological measurement was carried out using an rheometer (Advanced Rheometric Expansion System, ARES) in the linear viscoelastic region with 0.1 rad s^{-1} of frequency at 1 ^{o}C min^{-1} ramp.

Shear viscosity was also measured using ARES rheometer. Each sample was subjected to a shear rate of 10 Hz for 120 seconds at 30 ^{o}C. The average viscosity value was calculated and used as x-axis of Walden plot. The ionic conductivity of the SPEs was analyzed by complex impedance spectroscopy between 10 to 80 ^{o}C under dry nitrogen condition using Zahner Electrik IM6 apparatus in the frequency range of 0.1 Hz to 1 MHz and an applied voltage of 10 mV. The real part of the impedance at the minimum of imaginary part was used as the resistance to calculate the conductivity of the SPEs. The samples for the measurements were prepared by sandwiching the SPEs between two stainless-steel electrodes. Each sample was allowed to equilibrate for 30 min at each temperature prior to taking measurements. The ionic conductivity (σ) was calculated from the electrolyte resistance (R) obtained from the impedance spectrum, the electrolyte thickness (d) and the area of the electrode (A) using the following equation, $\sigma = (1/R) \times (d/A)$. Electrochemical stability was evaluated by linear sweep voltammetry (LSV) using a potentiostat (VMP3, Biologics) at 60 ^{o}C at scan rate of 1 mV/s. Charge/discharge test of all-solid-state lithium-ion battery was performed with a WBCS3000 battery cycler (WonATech) at 60 ^{o}C.

2.3. Results and Discussion

2.3.1. Synthesis of organic/inorganic hybrid branched and linear-graft copolymers

A series of organic/inorganic hybrid branched-graft copolymers (BCPs) was synthesized *via* RAFT polymerization. Since RAFT polymerization follows the pseudo-living polymerization mechanism, it has many advantages over the free radical polymerization regarding the control of polymer structures, molecular weights, and polydispersity.[43-47] For example, when diacrylate monomers are included in the polymerization systems, well-defined branched polymers with low PDI values could be prepared *via* RAFT polymerization without any gelation, whereas cross-linked polymers are normally obtained through the free radical polymerization.[48, 49]

The synthetic procedures of BCPs with PEGMA and MA-POSS monomeric units are illustrated in Figure 2.1. PEGMA and MA-POSS are comonomers and EGDMA acts as a branching agent to generate bridges between linear chains. MA-POSS was incorporated in order to

enhance the dimensional stability of polymers because P(PEGMA) homopolymer without any POSS moieties was found to be in a waxy state. CPDN was chosen as a chain transfer agent (CTA) to mediate the RAFT polymerization in this study because it has been widely used as an effective CTA to prepare polymers with low PDI from the living radical polymerization of methacrylate monomers.[50] The feed ratio of PEGMA and/or MA-POSS : EGDMA : CPDN : AIBN was fixed to 100 : 2 : 1 : 0.3. The molar ratio of EGDMA to CPDN was determined as 2 : 1 in order to prepare branched polymers without any gelation because gelation occurs during the polymerization when the ratio of EGDMA/CPDN is larger than 3. Linear-graft copolymers (LCPs) were also prepared using only two monomers, PEGMA and/or MA-POSS, without a branching agent in order to investigate the structural effects on the properties of polymers.

The structure of polymers was confirmed by ^{1}H NMR analysis, as shown in Figure 2.2. The signals c and d at 3.48-4.21 ppm and 3.38 ppm are assigned to the CH_2-CH_2-O and terminal CH_3-O of PEG side groups, respectively. Signals a and b at 1.53-2.05 ppm and 0.78-1.11 ppm can be assigned to the methylene and methyl protons of the poly(methacrylate) backbone, respectively, although these signals could

not be clearly verified due to their low intensity. The presence of protons from MA-POSS in BCP21 was also clearly confirmed. The peaks observed at 0.6 ppm (signals e and f) are assigned to the methylene protons of MA-POSS. The protons from isobutyl groups of MA-POSS are observed at 1.85 ppm (signal g) and 0.95 ppm (signal h). The compositions of monomers in the copolymers were calculated from the following equation (1):

$$\text{MA–POSS Content (mol \%)} = (I_{e+f}/\,16) / [(I_d/\,3) + (I_{e+f}/\,16)] \times 100 \quad (1)$$

where I_d is the integral value of the signal d at 3.38 ppm corresponding to the methyl protons of PEGMA moieties and I_{e+f} is the integral value of signals e and f at 0.6 ppm, corresponding to the methylene protons of MA-POSS moieties. Additionally, the presence of POSS moieties in BCP21 was also verified by ^{29}Si NMR and ^{13}C NMR analysis (Figure 2.3 and Figure 2.4, respectively). In ^{29}Si NMR spectrum, there are two resonance peaks due to different proximity of silicon atoms to the methacryl side chains. These two peaks at -67.2 ppm and -67.4 ppm correspond to the isobutyl substituted silicon.[51]

In ^{13}C NMR spectrum, signals in 70-80 ppm are assigned to CH_2-CH_2-O units, and signal from terminal CH_3-O of PEG side groups is shown at 59.2 ppm. Signals from isobutyl groups attached to the silicon of POSS and carbons in polymer backbone are clearly observed at 20-30 ppm.

Although the branching points could not be elucidated from the ^1H NMR spectra, the presence of branching in the copolymers could be estimated by the differences in their absolute and relative molecular weights ($M_{w\ \mathrm{MALLS}}$ and $M_{w\ \mathrm{RI}}$, respectively) as shown in Table 2.1. It is known that branched-graft copolymers have smaller hydrodynamic volume than that of the linear counterparts.[33, 52] $M_{w\ \mathrm{RI}}/M_{w\ \mathrm{MALLS}}$ values of BCPs are always smaller than those of the corresponding LCPs, indicating that BCPs have some branching points in their structures. Furthermore, BCPs have higher absolute molecular weights than the corresponding LCPs when they have the same monomer composition because EGDMA generates bridges between the linear polymer chains.

The MA-POSS content in the polymers was controlled to be in the range of 9 - 36 mol % in this study. Flexible free-standing films could be prepared from the copolymers when MA-POSS content was in the

range of 21 - 40 mol %. Although we tried to synthesize BCPs having larger MA-POSS content than 40 mol %, it was difficult to purify the copolymers due to their amphiphilic properties. For instance, copolymers having MA-POSS content larger than 40 mol % are soluble in nonpolar solvents such as hexane and ether as well as in polar solvents such as methanol, and then the resulting copolymers cannot be separated easily from the monomers.

2.3.2. Thermal properties

BCP21, BCP30, BCP36, and LCP21 were chosen to evaluate the effects of the POSS content and the polymer structures on the thermal properties and ionic conductivities because dimensionally-stable free-standing films could be prepared from them and the purpose of this study is the possible application of the newly synthesized copolymers for SPE applications.

Figure 2.5 shows the DSC thermograms of the four organic/inorganic hybrid copolymers with MA-POSS moieties and branched P(PEGMA) without MA-POSS moieties. The branched P(PEGMA) shows a distinct melting transition peak (T_m) at -3.5 ^{o}C,

indicating that the branched P(PEGMA) has a semicrystalline phase, because it has crystalline PEG side chains.[53] In contrast, the melting transition peak is not observed for the copolymers with MA-POSS moieties, because the bulky POSS side groups suppress the crystallization of PEG side chains.[54] The copolymers having MA-POSS moieties show two glass transition temperatures at around -60 and 80 ^{o}C, respectively. The lower and higher ones are originated from the chain motions from PEGMA and MA-POSS segments in the copolymers, respectively.[12, 22]

Although the rigidity of POSS can suppress the mobility of polymer segments due to the rigid nature of POSS, the large volume of POSS can also provide interchain spacing and free volume of polymers to reduce the rotational energy barrier.[54-56] Moreover, flexible linear side chains such as PEG side groups can work as a plasticizer when they do not have ordered structures, thereby decreasing the T_g.[57] Since T_g of copolymers could be affected by both steric barrier and free volume effect of the POSS and PEG side groups, it could not be easily explained simply by the content of each monomeric units. To further study the effect of POSS moieties on the glass transition behavior of BCPs, BCP13 having 13 mol % of POSS monomer was intentionally

synthesized and its T_g of P(PEGMA) segment was found to be -70.1 ^{o}C which is lower than those of branched P(PEGMA) (-63.4 ^{o}C) and other BCPs. As shown in Figure 2.6, T_g of P(PEGMA) segments in BCP decreases with the increase of the POSS content to 13 mol %, then further increases when the POSS content is larger than about 13 mol %. However, when the POSS content is less than 30 mol %, the T_g is even smaller than that of P(PEGMA) because the POSS groups can provide considerable free volume offsetting the rigid nature of POSS. In other words, the flexibility of ion-conducting PEG side chains can be maintained when the POSS content is less than 30 mol %.

Meanwhile, T_g of P(PEGMA) segments in BCP21 is smaller than that of the LCP21, indicating that the chain mobility of the branched-graft polymers is larger than that of the linear-graft polymers when they have the same monomer composition. The larger chain mobility of BCP21 than that of the LCP21 can be ascribed to the larger free volume of branched-graft polymers than that of the linear counterparts. Similarly, larger chain mobility and smaller T_g values of branched polymers over the linear polymers were also reported by others. [33, 34]

The degradation temperatures at 5 % weight loss ($T_{d,\ 5\%}$) of the polymers are summarized in Table 2.2. The thermal decomposition of

the polymers occurred above 200 ^{o}C. $T_{d,\ 5\%}$ values of the polymers decrease with increasing MA-POSS content, because the isobutyl vertex groups of the POSS moieties decompose at lower temperature.[22] Furthermore, $T_{d,\ 5\%}$s of BCP21 and LCP21 are 277 ^{o}C and 232 ^{o}C, respectively, suggesting that the branched-graft polymer has better thermal stability than the corresponding linear-graft polymer.[58]

SPE films containing various LiTFSI concentrations ([Li]/[EO] = 0.03 – 0.11) were prepared from BCPs and LCP21 by solution casting technique. The prepared SPEs were flexible and transparent free-standing films as shown in Figure 2.7. These copolymers having MA-POSS moieties show dimensional stability as films at room temperature, because the glass transition temperatures of the MA-POSS segments are much higher than room temperature. Also, the presence of nanoscale-domain of the MA-POSS moieties was confirmed by TEM micrographs as shown in Figure 2.8. Although the polymers have random structure with PEG and POSS moieties, some phase separation could happen in the copolymer.[19, 59-61] Dark spots corresponding to the POSS-rich domain could be observed without additional staining processes, since the silicon in the POSS has high electron density.[62]

The dark spots are randomly distributed in the matrix, and the size of the POSS-rich domain is around 20 nm, indicating that the POSS-rich domain was formed through the aggregation of 10-15 blocks of POSS cages, because the approximate diameter of single POSS cage is about 1.5 nm.

Figure 2.9 presents the temperature-resolved rheological behaviors of the BCP electrolyte films ([Li]/[EO] = 0.07). It was revealed that the storage modulus (G') values were maintained until the temperature reaches the T_g of P(MA-POSS) segments, even though the T_g of the ion-conducting phase is quite low (around –60 ^{o}C). This result suggests that the formation of dimensionally-stable free-standing films is mainly attributed to the existence of the POSS-rich domain. Owing to this fact, the dimensional stability of the BCP electrolyte films could be maintained as its original shape even if temperature increases up to 90 ^{o}C. Then we don't need a separator in the assembly of lithium-ion battery because the inter-electrode distance could be maintained using the solid-state BCP electrolyte even at the elevated temperature. Therefore, BCP21 can be utilized as SPE for lithium-ion batteries operated at high-temperature. It is noteworthy that random copolymer prepared by simple one-step random copolymerization without any

block copolymer structure exhibits good dimensional stability. Furthermore, the G' value increases as the POSS content increases in the polymers, suggesting that the POSS moieties in the polymers definitely enhance the dimensional stability of the SPEs.[63, 64]

2.3.3. Ionic conductivity

Figure 2.10 shows the ionic conductivities of branched P(PEGMA), LCP21, and BCP electrolytes containing LiTFSI with various concentrations at 30 ^{o}C. According to equation (2), the ionic conductivity is related to the number of charge carriers and their mobility; n is the number of charge carriers, q is the charge on each charge carriers, and μ is the mobility of charge carriers.[65]

$$\sigma = \Sigma\, n\, q\, \mu \tag{2}$$

Although the ionic conductivity (σ) is expected to increase linearly as the lithium salt concentration (n) increases, the ionic conductivity does not increase continuously with increasing lithium salt concentration. It reaches a maximum value at a certain ratio of [Li]/[EO], followed by a

decrease with a further increase in lithium salt content. The optimum salt concentrations were found at [Li]/[EO] of 0.07 for branched P(PEGMA), BCP21, and LCP21, and at 0.09 for BCP30 and BCP36. This decrease could be attributed to two contributions. First, as the lithium salt concentration increases in the SPEs, the formation of associated ionic species such as contact ion pairs or ion aggregates also increases, thereby decreasing the number of effective charge carriers.[66] Second, the polymer chain mobility gradually decreases with increasing lithium salt concentration as estimated by the increase in T_g values as shown in Figure 2.11. This is ascribed to the increase in intermolecular or intramolecular interactions between the oxygen of the PEG moieties and the lithium cations with increasing lithium salt concentration.[67] Therefore, the number of effective charge carriers and the mobility of polymer segments decrease with increasing lithium salt concentration, resulting in a decrease in the ionic conductivity of the polymer electrolytes with larger amount of lithium salts. The decrease in ionic conductivity of SPEs at high salt concentrations was also observed for other polyether-based polymer electrolytes.[68] To further study the conductivity behavior of the electrolytes, molar conductivity as a function of square root of LiTFSI concentration for

each electrolyte and Walden plot (molar conductivity *vs*. shear fluidity (viscosity^{-1})) of BCP21 were depicted as shown in Figure 2.12. The molar conductivity firstly decreases until the salt concentration reaches to certain ratio due to formation of ion pairing, and then increases to reach the maximum conductivity due to formation of ion triplets and re-dissociation effect. At high LiTFSI concentration, the conductivity decreases again due to further increase of T_g and viscosity. In addition to the T_g of the polymer electrolytes, viscosity has been known to another very important factor affecting the ionic conductivity.[69] Walden plot in Figure 2.12(b) shows the relationship between viscosity and ionic conductivity very well; the increase of viscosity with LiTFSI concentration decreases the molar conductivity.

Figure 2.13 shows the temperature dependence of ionic conductivities of branched P(PEGMA), LCP21, and BCP electrolytes, where each electrolyte has the same lithium salt concentration ([Li]/[EO] = 0.07). It was revealed that the electrolytes with smaller POSS content exhibit higher ionic conductivities. BCP21 electrolyte exhibits maximum ionic conductivity over the entire temperature ranges among the SPEs. The ionic conductivity of BCP21 (1.6×10^{-4} S/cm) is about three times higher than that of BCP36 (4.7×10^{-5} S/cm)

at 60 ^{o}C. The lithium-ion conduction in SPEs occurs through long-range migration of lithium-ions by the exchange of solvation sites, as the PEG side groups have mobility in the polymer matrix at temperatures above T_g.[26] As the POSS content in the polymer matrix increases, the mobility of the polymer decreases, because the bulky POSS groups can work as a steric barrier, as estimated by the increase of T_g values of ion-conducting PEG segments in the electrolytes (Table 2.2). Therefore, the polymer electrolytes containing smaller POSS content have larger chain mobility and exhibit higher ionic conductivities. In addition, the lithium ion content of the electrolytes also affects the ionic conductivity. The polymer electrolytes containing smaller POSS content have larger PEG content, indicating that more lithium ions exist in the SPEs with smaller POSS content when the lithium salt concentrations are same ([Li]/[EO] = 0.07). Meanwhile, BCP21 electrolyte exhibits higher ionic conductivity than the LCP21 electrolyte. This result is ascribed to the larger chain mobility of the branched-graft polymer compared to that of the linear counterpart, as estimated by the lower T_g value of ion-conducting PEG segments originating from the larger free volume. [33, 34]

2.3.4. Electrochemical stability and all-solid-state cell performance

In order to operate the lithium-ion battery at broad potential window, the electrochemical stability of electrolyte is considered to be crucial factor. The electrochemical stability of BCP21 was evaluated by using linear sweep voltammetry with SS (Stainless steel)/BCP21/Li coin cell at 60 ^{o}C as shown in Figure 2.14. The current density is almost constant until the applied voltage swept to about 4.6 V. The abrupt rise of current at about 4.6 V corresponds to the electrochemical oxidative degradation of electrolyte. However, BCP21 is still electrochemically stable within the operation voltage range of V_2O_5 cathode as well as other higher voltage class cathode materials. This potential window is much wider than those of linear PEO-based electrolytes. Moreover, the electrochemical window of BCP21 is larger than that of organic liquid electrolytes (~ 4.5 V). Therefore, BCP21 can be applied to high-voltage battery systems over a wide temperature range.

Charge/discharge test of all-solid-state Li/BCP21/V_2O_5 cell was performed at 60 ^{o}C cycled at 0.1 C rate (Figure 2.15). Quite high initial discharge capacity was observed, while it continuously decreases and

stabilizes to 124 mAh g^{-1}, resulting in 65 % of capacity retention after 30 cycles. The relatively low capacity retention behavior might be caused by the solid nature of SPEs because the possible interfacial resistance between the interface of solid electrolyte and the cathode can prevent the full utilization of active materials in cathode.[70] However, this result still demonstrates that BCP21 has possibility to be used in high-temperature lithium-ion battery system without causing safety problems.

2.4. Conclusions

Organic/inorganic hybrid branched-graft copolymers (BCPs) containing PEGMA and MA-POSS moieties were synthesized by simple one-step RAFT polymerization. Linear-graft copolymers (LCPs) with PEGMA and MA-POSS moieties were also synthesized for comparison. Enhanced ionic conductivities and dimensional stability of the SPEs were accomplished by controlling the polymer structures and the MA-POSS content in the copolymers. Maximum ionic conductivity of 1.6 x 10^{-4} S/cm at 60 ^{o}C was achieved for the BCP21 electrolyte containing 21 mol % of MA-POSS and 79 mol %

of PEGMA moieties. It is very worthy to note that the MA-POSS moieties maintain the chain mobility of polymers despite its own rigidity as well as provide significant dimensional stability to the SPEs even at the high temperature. The branched-graft BCP21 electrolyte exhibited higher ionic conductivity than the linear-graft LCP21 electrolyte because the branched structure gives larger chain mobility to the polymers as estimated by the lower T_g value of ion-conducting segments. BCP21 exhibits wide electrochemically stable potential window and all-solid-state battery test at 60 ^{o}C was successfully performed without causing safety problem. All of these unique features of BCPs suggest that the SPEs with branched structure containing POSS moieties are very promising candidate for the field of high-temperature lithium-ion battery applications.

2.5. References

[1] A. Manuel Stephan and K. S. Nahm, *Polymer*, 2006, **47**, 5952-5964.

[2] W. H. Meyer, *Adv. Mater.*, 1998, **10**, 439-448.

[3] J. M. Tarascon and M. Armand, *Nature*, 2001, **414**, 359-367.

[4] D. E. Fenton, J. M. Parker and P. V. Wright, *Polymer*, 1973, **14**,

589-589.

[5] Q. Li, H. Y. Sun, Y. Takeda, N. Imanishi, J. Yang and O. Yamamoto, *J. Power Sources*, 2001, **94**, 201-205.

[6] M. S. Michael, M. M. E. Jacob, S. R. S. Prabaharan and S. Radhakrishna, *Solid State Ionics*, 1997, **98**, 167-174.

[7] Y. T. Shieh, G. L. Liu, K. C. Hwang and C. C. Chen, *Polymer*, 2005, **46**, 10945-10951.

[8] S. J. Park, A. R. Han, J. S. Shin and S. Kim, *Macromol. Res.*, 2010, **18**, 336-340.

[9] X. H. Flora, M. Ulaganathan, R. Babu and S. Rajendran, *Ionics*, 2012, **18**, 731-736.

[10] H. J. Ha, E. H. Kil, Y. H. Kwon, J. Y. Kim, C. K. Lee and S. Y. Lee, *Energy Environ. Sci.*, 2012, **5**, 6491-6499.

[11] Y. Kato, S. Yokoyama, H. Ikuta, Y. Uchimoto and M. Wakihara, *Electrochem. Commun.*, 2001, **3**, 128-130.

[12] N. A. A. Rossi, Z. Zhang, Y. Schneider, K. Morcom, L. J. Lyons, Q. Wang, K. Amine and R. West, *Chem. Mater.*, 2006, **18**, 1289-1295.

[13] L. Zhang, Z. Zhang, S. Harring, M. Straughan, R. Butorac, Z. Chen, L. Lyons, K. Amine and R. West, *J. Mater. Chem.*, 2008, **18**, 3713-3717.

[14] J. Y. Ji, J. Keen and W. H. Zhong, *J. Power Sources*, 2011, **196**, 10163-10168.

[15] S.-K. Kim, D.-G. Kim, A. Lee, H.-S. Sohn, J. J. Wie, N. A. Nguyen, M. E. Mackay and J.-C. Lee, *Macromolecules*, 2012, **45**, 9347-9356.

[16] P. P. Soo, B. Y. Huang, Y. I. Jang, Y. M. Chiang, D. R. Sadoway and A. M. Mayes, *J. Electrochem. Soc.*, 1999, **146**, 32-37.

[17] D. He, S. Y. Cho, D. W. Kim, C. Lee and Y. Kang, *Macromolecules*, 2012, **45**, 7931-7938.

[18] B. Oh, D. Vissers, Z. Zhang, R. West, H. Tsukamoto and K. Amine, *J. Power Sources*, 2003, **119–121**, 442-447.

[19] J. L. Nugent, S. S. Moganty and L. A. Archer, *Adv. Mater.*, 2010, **22**, 3677-3680.

[20] F. Wang, X. Lu and C. He, *J. Mater. Chem.*, 2011, **21**, 2775-2782.

[21] B. H. Tan, H. Hussain, Y. W. Leong, T. T. Lin, W. W. Tjiu and C. B. He, *Polym. Chem.*, 2013, **4**, 1250-1259.

[22] J. Pyun and K. Matyjaszewski, *Macromolecules*, 2000, **33**, 217-220.

[23] A. Strachota, I. Kroutilová, J. Kovářová and L. Matějka, *Macromolecules*, 2004, **37**, 9457-9464.

[24] J. Wu, T. S. Haddad and P. T. Mather, *Macromolecules*, 2009, **42**, 1142-1152.

[25] H.-S. Ryu, D.-G. Kim and J.-C. Lee, *Macromol. Res.*, 2010, **18**, 1021-1029.

[26] H.-S. Ryu, D.-G. Kim and J.-C. Lee, *Polymer*, 2010, **51**, 2296-2304.

[27] D.-G. Kim, H.-S. Sohn, S.-K. Kim, A. Lee and J.-C. Lee, *J. Polym. Sci., Part A: Polym. Chem.*, 2012, **50**, 3618-3627.

[28] H. J. Zhang, S. Kulkarni and S. L. Wunder, *J. Phys. Chem. B*, 2007, **111**, 3583-3590.

[29] H. J. Zhang, S. Kulkarni and S. L. Wunder, *J. Electrochem. Soc.*, 2006, **153**, A239-A248.

[30] C. J. Hawker, F. K. Chu, P. J. Pomery and D. J. T. Hill, *Macromolecules*, 1996, **29**, 3831-3838.

[31] T. Itoh, Y. Ichikawa, N. Hirata, T. Uno, M. Kubo and O. Yamamoto, *Solid State Ionics*, 2002, **150**, 337-345.

[32] T. Uno, H. Sano, M. Matsumoto, M. Kubo and T. Itoh, *J. Solid State Electr.*, 2010, **14**, 2161-2167.

[33] D. Wilms, M. Schomer, F. Wurm, M. I. Hermanns, C. J. Kirkpatrick and H. Frey, *Macromol. Rapid Commun.*, 2010, **31**, 1811-

1815.

[34] M. Marzantowicz, J. R. Dygas, F. Krok, A. Tomaszewska, Z. Florjanczyk, E. Zygadlo-Monikowska and G. Lapienis, *J. Power Sources*, 2009, **194**, 51-57.

[35] P. A. Costello, I. K. Martin, A. T. Slark, D. C. Sherrington and A. Titterton, *Polymer*, 2002, **43**, 245-254.

[36] H. R. Allcock, S. J. M. O'Connor, D. L. Olmeijer, M. E. Napierala and C. G. Cameron, *Macromolecules*, 1996, **29**, 7544-7552.

[37] T. Itoh, S. Gotoh, S. Horii, S. Hashimoto, T. Uno, M. Kubo, T. Fujinami and O. Yamamoto, *J. Power Sources*, 2005, **146**, 371-375.

[38] T. Itoh, S. Horii, T. Uno, M. Kubo and O. Yamamoto, *Electrochim. Acta*, 2004, **50**, 271-274.

[39] Y. Lin, F. Zeng-Guo, Z. Yu-Mei, W. Feng, C. Shi and W. Guo-Qing, *J. Polym. Sci., Part A: Polym. Chem.*, 2006, **44**, 3650-3665.

[40] Z. X. Wang, M. Ikeda, N. Hirata, M. Kubo, T. Itoh and O. Yamamoto, *J. Electrochem. Soc.*, 1999, **146**, 2209-2215.

[41] Z. Wen, T. Itoh, M. Ikeda, N. Hirata, M. Kubo and O. Yamamoto, *J. Power Sources*, 2000, **90**, 20-26.

[42] M. Benaglia, E. Rizzardo, A. Alberti and M. Guerra, *Macromolecules*, 2005, **38**, 3129-3140.

[43] H. S. Sohn, S. H. Cha, W. K. Lee, D. G. Kim, H. J. Yun, M. S. Kim, B. D. Kim, Y. H. Kim, J. W. Lee, J. S. Kim, D. B. Kim, J. H. Kim and J. C. Lee, *Macromol. Res.*, 2011, **19**, 722-728.

[44] J. Zhu, X. L. Zhu, Z. P. Cheng, F. Liu and J. M. Lu, *Polymer*, 2002, **43**, 7037-7042.

[45] M. Dietrich, M. Glassner, T. Gruendling, C. Schmid, J. Falkenhagen and C. Barner-Kowollik, *Polym. Chem.*, 2010, **1**, 634-644.

[46] X. Y. Jiang, Y. J. Li, G. L. Lu and X. Y. Huang, *Polym. Chem.*, 2013, **4**, 1402-1411.

[47] C. P. Li, J. Q. Wang, Y. Shi, Z. Liu, J. Lin and Z. F. Fu, *Macromol. Res.*, 2012, **20**, 858-867.

[48] R. Severac, P. Lacroix-Desmazes and B. Boutevin, *Polym. Int.*, 2002, **51**, 1117-1122.

[49] M. Wang, L. Qi, F. Zhao and S. Dong, *J. Power Sources*, 2005, **139**, 223-229.

[50] B. L. Liu, A. Kazlauciunas, J. T. Guthrie and S. Perrier, *Macromolecules*, 2005, **38**, 2131-2136.

[51] Y. Lin, X. Liu, X. Li, J. Zhan and Y. Li, *J. Polym. Sci., Part A: Polym. Chem.*, 2007, **45**, 26-40.

[52] J. Chiefari, Y. K. Chong, F. Ercole, J. Krstina, J. Jeffery, T. P. T. Le,

R. T. A. Mayadunne, G. F. Meijs, C. L. Moad, G. Moad, E. Rizzardo and S. H. Thang, *Macromolecules*, 1998, **31**, 5559-5562.

[53] H. Hussain, B. H. Tan, G. L. Seah, Y. Liu, C. B. He and T. P. Davis, *Langmuir*, 2010, **26**, 11763-11773.

[54] D. Yan, W. J. Wang and S. Zhu, *Polymer*, 1999, **40**, 1737-1744.

[55] P. R. Chinnam and S. L. Wunder, *Chem. Mater.*, 2011, **23**, 5111-5121.

[56] J. K. H. Teo, C. L. Toh and X. H. Lu, *Polymer*, 2011, **52**, 1975-1982.

[57] J. Wu, T. S. Haddad, G. M. Kim and P. T. Mather, *Macromolecules*, 2007, **40**, 544-554.

[58] S. Guns, P. Kayaert, J. A. Martens, J. Van Humbeeck, V. Mathot, T. Pijpers, E. Zhuravlev, C. Schick and G. Van den Mooter, *Eur. J. Pharm. Biopharm.*, 2010, **74**, 239-247.

[59] J.-C. Lee, M. H. Litt and C. E. Rogers, *J. Polym. Sci., Part A: Polym. Chem.*, 1998, **36**, 495-504.

[60] J.-W. Rhim, H. B. Park, C.-S. Lee, J.-H. Jun, D. S. Kim and Y. M. Lee, *J. Membrane Sci.*, 2004, **238**, 143-151.

[61] S. Roy, J. Feng, V. Scionti, S. C. Jana and C. Wesdemiotis, *Polymer*, 2012, **53**, 1711-1724.

[62] R. Verker, E. Grossman, I. Gouzman and N. Eliaz, *Compos. Sci. Technol.*, 2009, **69**, 2178-2184.

[63] H. Rios-Dominguez, F. A. Ruiz-Trevino, R. Contreras-Reyes and A. Gonzalez-Montiel, *J. Membrane Sci.*, 2006, **271**, 94-100.

[64] T. Hirai, M. Leolukman, C. C. Liu, E. Han, Y. J. Kim, Y. Ishida, T. Hayakawa, M.-a. Kakimoto, P. F. Nealey and P. Gopalan, *Adv. Mater.*, 2009, **21**, 4334-4338.

[65] G. Z. Li, L. Wang, H. Toghiani, T. L. Daulton and C. U. Pittman, *Polymer*, 2002, **43**, 4167-4176.

[66] F. Zhao, X. Bao, A. R. McLauchlin, J. Gu, C. Wan and B. Kandasubramanian, *Appl. Clay Sci.*, 2010, **47**, 249-256.

[67] H. Y. Wu, D. Saikia, C. P. Lin, F. S. Wu, G. T. K. Fey and H. M. Kao, *Polymer*, 2010, **51**, 4351-4361.

[68] I. Albinsson, B. E. Mellander and J. R. Stevens, *Solid State Ionics*, 1993, **60**, 63-66.

[69] M. Watanabe, Y. Suzuki and A. Nishimoto, *Electrochim. Acta*, 2000, **45**, 1187-1192.

[70] D. K. Lee and H. R. Allcock, *Solid State Ionics*, 2010, **181**, 1721-1726.

[71] P. G. Bruce and C. A. Vincent, *J. Chem. Soc. Faraday T*, 1993, **89**,

3187-3203.

[72] M. Nakayama, S. Wada, S. Kuroki and M. Nogami, *Energy Environ. Sci.*, 2010, **3**, 1995-2002.

Table 2.1. Synthesis results of the series of linear and branched-graft copolymers with different comonomers feeding ratios.

Samples	Composition (PEGMA : MA-POSS)[a]			$M_w^{b(c)}$	$M_w^{d(e)}$	M_w^b / M_w^d	State[f]
	Feed [mol%]	In polymer [mol%]	In polymer [wt%]	[10^{-3}, RI]	[10^{-3}, MALLS]		
Linear P(PEGMA)	100 : 0	100 : 0	100 : 0	2.4 (1.28)	50.8 (1.03)	0.05	Wax
Branched P(PEGMA)	100 : 0	100 : 0	100 : 0	4.8 (1.50)	177.3 (1.15)	0.03	Wax
BCP9	89 : 11	91 : 9	84 : 16	5.7 (1.53)	152.8 (1.04)	0.04	Sticky film
LCP21	77 : 23	79 : 21	65 : 35	16.4 (1.17)	128.4 (1.35)	0.13	Free-standing film
BCP21	77 : 23	79 : 21	65 : 35	16.2 (1.31)	139.6 (1.08)	0.12	Free-standing film
LCP29	68 : 32	71 : 29	56 : 44	16.6 (1.43)	117.8 (1.15)	0.14	Free-standing film

BCP30	68 : 32	70 : 30	54 : 46	12.3 (1.68)	140.6 (1.18)	0.09	Free-standing film
LCP35	62 : 38	65 : 35	51 : 49	23.6 (1.23)	163.9 (1.01)	0.14	Free-standing film
BCP36	62 : 38	64 : 36	47 : 53	25.8 (1.30)	341.8 (1.07)	0.08	Free-standing film

[a] Determined by ^{1}H NMR. [b] Determined by GPC using refractive index (RI) detector, calibrated with linear polystyrene standards (THF). [c] PDI values determined by GPC using RI detector (THF). [d] Determined by GPC using multi-angle laser light scattering (MALLS) detector (THF). [e] PDI values determined by GPC using MALLS detector (THF). [f] State after cast onto Teflon plate at room temperature.

Table 2.2. Thermal properties of the linear and branched-graft copolymers.

Samples	T_g (°C)[a]	T_g (°C)[b]	T_g (°C)[c]	$T_{d,5\%}$ (°C)[d]	Char yield (%)[e]
Branched P(PEGMA)	-63.4	-41.2	-	289	0.1
LCP21	-64.0	-38.5	78.1	232	0.9
LCP29	-56.7	-36.3	85.2	220	1.0
LCP35	-53.3	-33.2	85.9	212	1.8
BCP21	-67.2	-40.0	76.3	277	0.2
BCP30	-59.4	-38.2	82.6	262	1.1
BCP36	-56.9	-35.6	81.3	244	1.9

[a] T_g of P(PEGMA) segments in polymers. [b] T_g of P(PEGMA) segments in polymers containing LiTFSI ([Li]/[EO] = 0.07). [c] T_g of P(MA-POSS) segments in polymers. [e] The char yield at 700 °C.

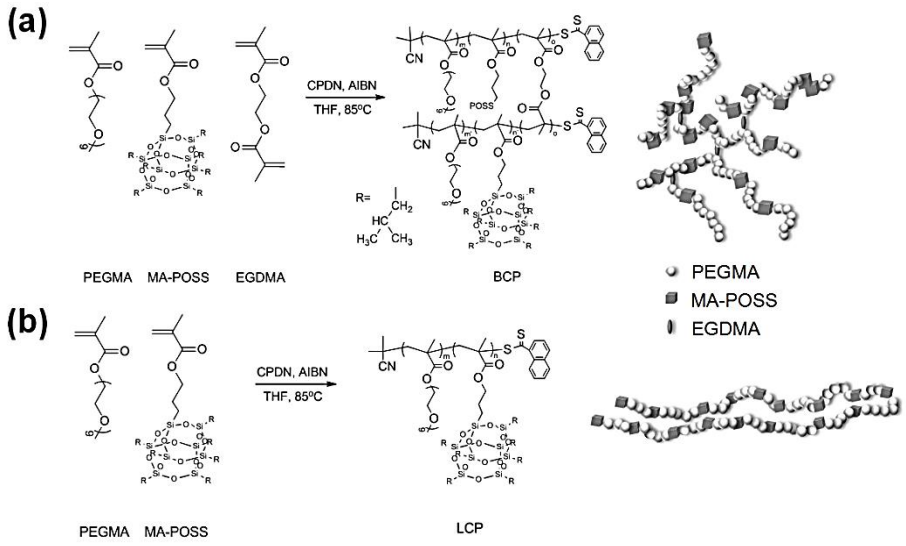

Figure 2.1. Synthesis of (a) branched (BCP) and (b) linear (LCP)-graft copolymers *via* RAFT polymerization.

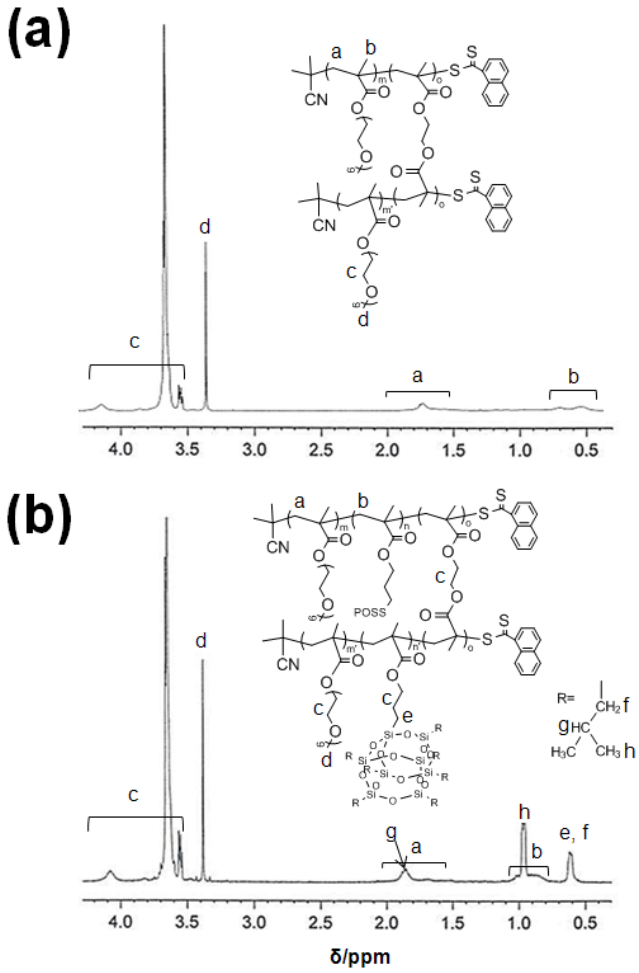

Figure 2.2. ^{1}H NMR spectrum of (a) branched P(PEGMA) and (b) BCP21.

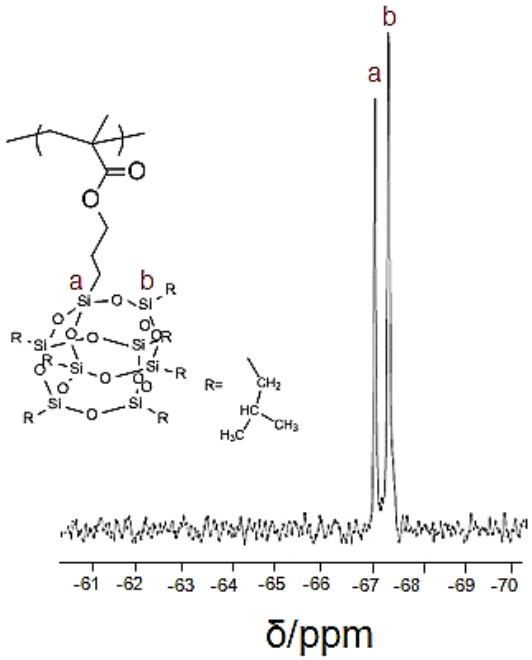

Figure 2.3. ^{29}Si NMR spectrum of BCP21.

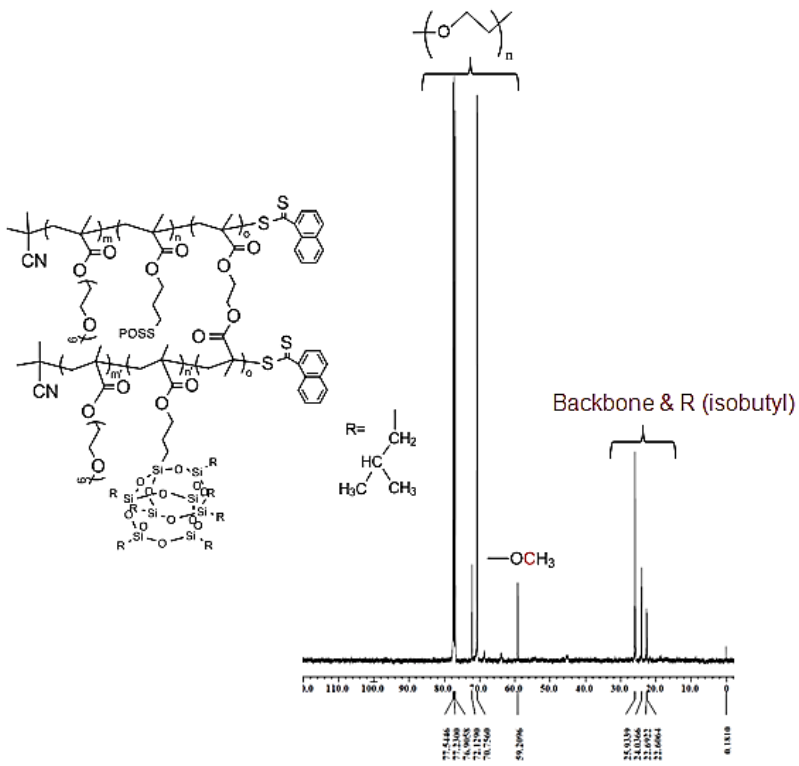

Figure 2.4. ^{13}C NMR spectrum of BCP21.

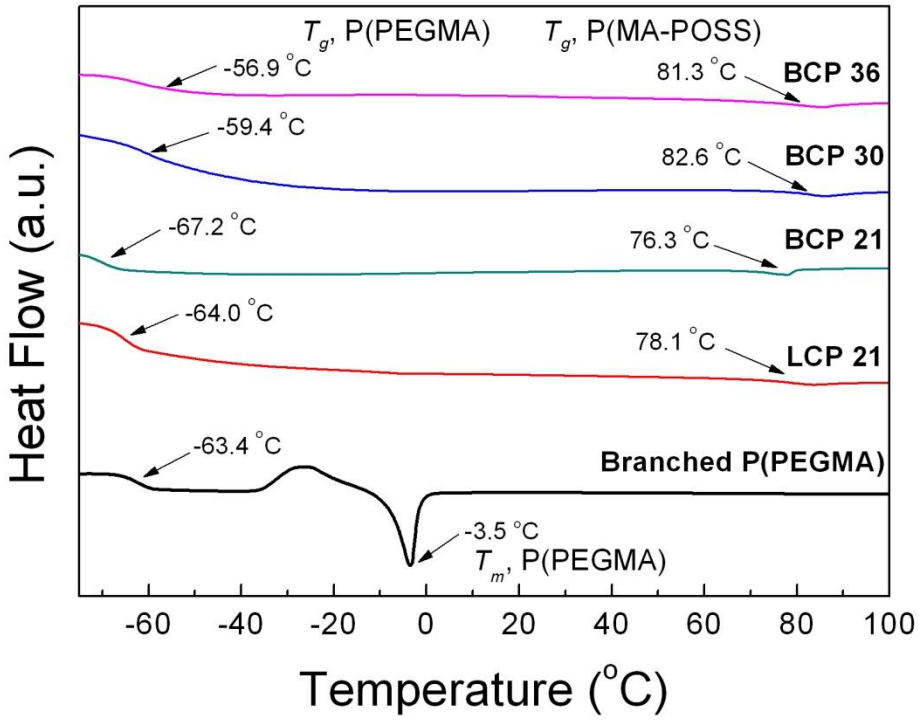

Figure 2.5. DSC thermograms of LCP21 and BCPs.

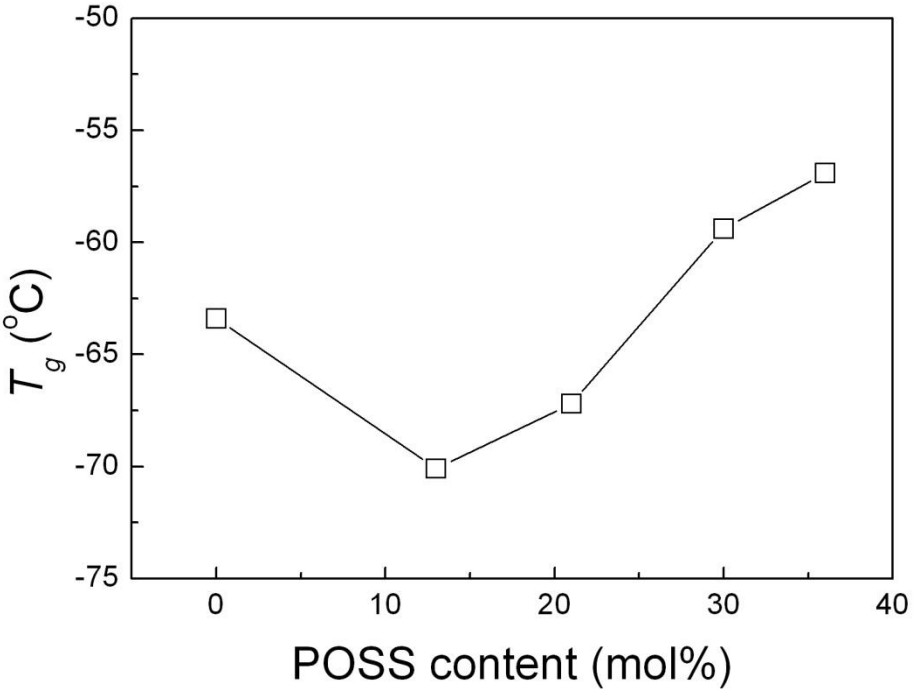

Figure 2.6. T_gs of P(PEGMA) segments in branched copolymers with different POSS contents.

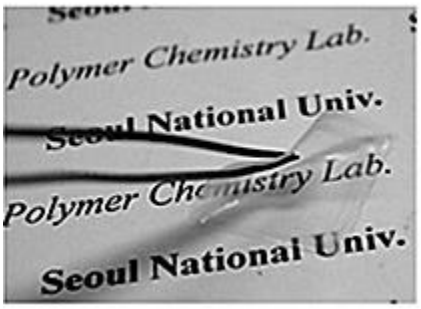

Figure 2.7. BCP21 electrolyte containing LITFSI ([Li]/[EO] = 0.07).

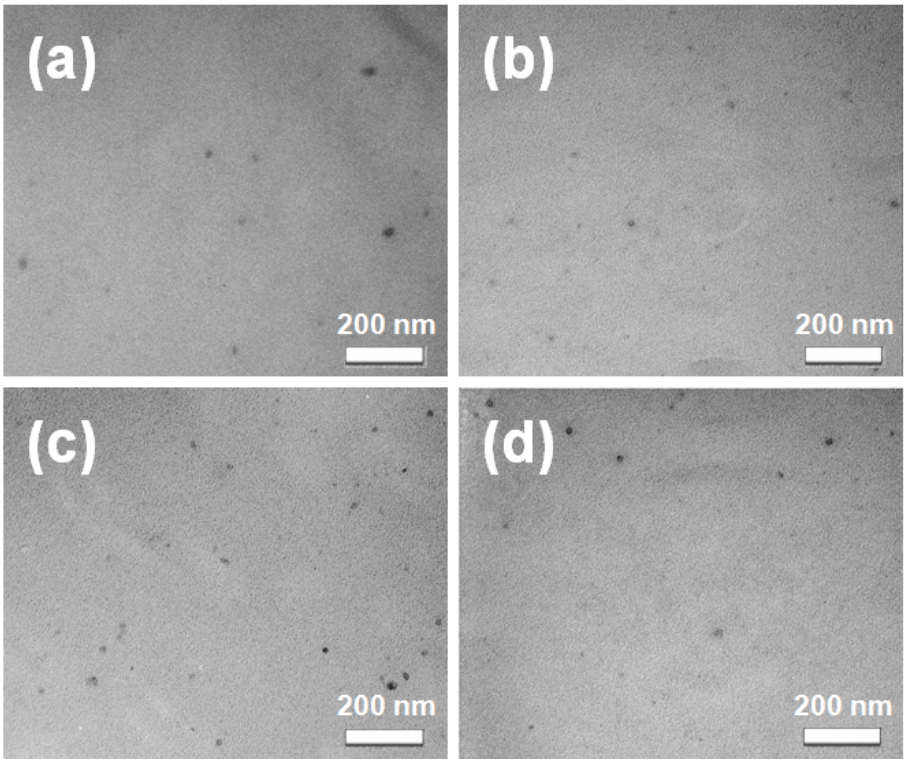

Figure 2.8. TEM micrographs of (a) LCP21, (b) BCP21, (c) BCP30, and (d) BCP36.

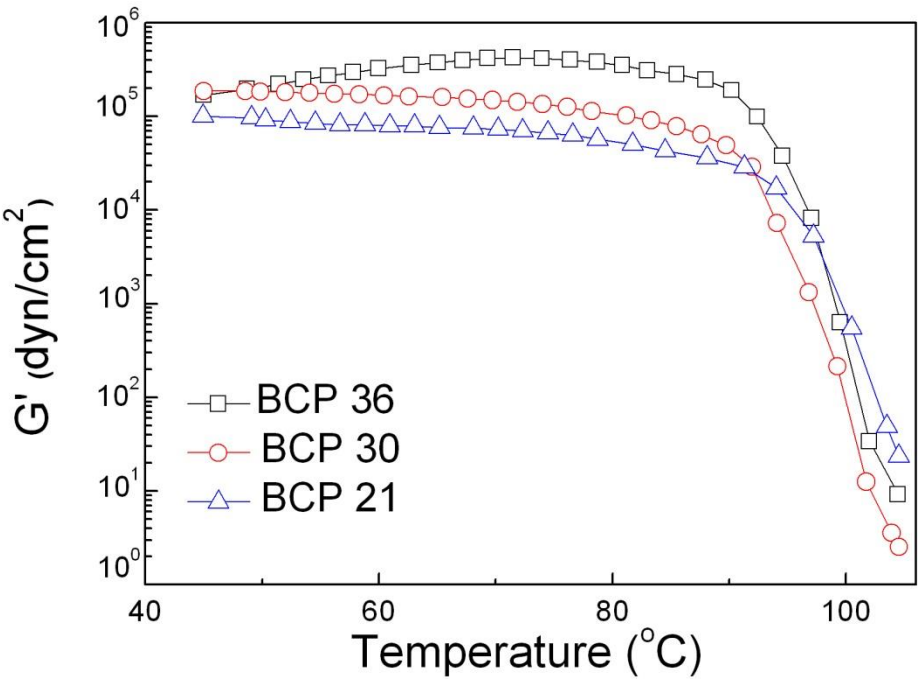

Figure 2.9. Temperature-resolved rheological behaviors of BCP21, BCP30, and BCP36 electrolyte films ([Li]/[EO] = 0.07) in the linear viscoelastic region with 0.1 rad s^{-1} of frequency at 1 ^{o}C min^{-1} ramp.

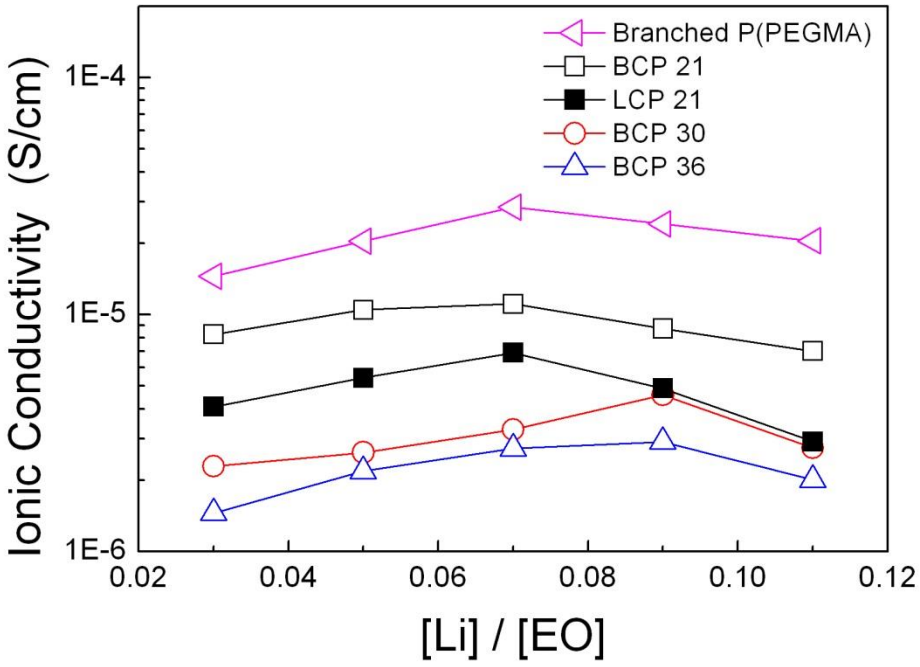

Figure 2.10. Ionic conductivities of LCP21 and BCPs containing LiTFSI with various concentrations at 30 ^{o}C.

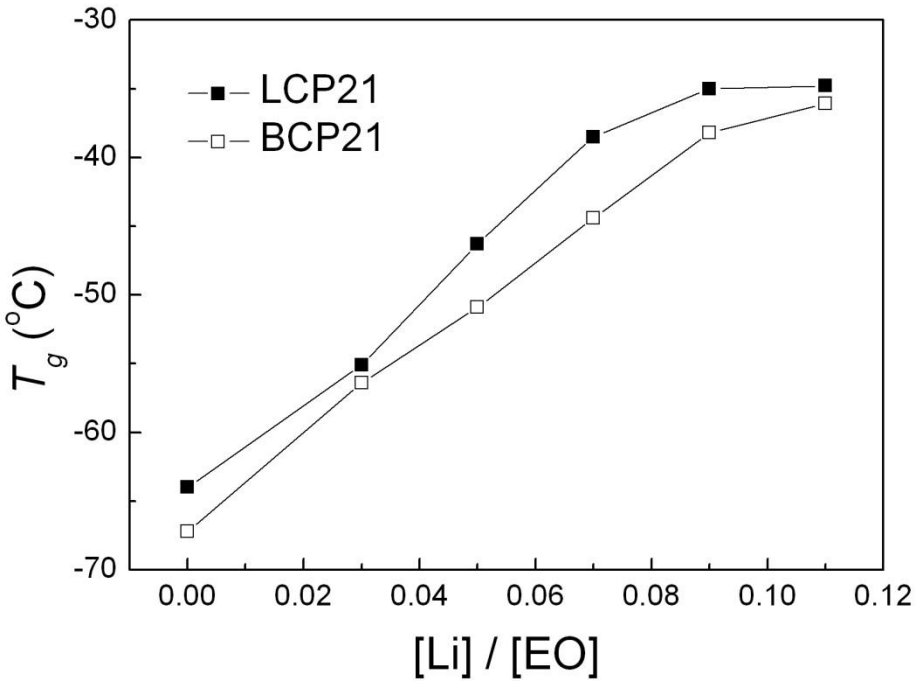

Figure 2.11. Glass transition temperatures of P(PEGMA) segments in LCP21 and BCP21 with various LiTFSI concentrations.

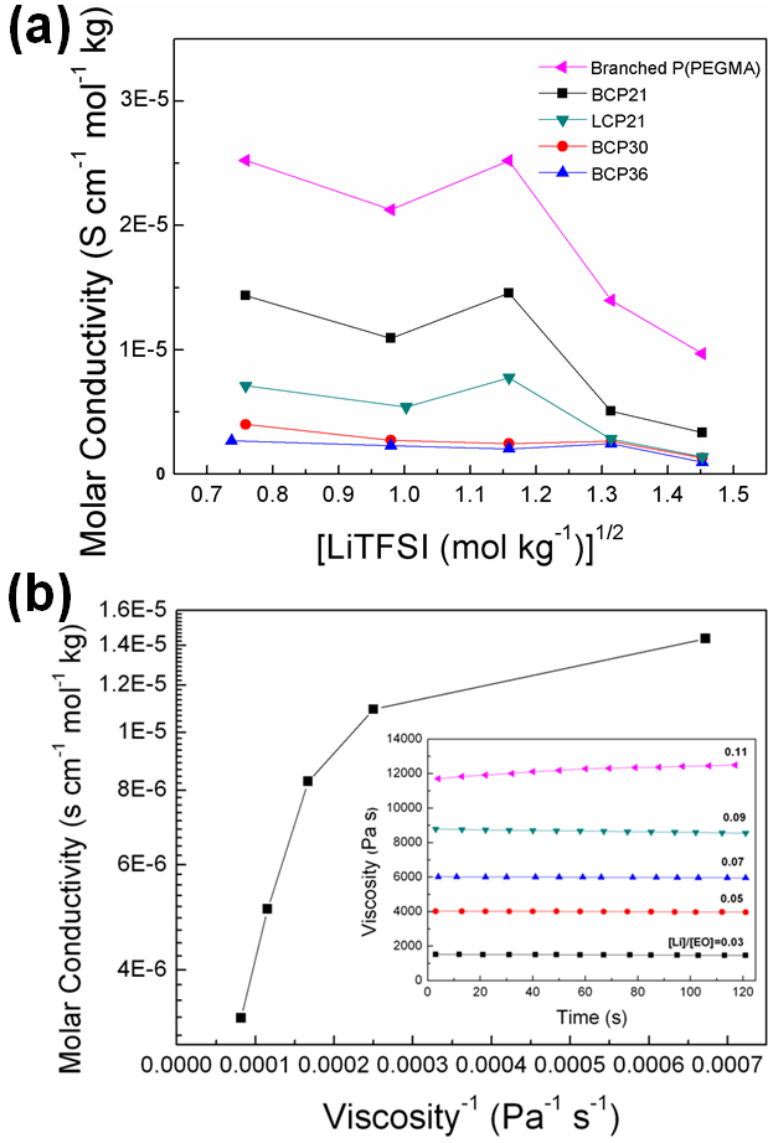

Figure 2.12. (a) Molar conductivities of LCP21 and BCPs containing LiTFSI with various concentrations at 30 ^{o}C and (b) Walden plot of BCP21 electrolytes with varying LiTFSI concentration (Inset image: shear viscosity with time).

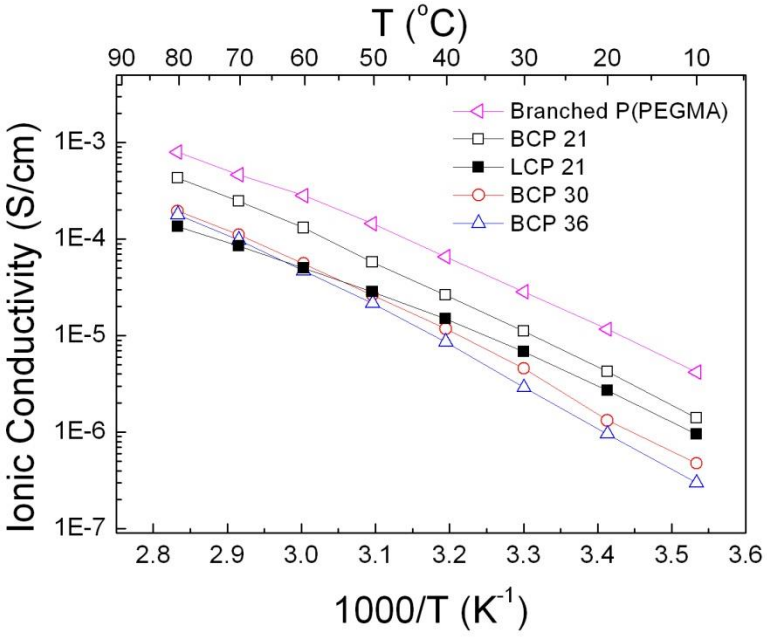

Figure 2.13. Temperature dependence of ionic conductivities of LCP21 and BCPs, where each electrolytes contains same lithium salt concentration ([Li]/[EO] = 0.07).

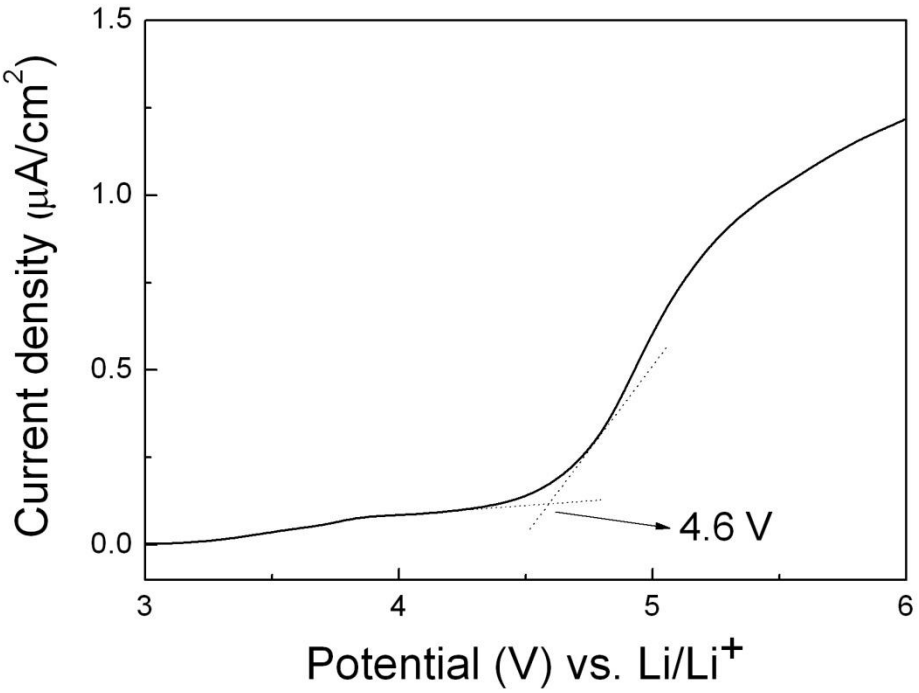

Figure 2.14. Linear sweep voltammogram of BCP21 ([Li]/[EO] = 0.07) at 60 ^{o}C with scan rate of 1 mV/s.

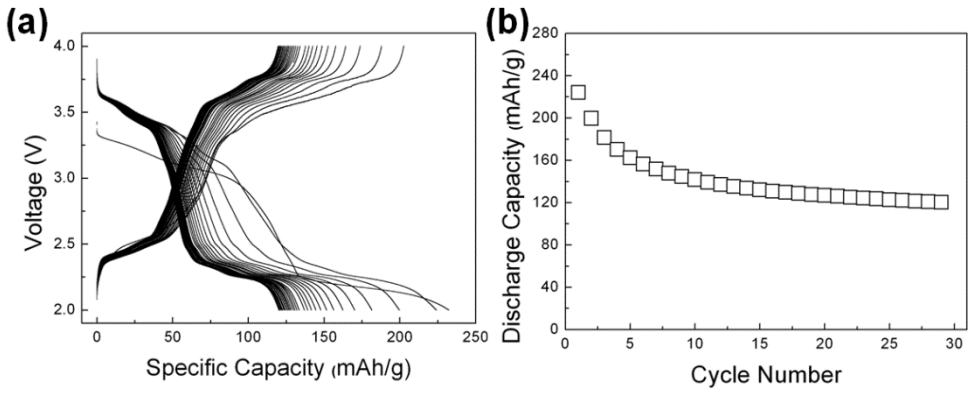

Figure 2.15. (a) Charge/discharge curves and (b) discharge capacity profiles of all-solid-state Li/BCP21/V_2O_5 cell cycled at 60 ^oC (0.1C).

Chapter 3

Dendrite Suppression by Synergistic Combination of Solid Polymer Electrolyte Crosslinked with Natural Terpenes and Lithium Powder Anode for Lithium Metal Batteries

3.1. Introduction

Lithium rechargeable batteries have been intensively studied, because they are one of the most important constituents of energy storage devices such as portable electronics, electric vehicles, and energy storage systems during the last several decades.[1] Recently, lithium metal batteries (LMBs) including lithium-air and lithium-sulfur batteries have been paid much attention for next-generation of battery system, because lithium can generate high specific capacity (3860 mAh/g) and low redox potential (-3.04 V *vs*. standard hydrogen electrode) compared to most of the other electrode materials.[2] However, several disadvantages of LMBs ascribed from the nature of lithium metal itself have hindered their practical applications in the energy systems. Since lithium metal is very reactive with most of the chemical species in battery components, inhomogeneous solid electrolyte interphase (SEI) layer can be easily formed on the lithium metal.[2] Furthermore, lithium dendrites can be easily formed and inevitably grown on the surface of lithium metal during repetitive charge/discharge cycles, because current density can be localized at the inhomogeneous SEI layer.[2] The lithium dendrites eventually

penetrate through the separator immersed with liquid electrolyte leading to an internal short-circuit of the battery, thereby causing the overheat and thermal runaway.[3]

Among various strategies for suppressing the formation and growth of lithium dendrites, controlling the morphology of lithium,[4] mechanical surface treatment of lithium,[5] introduction of conductive scaffolds,[6] and coating the lithium surface with protective layers[7] have been suggested as possible solutions. It was also found that lithium powder anode can show improved cycle performance compared to those of the conventional lithium foil anode systems, because large surface area of lithium powder can decrease effective current density and then uniform lithium dissolution/deposition behavior of lithium can be achieved, resulting in the suppression of the formation and growth of lithium dendrites.[4]

Another obstacles to prevent practical applications of LMBs are the safety problems such as leakage and explosion caused by liquid electrolytes especially at elevated temperature.[8] It is also known that the formation and growth of lithium dendrites is accelerated in the LMBs when the liquid electrolytes are used.[5c] To increase the utilization of LMBs including high-temperature applications, solid

polymer electrolytes (SPEs) based on ion-conducting poly(ethylene oxide) (PEO) derivatives have been intensively studied, because the SPEs form stable SEI layer on lithium metal anode and act as a mechanical barrier against the dendrite growth.[9] However, low ionic conductivity and poor dimensional stability of linear PEO derivatives can limit the practical SPE applications.[8, 9b, 10] The low ionic conductivity of SPEs could be increased using short PEO into the side chain of the polymers, while this can further decrease the dimensional stability.[10] The dimensional stability of the polymers including the PEO derivatives can be improved by crosslinking technology using various commercialized crosslinkers.[9h, 11] However, commercially available crosslinkers are often derived from petroleum-based sources which have resource limitation issues in the near future. Furthermore, ultraviolet (UV) light irradiation or high temperature conditions are often required to produce crosslinked polymer which are considered as energy-consuming processes.

Herein, we prepared all-solid-state lithium powder battery having a SPE crosslinked with natural terpenes, limonene and geraniol, by thiol-ene click reaction under mild condition for the first time (Figure 3.1). Eco-friendly click chemistry based on natural and renewable resources

such as sunlight and terpenes was introduced to suggest green method to prepare SPEs. The effects of structure of terpene crosslinkers, physical state of electrolytes, and morphology of lithium metal anode on the electrochemical properties and dendrite growth behavior were systematically studied. Interestingly, the SPEs crosslinked by terpenes were found to be effective to suppress the lithium dendrite growth especially when they were coupled with a lithium powder anode. To the best of our knowledge, it is the first report on all-solid-state lithium powder battery showing excellent cycle performance and suppressed dendrite growth.

3.2. Experimental

3.2.1. Materials

(3-Mercaptopropyl)methyldimethoxysilane, (3-mercaptopropyl)trimethoxysilane, limonene, and geraniol were purchased from Alfa Aesar and used as received. Poly(ethylene glycol) methyl ether (average M_n = 350 g mol^{-1}), allyl bromide, and 2,2-dimethoxy-2-phenylacetophenone) were purchased from Aldrich and

used as received. Lithium bis(trifluoromethane sulfonyl)imide (LiTFSI, >98%, TCI) was dried under high vacuum at 130 ^{o}C for 24 h and subsequently placed in an argon filled glove box. All other reagents and solvents were obtained from reliable commercial sources and used as received.

3.2.2. Synthesis of branched polysiloxane having thiol group (BPT)

Branched polysiloxane having thiol group (BPT) was synthesized by acid-catalyzed hydrolysis and condensation reaction. Hydrochloric acid (5.2 g, 0.052 mol) was dissolved in a mixed solvent (water-ethanol mixture) and resultant solution was added to a 100 mL of one-neck round bottomed flask equipped with a magnetic stirring bar. (3-Mercaptopropyl)methyldimethoxysilane (1.8 g, 0.01 mol) and (3-mercaptopropyl)trimethoxysilane (2.0 g, 0.01 mol) were added to the solution and then heated at 50 ^{o}C for 3 h in an oil bath under nitrogen atmosphere. The crude product was distillated at 80 ^{o}C under vacuum to remove the solvent. Excessive monomers were removed by precipitation of the crude solution in distilled water. After being dried

under vacuum at room temperature for 24 h, viscous and transparent oil was obtained with 75 % yield. For the convenience, branched polysiloxane having thiol group is abbreviated as BPT. ^{1}H NMR (300 MHz, $CDCl_3$, δ] of BPT: 2.55 (Si-CH_2-CH_2-C*H*$_2$-SH), 1.67 (Si-CH_2-C*H*$_2$-CH_2-SH), 1.35 (-S*H*), 0.62 (Si-C*H*$_2$-CH_2-CH_2-SH), 0.12 (Si-C*H*$_3$). ^{29}Si NMR (400 MHz, $CDCl_3$, δ] of BPT: -15.8 (D) and -68 (T).

3.2.3. Synthesis of allyl poly(ethylene oxide) (allyl PEO)

Poly(ethylene glycol) methyl ether (35 g, 0.10 mol) and allyl bromide (13 g, 0.11 mol) were reacted under the presence of sodium hydroxide (4.4 g, 0.11 mol) in distilled toluene at 45 ^{o}C for 16 h. The residual solvent was removed under reduced pressure by evaporation. Crude product was dissolved in dichloromethane and extracted with distilled water three times. After being dried under anhydrous magnesium sulfate, transparent liquid was obtained with 92 % yield. For the convenience, allyl poly(ethylene oxide) is abbreviated as allyl PEO. ^{1}H NMR (300 MHz, $CDCl_3$, δ] of allyl PEO: 5.92 (vinyl, C*H*$_2$), 5.25 (vinyl, C*H*), 4.11 (CH_2=CH-C*H*$_2$-O), 3.57-3.77 (C*H*$_2$-C*H*$_2$-O), 3.38 (C*H*$_3$-O).

3.2.4. Synthesis of branched polysiloxane having PEO side chains (BPTP100)

BPT (0.5 g, 3.6 mmol of thiol group), allyl PEO (1.81 g, 4.6 mmol), and 2,2-dimethoxy-2-phenylacetophenone (DMPA) (0.09 g, 0.35 mmol) were dissolved in 0.5 mL of distilled THF and stirred for 10 min under irradiation of UV light (OV-11 ultraviolet lamp, 60 Hz, FORCELAMP Co., LTD, Korea). Excessive allyl PEO was removed by precipitation of the crude product in *n*-hexane three times. After being dried under vacuum at room temperature for 24 h, viscous wax was obtained with 95 % yield. For the convenience, branched polysiloxane having PEO side chains is abbreviated as BPTP100, where 100 indicates that 100 mol% of thiol group in BPT is substituted by the allyl PEO, which is confirmed from the ^{1}H NMR result. ^{1}H NMR (300 MHz, $CDCl_3$, δ] of BPTP100: 3.57-3.77 (C*H*$_2$-C*H*$_2$-O), 3.38 (C*H*$_3$-O), 2.55 (Si-CH$_2$-CH$_2$-C*H*$_2$-S-), 1.85 (Si-CH$_2$-C*H*$_2$-CH$_2$-S-), 0.62 (Si-C*H*$_2$-CH$_2$-CH$_2$-S-), 0.11 (Si-C*H*$_3$).

3.2.5. Preparation of solid polymer electrolytes (SPEs): L-

BPTPs and G-BPTPs

SPEs were prepared by thiol-ene click reaction under light irradiation. BPT (0.1 g, 0.72 mmol of thiol group), allyl PEO (0.07 g, 0.181 mmol), limonene (0.037 g, 0.271 mmol), LiTFSI (0.018497 g, [Li]/[EO] = 0.07), and DMPA (0.00824 g, 0.0321 mmol) were dissolved in 0.5 mL of distilled THF. The solution was cast onto a glass plate (2.5 × 2.5 cm^2) and the THF solvent was removed under ambient condition. Subsequently, florescent lamp (BT-36DP, 36 W, SUNSEA Co., LTD, Korea) was irradiated to the glass plate for 12 h. The film was peeled from the glass plate and the resultant film was dried under high vacuum condition for a week at 60 ^oC prior to further characterization. Other SPEs having different PEO content and crosslinking density were also prepared using the same procedure except the feed ratio of allyl PEO and limonene. SPEs crosslinked with geraniol instead of limonene were also prepared using the same procedure. For the convenience, SPEs crosslinked with limonene and geraniol are abbreviated as L-BPTPs and G-BPTPs, respectively. Especially when the feed molar ratios of allyl PEO to terpene were 25:75, 50:50, and 75:25, they were named as L-BPTP25 (or G-

BPTP25), L-BPTP50 (or G-BPTP50), and L-BPTP75 (or G-BPTP75), respectively. And the numbers in the abbreviations represent mol% of allyl PEO group (Table 3.1). SPEs could be also prepared by irradiation of UV light or natural sunlight. When UV light was used, the dimensionally stable SPEs could be prepared by less than 30 min of irradiation. Since the energy from sunlight varies by the weather conditions, the irradiation time for the preparation of the dimensionally stable SPEs should be changed. For example, when the outside temperature was about 26~38 ^{o}C at summer period on the rooftop of building 302 at Seoul National University in Korea (latitude: 37^{o}26'55.94"N, longtitude: 126^{o}57'7.55"E), about 2 h of irradiation was required for the sample preparation.

3.2.6. Preparation of lithium powder anode

Lithium powder was prepared by droplet emulsion technique (DET). Molten lithium was dispersed in silicon oil at 190 ^{o}C and sheared at 30000 rpm for 3 min to produce an emulsion. After the temperature of emulsion was cooled down to room temperature, solidified lithium droplets were obtained. Lithium powder was separated from the

silicon oil and washed with *n*-hexane several times and dried under high vacuum condition for 24 h at 60 ^{o}C. 13 mg of lithium powder was pressed to a coin shape (diameter: 15 mm, thickness: 220 μm) on a stainless-steel mesh by applying a pressure of about 1 MPa, and then lithium powder anode having conventional disc form was obtained. For the evaluation of dendrite growth and cycle performance of the cell having a SPE (G-BPTP75), the obtained lithium powder anode was coated with G-BPTP75 electrolyte solution comprising BPT (8.0 mg), allyl PEO (17 mg), geraniol (1.1 mg), LiTFSI (2.3 mg, [Li]/[EO] = 0.07), and DMPA (0.8 mg) dissolved in 20 uL of distilled THF *via* solution casting followed by UV curing for 30 min.

3.2.7. Cell fabrication and electrochemical characterization

Ionic conductivities of the SPEs were measured by complex impedance spectroscopy between 10 to 100 ^{o}C with a Zahner Electrik IM6 apparatus in the frequency range of 0.1 Hz to 1 MHz and an applied voltage of 10 mV. The real part of the impedance at the minimum of imaginary part was used as the resistance to calculate the conductivity of the SPEs. The samples for the measurements were

prepared by sandwiching the SPEs between two stainless-steel electrodes. Each sample was allowed to equilibrate for 30 min at each temperature prior to taking the measurements. The ionic conductivity (σ) was calculated from the electrolyte resistance (R) obtained from the impedance spectrum, the electrolyte thickness (d) and the area of the electrode (A) using the equation, $\sigma = (1/R) \times (d/A)$. The electrochemical stability of the electrolytes was evaluated using linear sweep voltammetry (LSV). The cell was assembled by sandwiching electrolyte between stainless steel (working electrode) and lithium metal (reference electrode) in a 2032 coin cell. The cell was swept in the potential range from 3 V to 7 V (vs. Li/Li^+) at a scan rate of 1 mV/s at 60 ^oC. Glavanostatic charge/discharge test was carried out to evaluate dendrite growth behavior. Time evolution of voltage was measured on a symmetric lithium cell during repetitive charge/discharge cycles, where the cell was cycled under constant current density of 0.2 mA/cm^2 and the polarity was reversed for every 3 h. Rest time was given as 10 min before reversing the polarity to alleviate the influence of concentration gradients. Charge/discharge test of all-solid-state lithium-ion battery was performed with WBSC3000 battery cycler (WonATech) with cutoff voltages of 2.0 ~

3.6 V (vs. Li/Li^+) at 60 ^oC. LiV_3O_8 (70 wt%) prepared as previously described[11a] was used as cathode active materials and dispersed in *N*-methyl-2-pyrrolidone with Super P (20 wt%) and PVDF (10 wt%). The cathode was coated with electrolyte (G-BPTP75) solution comprising BPT (10 mg), LiTFSI (2.9 mg, [Li]/[EO]=0.07), allyl PEO (21 mg), geraniol (1.4 mg), and DMPA (1.0 mg) dissolved in 0.2 mL of distilled THF *via* solution casting followed by UV curing for 30 min. The coated cathode was dried under high vacuum at 120 ^oC for 24 h prior to test. LiV_3O_8 cathode, lithium metal anode (foil or powder), and SPE were punched into disks and assembled together in a 2032 coin cell. In case of coin cell containing liquid electrolyte, Celgard 2320 was used as a separator and 1 M $LiPF_6$ in EC:DEC (1:1 vol%) was used as a liquid electrolyte instead of SPE. All components were assembled in argon filled glove box (H_2O < 0.5 ppm, O_2 < 0.5 ppm).

3.2.8. Characterizations

^1H NMR spectra were recorded on an AscendTM 400 spectrometer (300 MHz) using $CDCl_3$ (Cambridge Isotope Laboratories) as a

solvent at room temperature, with TMS as a reference. ^{29}Si NMR spectra were recorded on JeolJNM-LA400 spectrometer (400 MHz) using $CDCl_3$ (Cambridge Isotope Laboratories) as a solvent at room temperature. Molecular weights (M_n, M_w) and polydispersity index (PDI) were analyzed by gel permeation chromatography (GPC) equipped with a Waters 515 HPLC pump and three columns including PLgel 5.0 μm guard, MIXED-C, and MIXED-D from Polymer Laboratories. The refractive index (RI) detector was calibrated using polystyrene standards. The resulting data was analyzed using the Omnisec software. HPLC grade THF (J. T. Baker) was used as the eluent at a flow rate of 1.0 mL min^{-1} at 35 ^{o}C. The glass transition temperatures of the polymers were examined by differential scanning calorimetry (DSC) using TA Instruments DSC-Q1000 under a nitrogen atmosphere. Samples with a typical mass of 5.0-10 mg were encapsulated in sealed aluminum pans. The samples were first heated to 150 ^{o}C and then quenched to -80 ^{o}C followed by a second heating scan from -80 ^{o}C to 150 ^{o}C at a heating rate of 10 ^{o}C min^{-1}. FT-IR spectra were recorded in the absorption mode on Nicolet 6700 spectrophotometer with a resolution of 4 cm^{-1} in the vibrational frequency range from 400 to 4000 cm^{-1}. Field-emission scanning

electron microscopy (FE-SEM) was performed on a JEOL JSM-6700F with an accelerating voltage of 10 kV. Temperature-resolved dynamic mechanical analysis (DMA) was conducted using a Q800 dynamic mechanical analyzer (TA Instruments) with 1 Hz of frequency at 10 ^{o}C/min ramp.

3.3. Results and Discussion

3.3.1. Synthesis and characterization of branched polysiloxane having ion-conducting PEO group

Since polysiloxane derivatives are very flexible due to their low barrier energy to bond rotation (~0.8 kJ/mol), they have high chain mobility to faciliate the ion conduction in the crosslinked polymer structures.[13] Although there have been many reports on the SPEs based on polysiloxane derivatives, petroleum based crosslinkers and expensive transition metal based catalyst were often used to graft functional monomers to the side chain of polysiloxane by hydrosilylation.[11c, 13a] This time, we synthesized a polysiloxane having thiol group that can be prepared by thiol-ene click reaction

between the thiol group and allyl monomers under mild condition without using any transition metal based catalyst. Furthermore, branched structure was introduced to the polysiloxane, because it can enhance ion-conducting ability by increasing free volume of the polymer.[9i] The branched polysiloxane having thiol group (BPT) was synthesized by acid-catalyzed hydrolysis and condensation reaction[14] between (3-mercaptopropyl)methyldimethoxysilane and (3-mercaptopropyl)trimethoxysilane as presented in Figure 3.2. The structure of BPT was confirmed by ^{1}H NMR analysis (Figure 3.3(a)). Proton peaks at 3.5 ppm corresponding to the methoxy group of the silane monomers clearly disappeared after the reaction and new signal assigned to the thiol group appeared at 1.35 ppm. Figure 3.3(b) shows ^{29}Si NMR spectrum of BPT. Two peaks at around -20 ppm and -70 ppm are attributed to the silicon in BPT corresponding to D and T units, respectively, indicating that BPT has a branched structure.[15] Allyl poly(ethylene oxide) (Allyl PEO) was synthesized by Williamson ether synthetic method between allyl bromide and poly(ethylene glycol) methyl ether as shown in Figure 3.2. The structure of allyl PEO was confirmed by ^{1}H NMR analysis (Figure 3.4). Proton peaks (signal a, b, and c) at 4~6 ppm corresponding to the

allyl group were observed, and signals d and e at 3.5~3.8 ppm and 3.38 ppm are assigned to CH_2-CH_2-O and terminal CH_3-O of PEO group, respectively.

To impart ion-conducting property to the BPT, thiol groups of BPT were substituted by allyl PEO. Excessive amount of allyl PEO was reacted with BPT to achieve 100 % conversion of the thiol group to PEO group *via* thiol-ene click reaction (Figure 3.5). ^{1}H NMR spectrum of the product shown in Figure 3.6 clearly indicates the 100 % conversion. The thiol groups of pristine BPT at 1.33 ppm disappered after the PEO grafting, and proton peaks corresponding to the PEO side chains were obsereved. Since 100 % of thiol group is substituted by PEO group, the resulting product was named as BPTP100. BPTP100 exhibits a liquid state as shown in photograph of Figure 3.5. It was also found that molecular weight of BPTP100 is obviously higher than that of BPT, because PEO groups are attached to the side chain of BPT as shown in GPC profiles (Figure 3.7). The temperature dependene of ionic conductivity of BPTP100 containing LiTFSI ([Li]/[EO]=0.07) was measured and it was found that the ionic conductivity at 30 ^{o}C was 1.5×10^{-4} S/cm (Figure 3.8).

3.3.2. Preparation of solid polymer electrolytes (SPEs) via thiol-ene click reaction

Since BPTP100 has a liquid state, it cannot be directly used as the electrolyte without an additional separator although it showed reasonably high ionic conductivity at room temperature. To impart sufficient dimensional stability as a free-standing film, natural terpenes were introduced as crosslinkers. SPEs were prepared by blending BPT as a flexible polymer backbone, allyl PEO as an ion-conducting group, and terpenes (limonene or geraniol) as crosslinkers, followed by thiol-ene click reaction under light irradiation (Figure 3.5(b) and 3.5(c)). Terpenes are naturally occurring organic compounds having isoprene (C_5H_8) units and they are produced by plants or emitted from insects.[16] Since the terpenes have two unsaturated carbon double bonds, they can be reacted with thiol groups through thiol-ene click reaction under light irradiation, leading to the formation of crosslinked polymer network.[17] After the light irradiation, liquid state of BPT was changed to a solid-state by crosslinking process *via* thiol-ene click reaction as shown in photographs of Figure 3.5(b) and 3.5(c). Among various kinds of

terpenes, limonene ($C_{10}H_{16}$) and geraniol ($C_{10}H_{18}O$) were chosen as crosslinkers for this study to investigate the structural effect of terpene crosslinkers on electrochemical properties. Both limonene and geraniol have same number of carbon and two unsaturated carbon double bonds, while limonene is a cyclic compound and geraniol is a linear compound with a hydroxyl end group. Although it might be more proper to use a linear crosslinker without a hydroxyl group, linear terpene counterpart of the limonene without a hydroxyl group is not commercially available.

Among the various methods for the preparation of well-defined crosslinked SPEs including hydrosilylation[11c, 13a] and radical polymerization of methacryl/acryl moieties[9h, 11], we intentionally used the thiol-ene click reaction to prepare the crosslinked SPEs because of its advantegeous features such as being highly efficient, simple to execute with no side products, and proceeding rapidly to high conversion even with relatively small amount of initiators.[18a] Furthermore, since the thiol-ene reaction is insensitive to ambient oxygen or water, it can be readily applied for the commercialized process for the production of the SPEs.[18a] It was further found that various kinds of light sources such as fluorescent lamp, UV lamp, and

even natural sunlight can induce the crosslinking reaction between the thiol and unsaturated hydrocarbon groups of terpenes due to highly reactive and efficient nature of thiol-ene click reaction.[17a, 18] Figure 3.9 shows photographs of light irradiation with various light sources. Although the UV light can induce the crosslinking reaction within relatively short reaction time (~30 min), fluorescent lamp and sunlight-induced processes are eco-friendly approaches that do not require any excessive power. We found that natural sunlight irradiation can successfully produce the well-defined crosslinked SPEs having sufficient dimensional stability within about 2 h, especially in sunny days in June to August at rooftop of building 302 in Seoul National University (latitude: 37°26’55.94”N, longtitude: 126°57’7.55”E) (Figure 3.9(a)). The temperature and cloud amount at the period are provided in Figure 3.10. However, since the intensity of the sunlight often changes throughout the year depending on the weather conditions, reproducible crosslinking process was performed using a fluorescent lamp that we can control the irradiation intensity inside the laboratory. The fluorescent lamp requires 12 h of irradiation time to produce SPEs. Although there is a difference in irradiation time depending on the light sources, it was found that all of these light

sources including natural sunlight, fluorescent lamp, and UV lamp can induce the crosslinking reaction, thereby obtaining equivalent state of SPEs.

SPEs containing various monomeric compositions were prepared by varying the molar ratios of allyl PEO and terpenes (limonene or geraniol) as 25:75, 50:50, and 75: 25 to investigate the effect of monomeric composition on various properties of the SPEs. When the allyl PEO content is larger than 75 mol%, free-standing SPEs could not be obtained, because the physical state of allyl PEO in the liquid state dominates the overall physical state of the SPEs. Thus, maximum allyl PEO content was decided to be 75 mol%. For the convenience, SPEs crosslinked with limonene and geraniol are abbreviated as L-BPTPs and G-BPTPs, respectively, and the numbers in the abbreviations represent the mol% of PEO groups (Table 3.1). The reaction between thiol group of BPT and allyl groups of allyl PEO and terpenes to form SPEs was confirmed by FT-IR spectra as shown in Figure 3.11. The thiol peak of BPT at 2565 cm^{-1} is not observed from all the SPEs after the crosslinking reaction, indicating that a crosslinked polymer network is formed.[19]

Flat surfaces without any wrinkles and pores were observed from the

surface SEM images of the SPEs (Figure 3.12), indicating that macroscopic phase separation or aggregation did not occur in this system.[17a] When the crosslinked SPEs were prepared using methacrylated tannic acid and poly(ethylene glycol) methyl ether methacrylate (PEGMA) according to our previous study, wrinkles and pores were observed on the surface of the SPEs by the phase separation of electrolyte components, because they are not miscible.[11a] This time, the crosslinked SPEs prepared using polysiloxane based BPT and terpene based crosslinker do not show any phase separation behavior, because relatively nonpolar limonene or geraniol can be mixed well in the nonpolar BPT domains. It was reported that polymer electrolytes or separator having pore sizes larger than 1 μm are vulnerable to an internal short-circuit, because such large pores can let the sharp dendrites easily penetrate through the pores.[20] Therefore, pore-free structure of both L-BPTPs and G-BPTPs should be advantageous to prevent the penetration of the dendrite compared to the porous structures.

3.3.3. Ion conduction property

Since chain mobility of ion-conducting PEO group is critical factor affecting ionic conductivity of the SPE, glass transition temperatures (T_gs) of the SPEs having different crosslinkers (limonene or geraniol) and PEO contents were measured using DSC analysis. As shown in Figure 3.13(a), T_g value decreases with the increase of PEO content (or with the decrease of terpene crosslinker content) due to low crosslinking density.[11a] Although the T_g value might be further lowered by increasing the PEO content, free-standing films having dimensional stability could not be obtained when the SPEs were prepared using allyl PEO larger than 75 mol%. Therefore, 75 mol% of allyl PEO is the maximum PEO content for the SPE having sufficient dimensional stability as well as low T_g. Interestingly, T_g values of L-BPTPs are higher than those of G-BPTPs when they have same composition. For example, T_g values of L-BPTP75 and G-BPTP75 are -55.6 ^{o}C and -60.9 ^{o}C, respectively. This result can be ascribed to the different chain mobility caused by the different structure of the crosslinkers; limonene having a cyclic structure and geraniol having a linear structure. The ring structure in limonene can definitely increase the steric hindrance toward the chain mobility, resulting in higher T_g.[17a] Therefore, G-BPTP75 having a linear type of crosslinker

causing less steric hindrance and largest PEO content exhibits lowest T_g value among the series of the SPEs. Others also reported that the structure of the crosslinker affects the glass transition behavior of the crosslinked polymers as our result. [21]

The structure-property relationship revealed in T_g behaviors of L-BPTPs and G-BPTPs was consistent with the ionic conductivity result, because ion conduction of SPE is dominated by chain mobility of the polymer. Figure 3.13(b) shows temperature dependence of ionic conductivities of L-BPTPs and G-BPTPs. In both series, ionic conductivity increases with increasing the PEO content (or decreasing the crosslinker content), because the chain mobility of ion-conducting PEO groups increases, as estimated by the T_g behavior.[11a] In addition, SPE having larger PEO content can contain more lithium ions as charge carriers in the electrolyte system when the lithium salt concentrations is [Li]/[EO]=0.07, thereby increasing the ionic conductivity.[9i] Furthermore, ionic conductivities of G-BPTPs are higher than those of L-BPTPs when they have the same composition as expected from the DSC results; G-BPTPs having a linear geraniol crosslinker exhibit higher chain mobility (lower T_g values), resulting in higher ionic conductivity than L-BPTPs having a cyclic limonene

crosslinker. As a result, the ionic conductivity of G-BPTP75 (8.6×10^{-5} S/cm at 30 ^{o}C) is highest among the series, and this value is about two times higher than that of L-BPTP75 (4.2×10^{-5} S/cm at 30 ^{o}C). Although the maximum ionic conductivity of G-BPTP75 prepared in this study is still lower than those of conventional liquid electrolytes, our liquid-free SPE system should be more suitable for the high-temperature battery applications such as electric vehicle or energy storage system, because it does not have any leakage and explosion problems. Furthermore, formation and growth of dendrites can be significantly suppressed when the SPE was used instead of liquid electrolyte/separator system as will be described in the later part of this paper.

3.3.4. Preparation of lithium powder anode and evaluation of dendrite growth behavior

Figure 3.14 shows the schematic diagram of all-solid-state lithium powder battery containing SPE and lithium powder anode. In this study, firstly, we tried to suppress the formation and growth of lithium dendrites using SPE as the electrolyte instead of conventional liquid

electrolyte/separator system, where G-BPTP75 having the highest ionic conductivity was used as the SPE. Secondly, we tried to use lithium powder as the anode materials instead of commonly used lithium foil anode. Lithium powder anode was prepared by droplet emulsion technique (DET) followed by compression procedure as presented in Figure 3.15(a).[12b] Each lithium powder has a spherical shape with the average diameter of about 10 μm as shown in Figure 3.15(b) and 3.15(c). The lithium powder anode having a conventional disc form was obtained by applying 1 MPa of pressure to these spherical lithium powders on a stainless-steel mesh. The spherical shape of the lithium powders was maintained even after the compression procedure as shown in Figure 3.15(d) and 3.15(e), and this produces a porous structure having a larger surface area than that of the conventional lithium foil anode (Figure 3.16).[12a] The increased surface area of lithium powder anode contributes to decrease effective current density applied to each lithium powder compared to the case of lithium foil anode, and then formation and growth of dendrites can be much suppressed[5c] as will be described in the later part of this paper.

Figure 3.17(a) shows the galvanostatic cycling curves of symmetric

cells prepared using a liquid electrolyte with lithium foil and powder anodes at a current density of 0.2 mA/cm^2. The overpotential value of the cell with lithium powder anode is smaller than that of the cell with lithium foil anode, because large surface area of lithium powder decreases effective current density, thereby suppressing the formation and growth of dendrites.[4, 22] However, even the lithium powder anode showed an continuous increase in the overpotential during cycling, because unstable solid electrolyte interphase (SEI) layer is inevitably formed when the liquid electrolyte is incorporated.[2] Since the SEI layer can be easily cracked and broken down during repetitive lithium dissolution/deposition cycles, inhomogeneous SEI layer on the lithium metal surface induces localized current density, resulting in the formation of the dendrites.[3a] Figure 3.17(c) and 3.17(e) show the lithium dendrites formed and grown on the surfaces of lithium foil and powder anodes, respectively, when the liquid electrolyte is used. After 400 h of cycling, flat and smooth lithium foil (Figure 3.16) was found to be fully covered by the dendrites, while some of the spherical powder still remains and much smaller amount of sharp dendrites were formed on the lithium powder anode, because large surface area of lithium powder anode decreases effective current density,[4, 6]

thereby suppressing the growth of lithium dendrites compared to the lithium foil anode. Still, the formation and growth of dendrites could not be effectively suppressed even with the lithium powder anode, because the liquid state electrolyte cannot impart any physical resistance as a mechanical barrier against the formation and growth of dendrites.

Figure 3.17(b) shows the galvanostatic cycling curves of symmetric cells prepared using G-BPTP75 as the SPE with lithium foil and powder anodes at a current density of 0.2 mA/cm^2. To fill the empty space in a porous lithium powder anode with the SPE as much as possible, G-BPTP75 electrolyte solution was cast onto a ltihum powder anode followed by curing process. Comparing to the cells with the liquid electrolyte, stable cycling behaviors with much smaller overpotential values were observed with the introduction of the SPE. Not much voltage fluctuation was observed, if any, during 400 h, indicating that the formation and growth of lithium dendrites is effectively suppressed by the SPE which covers the surface of lithium anode, because the liquid-free SPE system can significantly hinder the formation of inhomogeneous SEI layer by removing all the reactive liquid components, resulting in delocalized current density.[23]

Furthermore, it has been reported that crosslinked SPE having a modest level of shear modulus (>0.1 MPa) can effectively suppress the dendrite growth.[23] As shown in Figure 3.18, G-BPTP75 has constant G‘ values larger than 9 MPa over the wide range of temperature due to its robust crosslinked structure, implying that the crosslinked structure can impart sufficient mechanical resistance against the dendrite growth. Figure 3.17(d) shows that mossy particles are formed on the surface of lithium foil anode, which is quite different from the dendrites formed on that prepared with liquid electrolyte. In the case of lithium powder anode prepared with the SPE (Figure 3.17(f)), any sharp dendritic particles were not observed, because large surface area of lithium powder decreases effective current density,[5] although most of the lithium powders were crushed or expanded from the pristine powder form. This result implys that the morphology of lithium dendrite is found to be different depending on the combination of electrolyte and lithium anode types, and the formation and growth of dendrites can be significantly suppressed with the synergistic combination of SPE and lihtium powder anode. We believe that this is the first systematic study to show the effect of the physical state of electrolyte (liquid and solid) and lithium anode

materials (foil and powder) on the morphology of the lithium dendrites.

3.3.5. Cycle performance

L-BPTP75 and G-BPTP75, the SPEs used in this study, were found to have electrochemical stability up to 4.5 V from linear sweep voltammetry (LSV) study (Figure 3.19(a)).[9c] Since the operation voltage range of cathode materials, LiV_3O_8, is in the range of 2.0 ~ 3.6 V, there might be no electrochemical oxidative decomposition of electrolyte components during cycling even at high temperature, 60 ^oC. Furthermore, our SPEs can be possibly applied to other conventional 4 V class cathode materials such as $LiCoO_2$ and $LiFePO_4$. It was also found that our SPE system has reduction stability with the lithium metal. As shown in Figure 3.19(b) and 3.19(c), reversible lithium deposition/dissolution behavior at around 0 V (*vs.* Li/Li^+) in the cathodic cyclic voltammetry scan was observed from both L-BPTP75 and G-BPTP75.

Figure 3.20(a) shows cycle performance of lithium (foil or powder)/electrolyte (liquid electrolyte or SPE)/LiV_3O_8 cells at 60 ^oC

with a scan rate of 0.1 C. Voltage-capacity curves of each cell are provided in Figure 3.21. LiV_3O_8 was chosen as a cathode active material, because of its large capacity (280 mAh/g) compared to other conventional cathode materials such as $LiCoO_2$ (150 mAh/g) and $LiFePO_4$ (170 mAh/g). As shown in Figure 3.20(a), the initial capacity values of the cells with liquid electrolyte are very close to the theoretical capacity value of cathode active materials, LiV_3O_8 (280 mAh/g), and this value is higher than those of the cells with SPE due to high ionic conductivity of liquid electrolyte.[11a] However, the cells with liquid electrolyte show relatively poor capacity retention behavior compared to the cells with SPE, even with the lithium powder anode, because inhomogeneous SEI layer induced by liquid electrolyte generates lithium dendrites. Furthermore, it was further revealed that a difference in capacity between the cell having SPE/Powder and SPE/Foil is relatively smaller than that between the cell having Liquid electrolyte/Powder and Liquid electrolyte/Foil, implying that introduction of SPE gives more dominant effect on the cycle performance than the lithium powder anode.

The cycle performance of the cells with different configurations could be correlated well with the surface morphology of lithium

anodes after 50 cycles (Figure 3.20(b)~3.20(e)).[22] In the surface images of the cells prepared using a liquid electrolyte with lithium foil and powder (Figure 3.20(b) and 3.20(d)), the lithium powder anode shows smaller dendrites compared to the lithium foil anode, indicating that the growth of dendrites are suppressed on the powder anode, because large surface area of powder anode decreases effective current density.[4, 6] Still, lithium dendrites are inevitably formed from the cells with the liquid electrolyte even with the powder anode, especially at high temperature, 60 ^{o}C, because formation of inhomogeneous SEI layer induces localized current density. Furthermore, dead lithium isolated from the sharp lithium dendrites can easily penetrate through the electrolyte in the liquid state and absorb the liquid electrolyte, resulting in capacity decay.[25] On the contrary, any sharp dendrite particles are not observed from the cells with SPE as shown in Figure 3.20(c) and 3.20(e). In case of the cell prepared using a SPE with lithium foil (Figure 3.20(c)), although the small mossy particles were formed, they are not as sharp as that formed in the cell prepared using a liquid electrolyte with lithium foil. The pristine spherical shape of the lithium powder anode was found to be slightly expanded during repetitive lithium deposition and

dissolution processes (Figure 3.20(e)), while the original state of the lithium powder is maintained for some degree. In contrast, the cell prepared using liquid electrolyte with lithium powder anode (Figure 3.20(d)) does not show any remaining spherical shapes.

The results on cycle performance and dendrite growth are consistent well with electrochemical impedance spectra of the cells obtained before and after cycling (Figure 3.22). It was found that bulk and interfacial resistances of the cells having liquid electrolyte are quite smaller than those of the cells having SPE before cycling due to the high ionic conductivity of liquid electrolyte. However, after 50 cycles, the interfacial resistances of the cells having liquid electrolyte become larger than those of the cells having SPE that is ascribed from the formation of unstable SEI layer as well as dendrite growth. Among various cell configurations, the cell having SPE/Powder exhibits less increase in interfacial resistance, indicating the synergistic combination effect of SPE and powder anode. The stability of the cell having SPE/Powder was further evaluated by observing SEM images (Figure 3.23(a) and 3.23(b)) of the SPE by disassembling the cell after 50 cycles; any pinholes or cracks by the dendrites were not observed on the surface of G-BPTP75 after the cycling, indicating that the

robust crosslinked structure of G-BPTP75 can impart mechanical resistance against the growth and penetration of the dendrites. Furthermore, it was also found that there is no significant change in FT-IR spectra of G-BPTP75 before and after cycling, indicating that the chemical structure of G-BPTP75 also retained well during cycling (Figure 3.23(c)). Meanwhile, coulombic efficiencies of all batteries were retained well throughout the cycles (Figure 3.24), which reflects the good charge transfer reversibility. Among them, the cell with SPE/powder exhibits highest coulombic efficiencies during cycles, because possible side reactions including formation of inhomogeneous SEI, dendrites, and dead lithium are much suppressed [26] with the introduction of SPE/powder as aforementioned. Furthermore, since our system can be also compatible with other cathode materials if the operation voltage range is in the range of ~4.5 V as estimated by the LSV result, all-solid-state lithium powder battery prepared from $LiFePO_4$/G-BPTP75/lithium powder also shows reasonable cycle performance (Figure 3.25).

We also tried to operate the cells at higher C-rate than 0.1 C, while reproducible results were not obtained possibly due to large interfacial resistance between the SPE and electrodes. Similarly, many of other

all-solid-state lithium battery cells using SPE as the electrolyte without using any of liquid electrolytes and/or plasticizers either in electrodes or in polymer system also show their cycle performance results at low C-rates such as 0.1 C as ours due to the same reasons.[27] Further works to overcome the poor rate property of the all-solid-state lithium battery system by controlling the interface between SPE and electrodes and changing binder materials are under progress. Still, it is clearly demonstrated that all-solid-state battery systems containing lithium powder anode and SPE, G-BPTP75, without any liquid or volatile materials exhibit stable capacity retention at high temperature, 60 ^{o}C.

3.4. Conclusions

All-solid state lithium powder batteries comprising lithium powder anode and polysiloxane based SPEs crosslinked with naturally occurring terpenes, limonene and geraniol, were prepared. The effects of structures of terpene crosslinkers, the physical state of electrolytes, and the morphology of lithium metal anode on the electrochemical properties and dendrite growth behavior were systematically studied.

The ionic conductivity of SPE having a linear geraniol crosslinker is higher than that of SPE having a cyclic limonene crosslinker, because linear structure of geraniol provides reduced steric hindrance compared to cyclic limonene with a ring strain. Lithium dendrite growth was effectively suppressed using lithium powder anode due to uniform lithium dissolution/deposition behavior of lithium powder. As a result, the combination of SPE and lithium powder anode gives synergistic effect on cycle performance with much suppressed dendrite growth. To the best of our knowledge, it is the first time to report all-solid-state lithium powder battery comprising SPE crosslinked with natural terpene and lithium powder anode that can suppress the lithium dendrite growth.

3.5. References

[1] a) B. Scrosati and J. Garche, *J. Power Sources* **2010,** *195*, 2419; b) J. B. Goodenough and K. S. Park, *J. Am. Chem. Soc.* **2013,** *135*, 1167.

[2] a) X. B. Cheng, R. Zhang, C. Z. Zhao, F. Wei, J. G. Zhang and Q. Zhang, *Adv. Sci.* **2016,** *3*, 1500213; b) W. Xu, J. L. Wang, F. Ding, X. L. Chen, E. Nasybutin, Y. H. Zhang and J. G. Zhang, *Energy Environ.*

Sci. **2014,** *7*, 513; c) Z. Li, J. Huang, B. Y. Liaw, V. Metzler and J. B. Zhang, *J. Power Sources* **2014,** *254*, 168.

[3] T. M. Bandhauer, S. Garimella and T. F. Fuller, *J. Electrochem. Soc.* **2011,** *158*, R1.

[4] a) J. S. Kim and W. Y. Yoon, *Electrochim. Acta* **2004,** *50*, 531; b) J. S. Kim, W. Y. Yoon, K. Y. Yi, B. K. Kim and B. W. Cho, *J. Power Sources* **2007,** *165*, 620; c) Y. S. Lee, J. H. Lee, J. A. Choi, W. Y. Yoon and D. W. Kim, *Adv. Funct. Mater.* **2013,** *23*, 1019.

[5] a) M. H. Ryou, Y. M. Lee, Y. J. Lee, M. Winter and P. Bieker, *Adv. Funct. Mater.* **2015,** *25*, 834; b) J. Park, J. Jeong, Y. Lee, M. Oh, M. H. Ryou and Y. M. Lee, *Adv. Mater. Interfaces* **2016,** *3*, 1600140.

[6] a) R. Zhang, X.-B. Cheng, C.-Z. Zhao, H.-J. Peng, J.-L. Shi, J.-Q. Huang, J. Wang, F. Wei and Q. Zhang, *Adv. Mater.* **2016**, *28*, 2155; b) Y. Sun, G. Zheng, Z. W. She, N. Liu, S. Wang, J. Sun, H. R. Lee and Y. Cui, *Chem* **2016**, *1*, 287; c) R. Zhang, N.-W. Li, X.-B. Cheng, Y.-X. Yin, Q. Zhang and Y.-G. Guo, *Adv. Sci.* **2017**, *4*, 1600445.

[7] a) W. K. Shin, A. G. Kannan and D. W. Kim, *ACS Appl. Mater. Interfaces* **2015,** *7*, 23700; b) S. H. Lee, J. R. Harding, D. S. Liu, J. M. D'Arcy, Y. Shao-Horn and P. T. Hammond, *Chem. Mater.* **2014,** *26*,

2579; c) S. M. Choi, I. S. Kang, Y. K. Sun, J. H. Song, S. M. Chung and D. W. Kim, *J. Power Sources* **2013,** *244*, 363.

[8] J. M. Tarascon, M. Armand, *Nature* **2001,** *414*, 359.

[9] a) W. H. Meyer, *Adv. Mater.* **1998,** *10*, 439; b) L. Z. Long, S. J. Wang, M. Xiao and Y. Z. Meng, *J. Mater. Chem. A* **2016,** *4*, 10038; c) J. Shim, D. G. Kim, H. J. Kim, J. H. Lee and J. C. Lee, *ACS Appl. Mater. Interfaces* **2015,** *7*, 7690; d) J. Shim, D. G. Kim, H. J. Kim, J. H. Lee, J. H. Baik and J. C. Lee, *J. Mater. Chem. A* **2014,** *2*, 13873; e) D. G. Kim, H. S. Sohn, S. K. Kim, A. Lee and J. C. Lee, *J. Polym. Sci., Part A: Polym. Chem.*, **2012,** *50*, 3618; f) S. K. Kim, D. G. Kim, A. Lee, H. S. Sohn, J. J. Wie, N. A. Nguyen, M. E. Mackay and J. C. Lee, *Macromolecules* **2012,** *45*, 9347; g) D. G. Kim, J. M. Shim, J. H. Lee, S. J. Kwon, J. H. Baik and J. C. Lee, *Polymer* **2013,** *54*, 5812; h) S. J. Kwon, D. G. Kim, J. Shim, J. H. Lee, J. H. Baik and J. C. Lee, *Polymer* **2014,** *55*, 2799; i) J. Shim, D.-G. Kim, J. H. Lee, J. H. Baik and J.-C. Lee, *Polym. Chem.* **2014,** *5*, 3432.

[10] Z. G. Xue, D. He and X. L. Xie, *J. Mater. Chem. A* **2015,** *3*, 19218.

[11] a) J. Shim, K. Y. Bae, H. J. Kim, J. H. Lee, D. G. Kim, W. Y. Yoon and J. C. Lee, *Chemsuschem* **2015,** *8*, 4133; b) K. H. Choi, S. J.

Cho, S. H. Kim, Y. H. Kwon, J. Y. Kim and S. Y. Lee, *Adv. Funct. Mater.* **2014,** *24*, 44; c) Y. Kang, W. Lee, D. Hack Suh and C. Lee, *J. Power Sources* **2003,** *119*, 448; d) Y. K. Kang, J. Lee, J. I. Lee and C. Lee, *J. Power Sources* **2007,** *165*, 92.

[12] a) M. S. Park and W. Y. Yoon, *J. Power Sources* **2003,** *114*, 237; b) S. W. Kim, Y. J. Ahn and W. Y. Yoon, *Met. Mater.* **2000,** *6*, 345.

[13] a) U. H. Choi, S. W. Liang, M. V. O'Reilly, K. I. Winey, J. Runt and R. H. Colby, *Macromolecules* **2014,** *47*, 3145; b) Y. Kang, W. Lee, D. Hack Suh and C. Lee, *J. Power Sources* **2003,** *119*, 448.

[14] P. J. Evans, R. C. T. Slade, J. R. Varcoe and K. E. Young, *J. Mater. Chem.* **1999,** *9*, 3015.

[15] J. S. Kim, S. Yang and B. S. Bae, *Chem. Mater.* **2010,** *22*, 3549.

[16] J. Gershenzon and N. Dudareva, *Nat. Chem. Biol.* **2007,** *3*, 408.

[17] a) Y. J. Zuo, J. F. Cao and S. Y. Feng, *Adv. Funct. Mater.* **2015,** *25*, 2754; b) M. Claudino, J. M. Mathevet, M. Jonsson and M. Johansson, *Polym. Chem.* **2014,** *5*, 3245; c) M. Firdaus, L. M. de Espinosa and M. A. R. Meier, *Macromolecules* **2011,** *44*, 7253; d) K. Hearon, L. D. Nash, J. N. Rodriguez, A. T. Lonnecker, J. E. Raymond, T. S. Wilson, K. L. Wooley and D. J. Maitland, *Adv. Mater.* **2014,** *26*, 1552.

[18] a) C. E. Hoyle and C. N. Bowman, *Angew. Chem.Int. Ed.* **2010,** *49*, 1540; b) J. J. Yan, J. T. Sun, Y. Z. You, D. C. Wu and C. Y. Hong, *Sci.Rep.* **2013,** *3*, 2841.

[19] G. Z. Yang, S. L. Kristufek, L. A. Link, K. L. Wooley and M. L. Robertson, *Macromolecules* **2015,** *48*, 8418.

[20] Q. Z. Xiao, X. Z. Wang, W. Li, Z. H. Li, T. J. Zhang and H. L. Zhang, *J. Membr. Sci.* **2009,** *334*, 117.

[21] a) D. L. Safranski and K. Gall, *Polymer* **2008,** *49*, 4446; b) L. M. Campos, I. Meinel, R. G. Guino, M. Schierhorn, N. Gupta, G. D. Stucky and C. J. Hawker, *Adv. Mater.* **2008,** *20*, 3728.

[22] D. Zhou, R. L. Liu, Y. B. He, F. Y. Li, M. Liu, B. H. Li, Q. H. Yang, Q. Cai and F. Y. Kang, *Adv. Energy Mater.* **2016,** *6*, 1502214.

[23] R. Khurana, J. L. Schaefer, L. A. Archer and G. W. Coates, *J. Am. Chem. Soc.* **2014,** *136*, 7395.

[24] a) S. O. Tung, S. Ho, M. Yang, R. L. Zhang and N. A. Kotov, *Nat. Commun.* **2015,** *6*, 6152; b) W. Na, A. S. Lee, J. H. Lee, S. S. Hwang, E. Kim, S. M. Hong and C. M. Koo, *ACS Appl. Mater. Interfaces* **2016,** *8*, 12852.

[25] R. R. Miao, J. Yang, Z. X. Xu, J. L. Wang, Y. Nuli and L. M. Sun, *Sci. Rep.* **2016,** *6*, 21771.

[26] B. Gyenes, D. A. Stevens, V. L. Chevrier and J. R. Dahn, *J. Electrochem. Soc.* **2015,** *162*, A278.

[27] a) B. Sun, I. Y. Liao, S. Tan, T. Bowden and D. Brandell, *J. Power Sources* **2013,** *238*, 435; b) Y. G. Zhang, Y. Zhao, D. Gosselink and P. Chen, *Ionics*, **2015,** *21*, 381; c) S. Das, P. Ngene, P. Norby, T. Vegge, P. E. de Jongh and D. Blanchard, *J. Electrochem. Soc.* **2016,** *163*, A2029.

Table 3.1. Summary on compositions, glass transition temperatures (T_gs), and ionic conductivities of L-BPTPs and G-BPTPs.

SPEs / Properties	L-BPTPs			G-BPTPs		
	L-BPTP25	L-BPTP50	L-BPTP75	G-BPTP25	G-BPTP50	G-BPTP75
PEO (mol%)	25	50	75	25	50	75
Terpene (mol%)	75	50	25	75	50	25
T_g (^{o}C)	-39.6	-45.2	-55.6	-43.3	-56.0	-60.9
Ionic conductivity at 30 ^{o}C (S/cm)	2.6×10^{-6}	1.3×10^{-5}	4.2×10^{-5}	5.2×10^{-6}	2.3×10^{-5}	8.6×10^{-5}

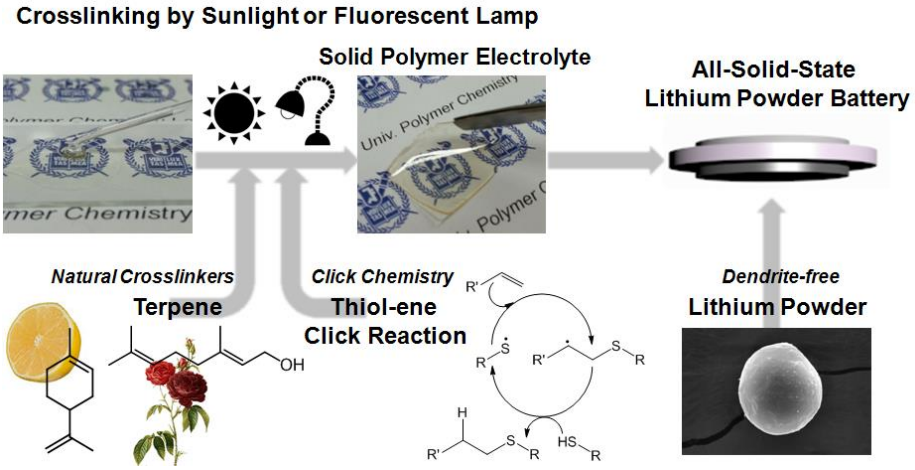

Figure 3.1. Development of all-solid-state lithium powder battery containing solid polymer electrolyte (SPE) containing natural terpene crosslinkers prepared by thiol-ene click reaction.

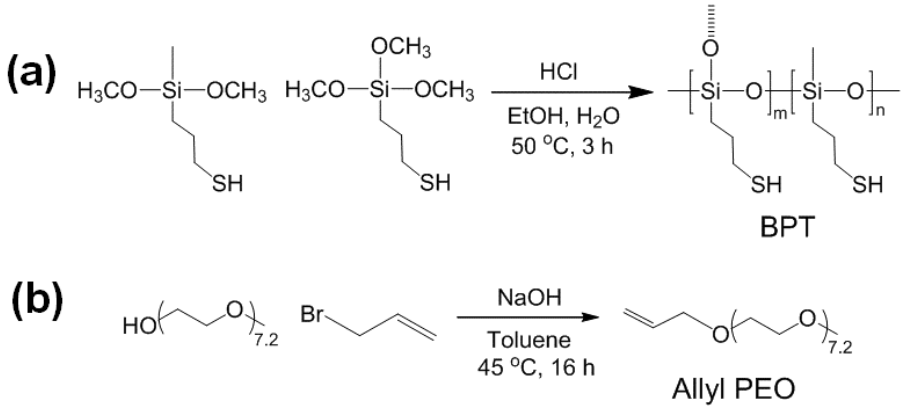

Figure 3.2. Synthesis of (a) branched polysiloxane having thiol group (BPT) and (b) allyl poly(ethylene oxide) (allyl PEO).

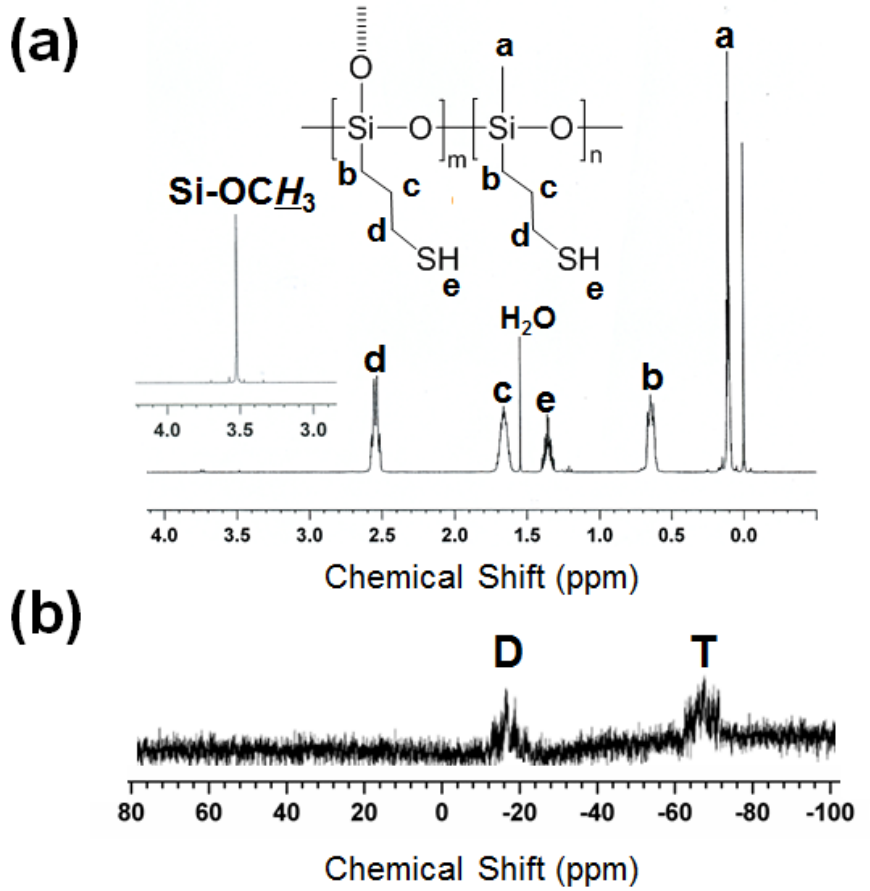

Figure 3.3. (a) ^{1}H NMR spectrum and (b) ^{29}Si NMR spectrum of BPT.

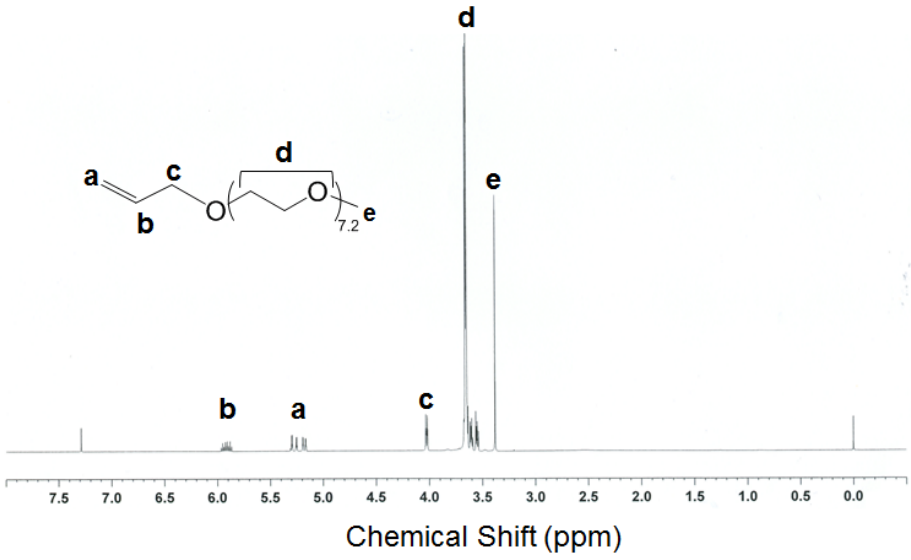

Figure 3.4. ^{1}H NMR spectrum of allyl PEO.

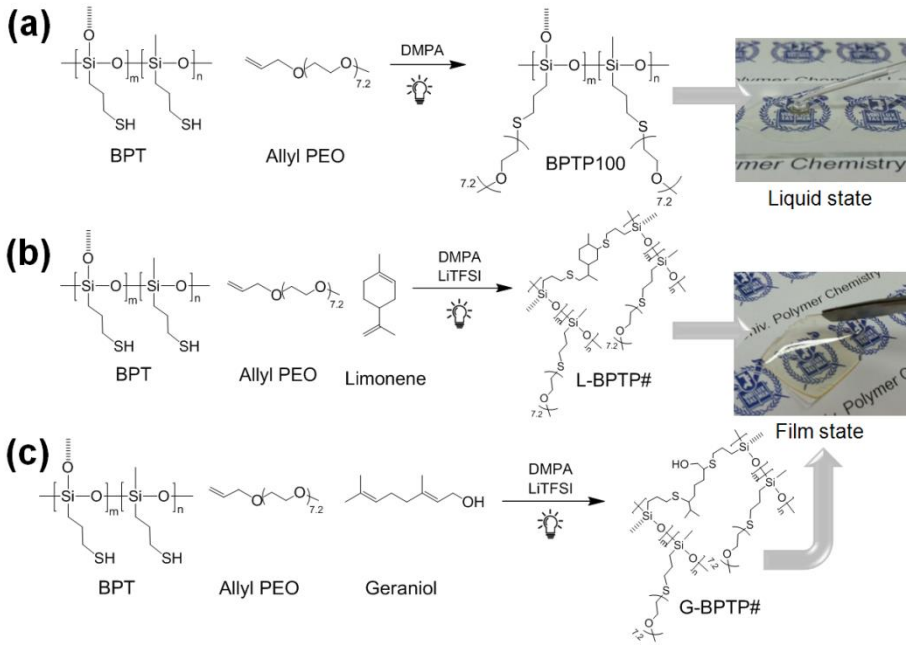

Figure 3.5. Preparation of (a) BPTP100, (b) L-BPTPs, and (c) G-BPTPs where # indicates mol% of allyl PEO.

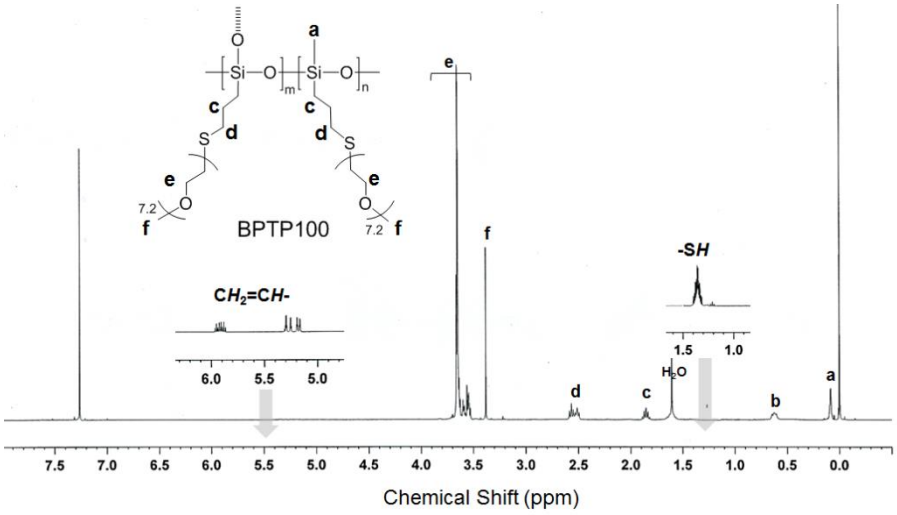

Figure 3.6. ^{1}H NMR spectrum of BPTP100.

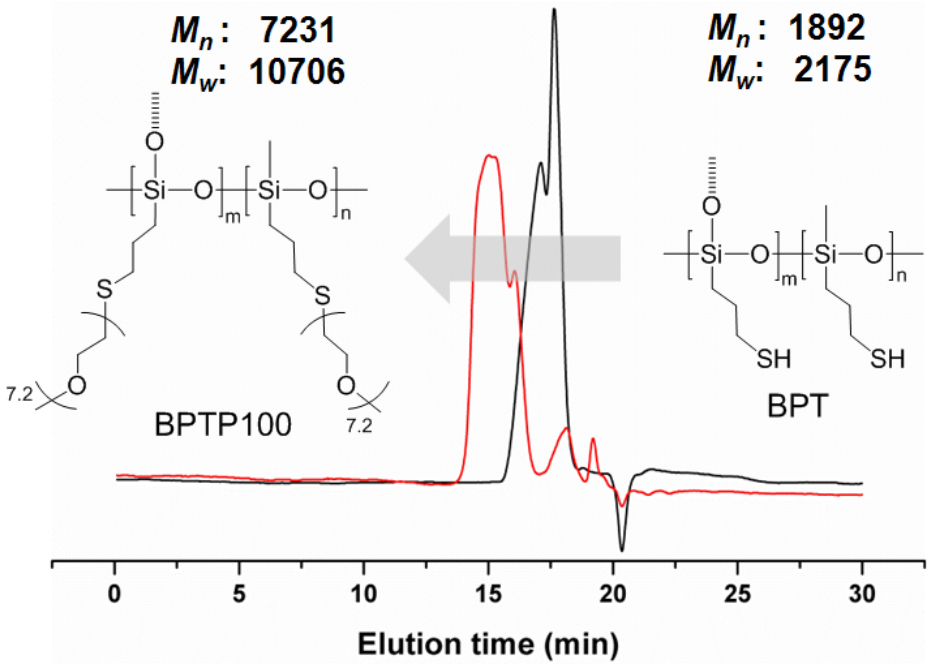

Figure 3.7. GPC profile of BPT and BPTP100.

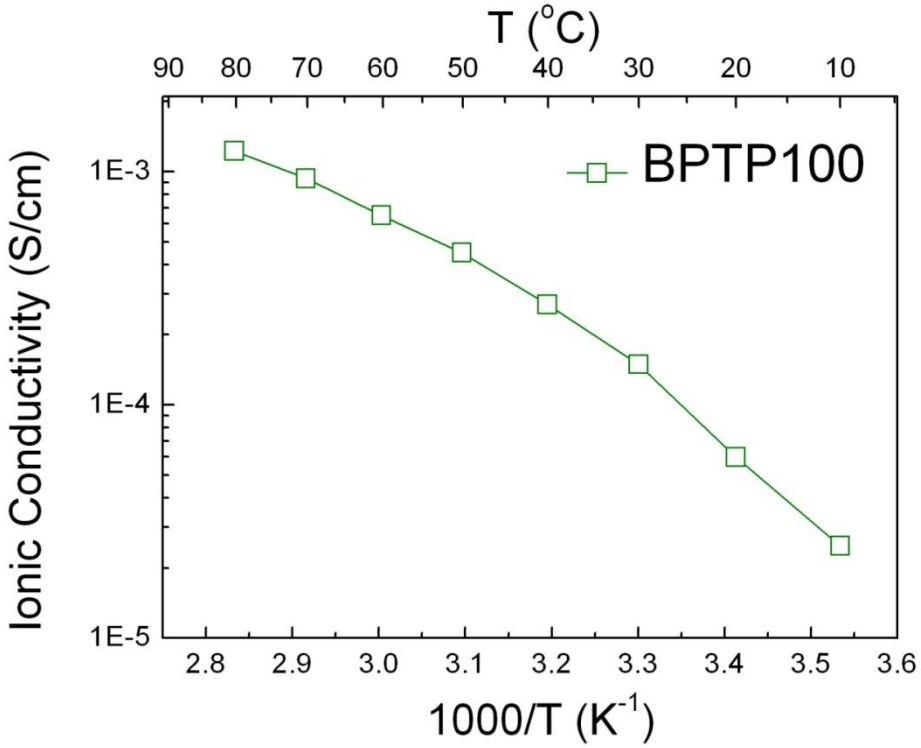

Figure 3.8. Temperature dependene of ionic conductivity of BPTP100 containing LiTFSI ([Li]/[EO]=0.07).

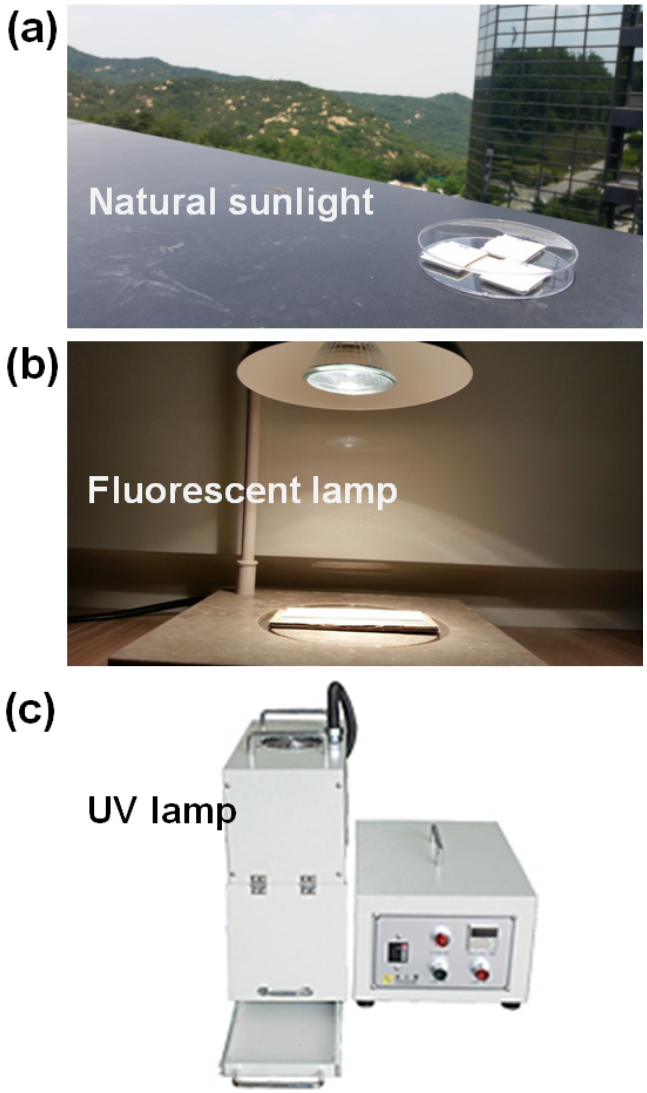

Figure 3.9. Photographs of irradiation with (a) natural sunlight, (b) fluorescent lamp, and (c) UV lamp.

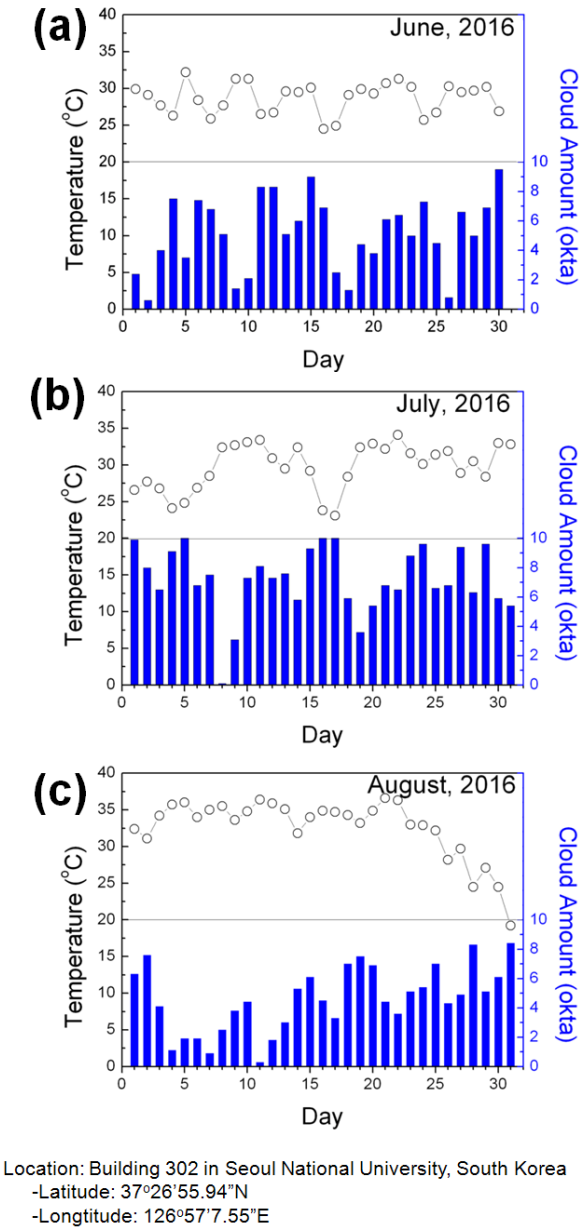

Figure 3.10. Temperature and cloud amount in June to August, 2016, at building 302 in Seoul National University.

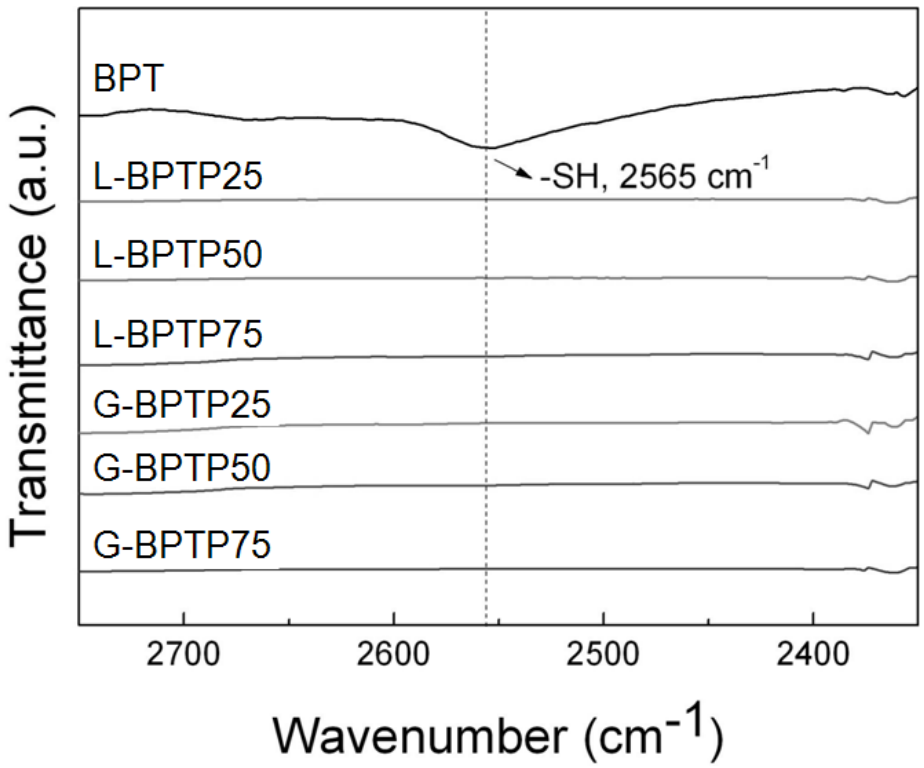

Figure 3.11. FT-IR spectra of BPT, L-BPTPs, and G-BPTPs, where the number in the abbreviation indicates mol% of PEO groups.

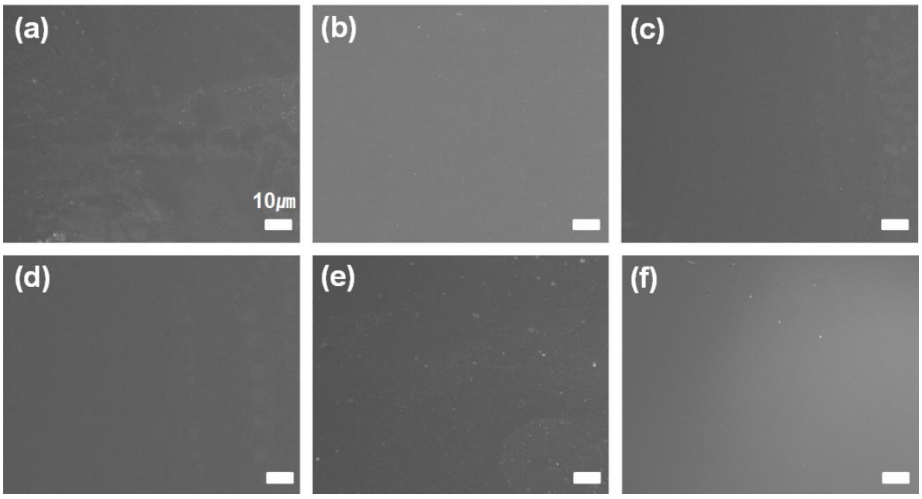

Figure 3.12. Surface SEM images of (a) L-BPTP25, (b) L-BPTP50, (c) L-BPTP75, (d) G-BPTP25, (e) G-BPTP50, and (f) G-BPTP75 (scale bar: 10 μm).

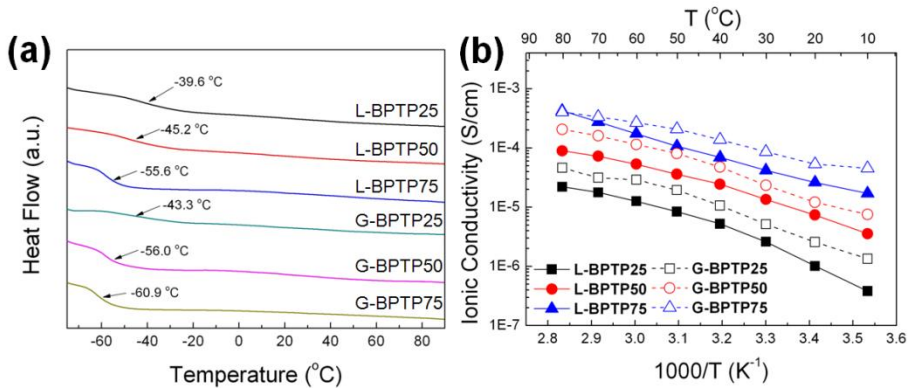

Figure 3.13. (a) DSC thermograms of L-BPTPs and G-BPTPs and (b) temperature dependence of ionic conductivities of L-BPTPs and G-BPTPs, where each electrolyte contains same LiTFSI concentration ([Li]/[EO]=0.07).

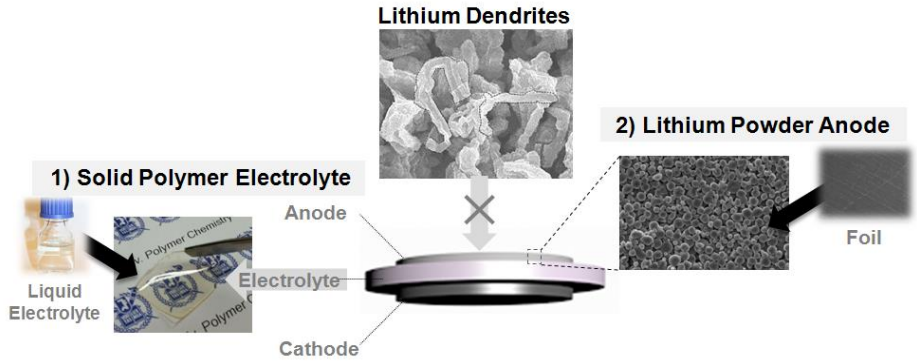

Figure 3.14. Schematic diagram of the all-solid-state lithium powder battery with solid polymer electrolyte and lithium powder anode.

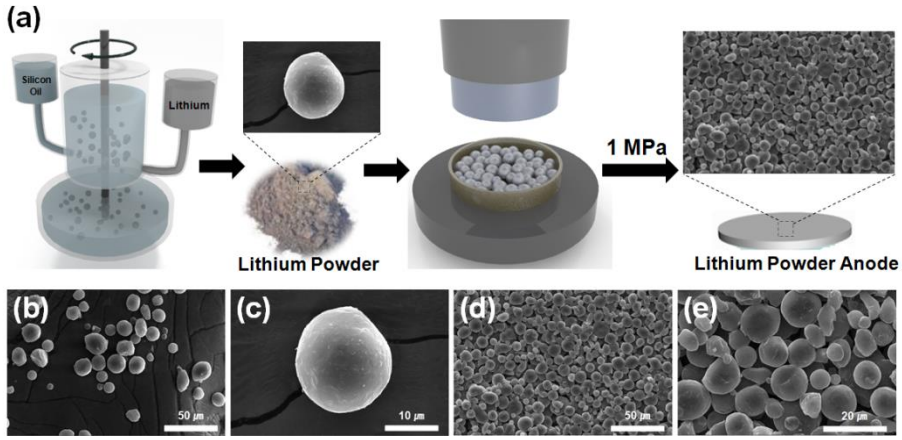

Figure 3.15. (a) Schematic illustration of preparation of lithium powder anode by droplet emulsion technique (DET). SEM images of (b, c) lithium powder (b: ×1000, c: ×5000) and (d, e) surface of lithium powder anode (d: ×1000, e: ×3000).

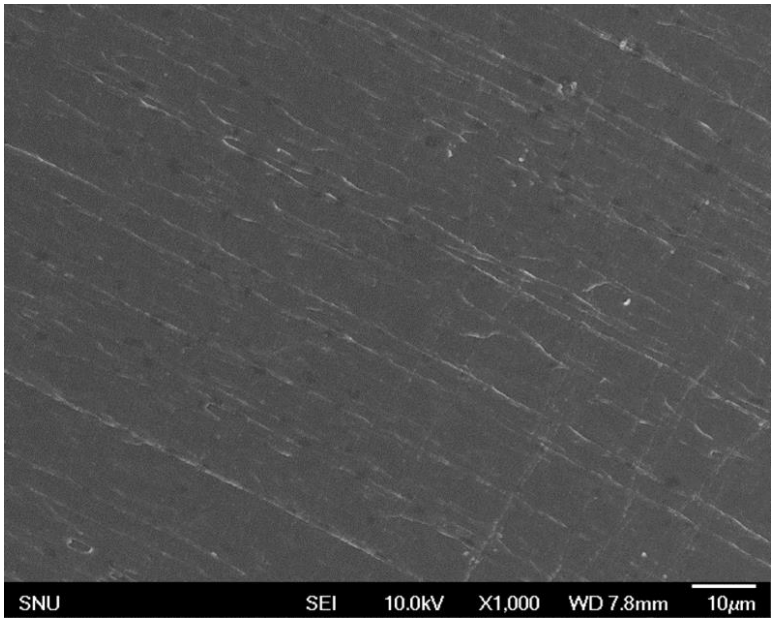

Figure 3.16. Surface SEM image of lithium foil anode.

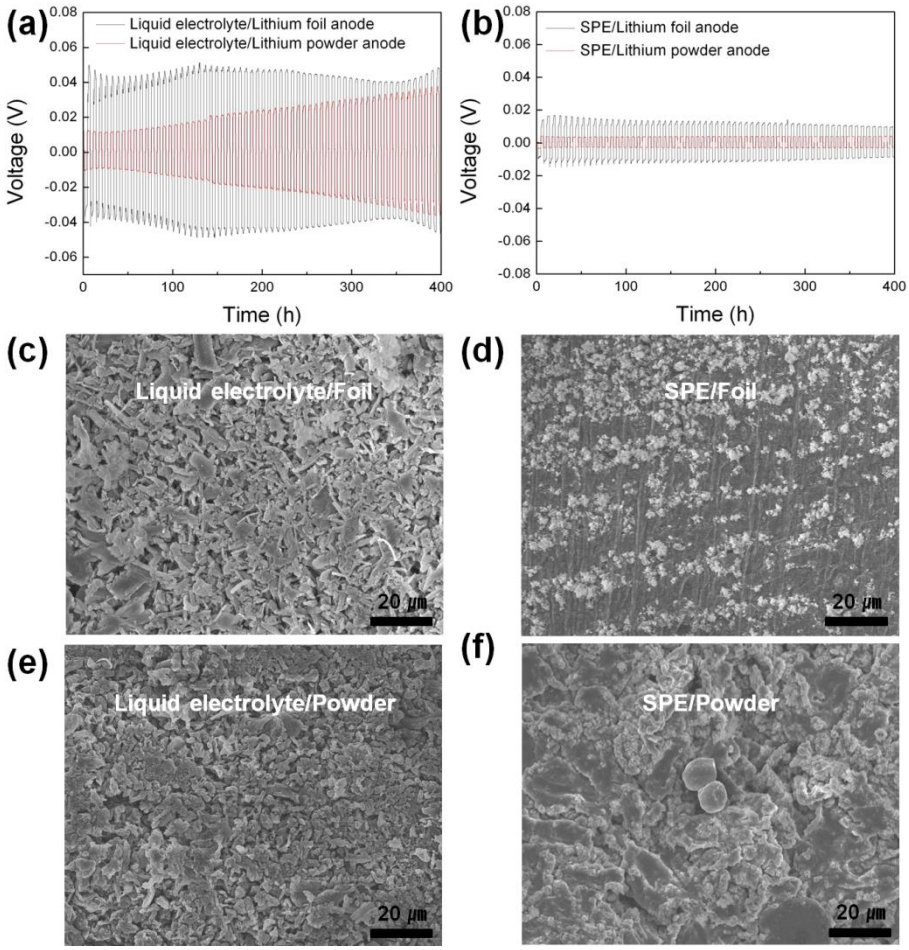

Figure 3.17. Galvanostatic cycling curves of symmetric cells prepared using lithium foil and powder anode with (a) liquid electrolyte and (b) SPE (G-BPTP75) at a current density of 0.2 mA/cm^2 at 60 ^{o}C. Surface SEM images of lithium anode in the cell prepared with (c) liquid electrolyte/lithium foil anode, (d) SPE/lithium foil anode, (e) liquid electrolyte/lithium powder anode, and (f) SPE/lithium powder anode after 400 h of cycling.

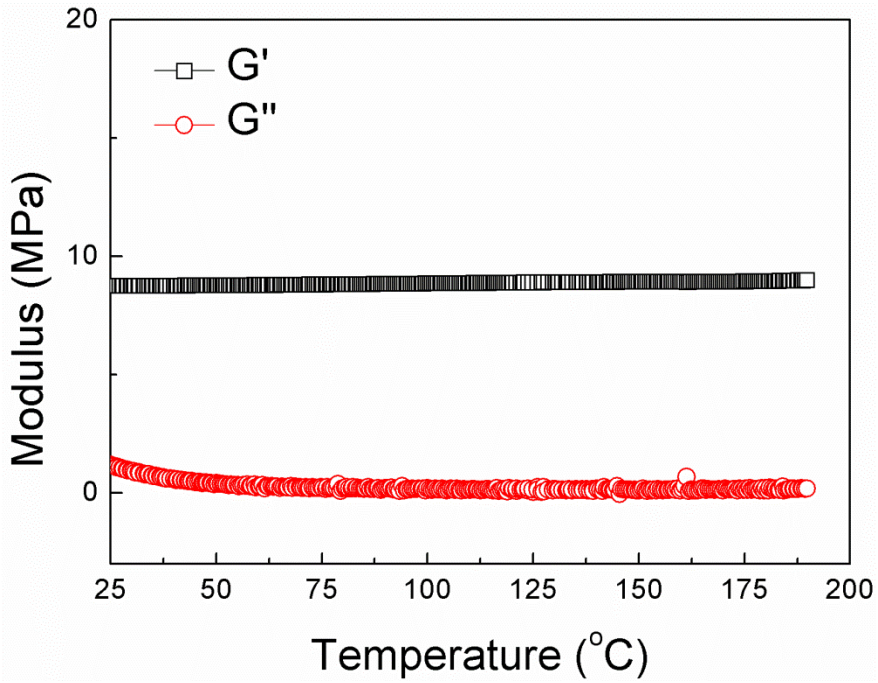

Figure 3.18. Temperature-resolved rheological behaviors of G-BPTP75 in the linear viscoelastic region with 1 Hz of frequency at 1 °C/min ramp.

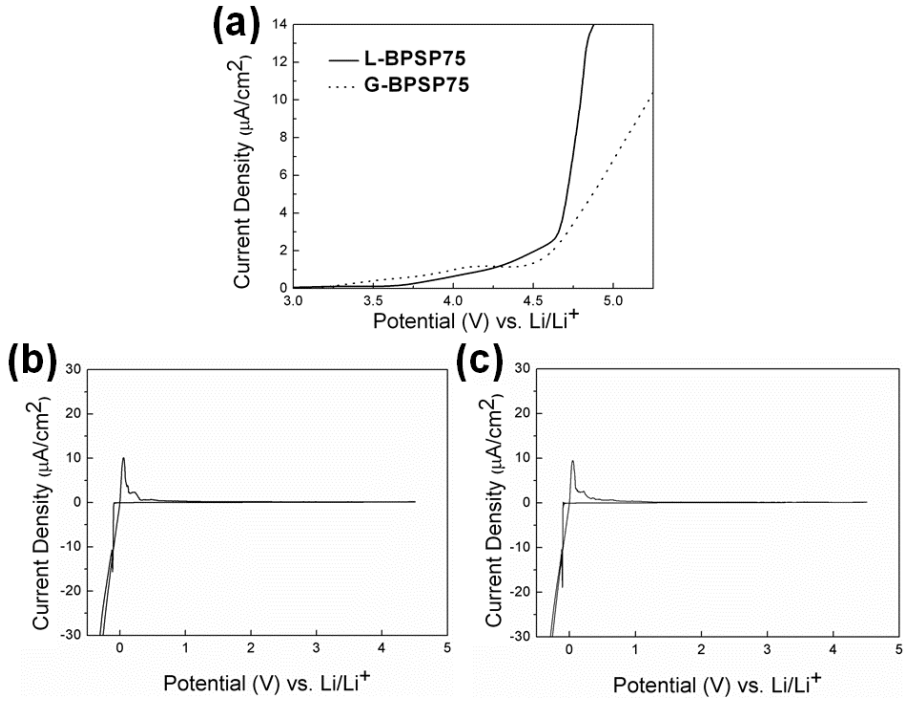

Figure 3.19. (a) Linear sweep voltammogram of L-BPTP75/G-BPTP75 and cyclic voltammogram of (b) L-BPTP75 and (c) G-BPTP75 at 60 ^{o}C with a scan rate of 1 mV/s.

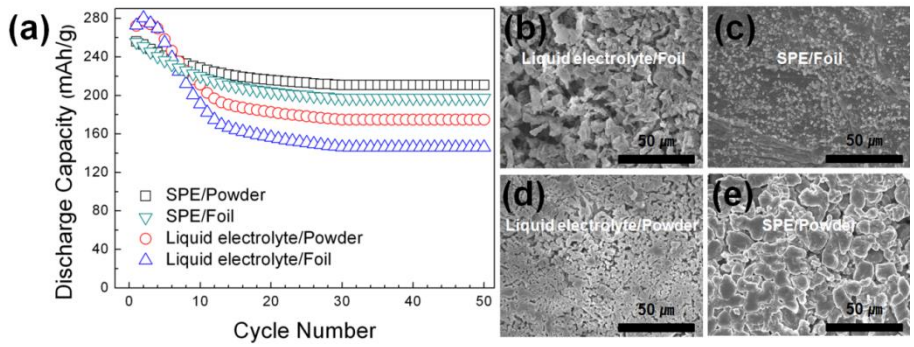

Figure 3.20. (a) Discharge capacity profiles of lithium (foil or powder)/electrolyte (liquid electrolyte or SPE)/LiV_3O_8 cells cycled at 60 ^oC with a scan rate of 0.1 C. Surface SEM images of lithium anode after 50 cycles from the cell prepared with (b) liquid electrolyte/lithium foil anode (△), (c) SPE/lithium foil anode (▽), (d) liquid electrolyte/lithium powder anode (○), and (e) SPE/lithium powder anode (□), where SPE indicates G-BPTP75.

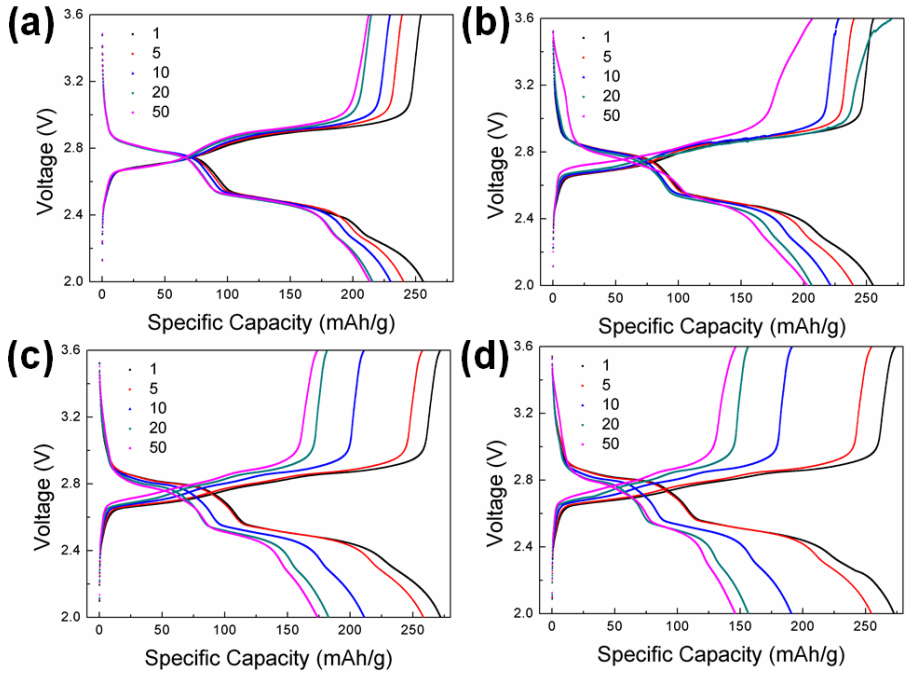

Figure 3.21. Voltage-capacity curves of cells containing (a) SPE/Powder, (b) SPE/Foil, (c) Liquid electrolyte/Powder, and (d) Liquid electrolyte/Foil cycled at 60 ^{o}C with a scan rate of 0.1 C, where each cell has LiV_3O_8 as a cathode.

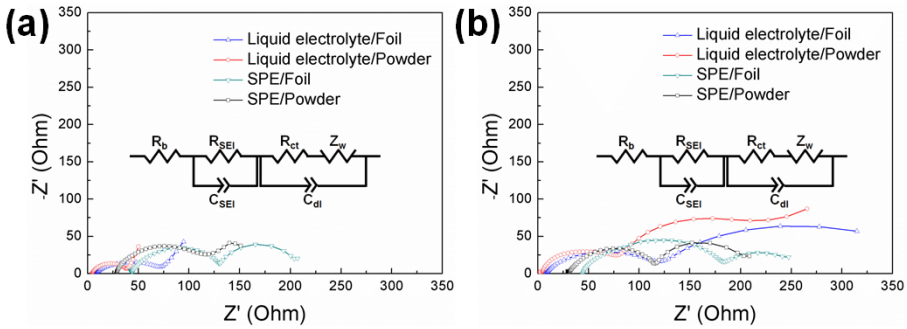

Figure 3.22. Electrochemical impedance spectra of the cell prepared with SPE/Powder, SPE/Foil, Liquid electrolyte/Powder, and Liquid electrolyte/Foil (a) before and (b) after cycling.

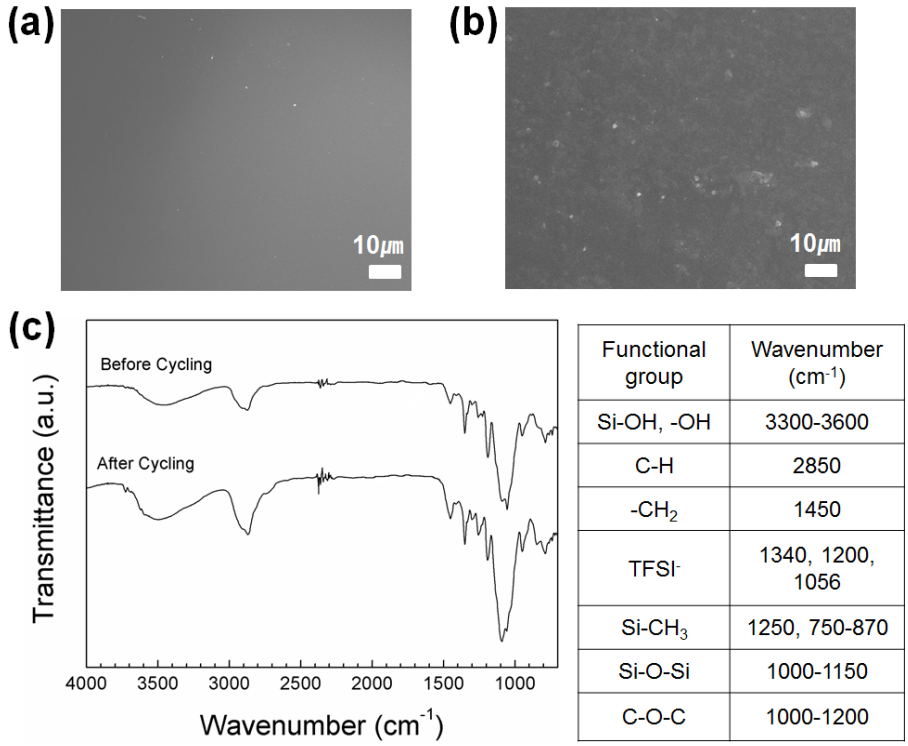

Functional group	Wavenumber (cm^{-1})
Si-OH, -OH	3300-3600
C-H	2850
$-CH_2$	1450
$TFSI^-$	1340, 1200, 1056
$Si-CH_3$	1250, 750-870
Si-O-Si	1000-1150
C-O-C	1000-1200

Figure 3.23. Surface SEM images of G-BPTP75 (a) before and (b) after cycling (scale bar: 10 μm) and (c) FT-IR spectra of G-BPTP75 before and after cycling.

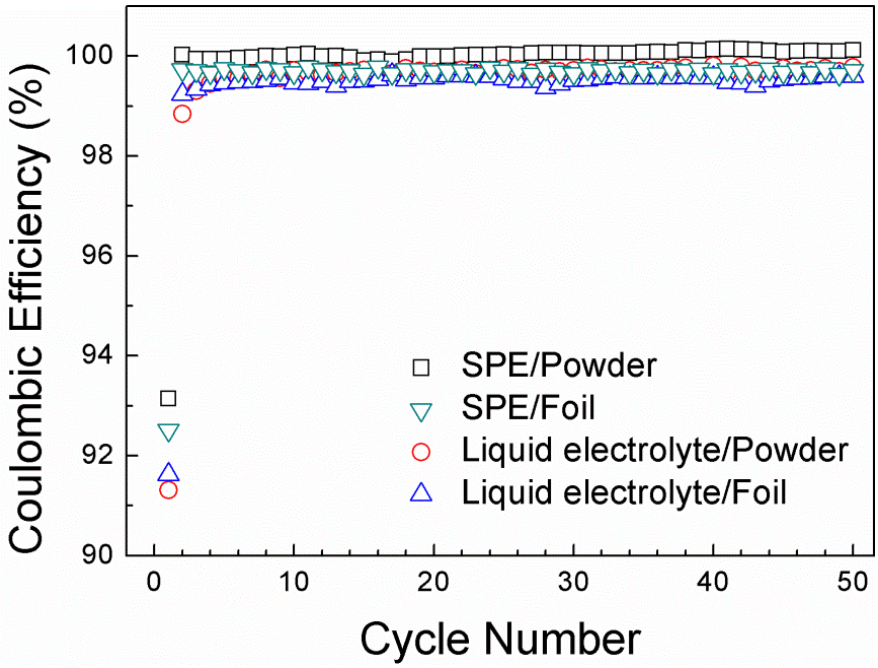

Figure 3.24. Coulombic efficiency of lithium (foil or powder)/electrolyte (liquid electrolyte or SPE)/LiV_3O_8 cells cycled at 60 ^oC with a scan rate of 0.1 C.

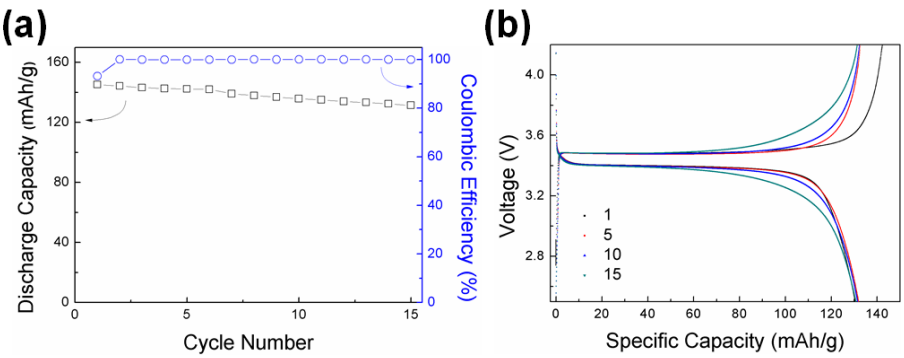

Figure 3.25. (a) Discharge capacity profiles and (b) voltage-capacity curves of of lithium powder/G-BPTP75/ $LiFePO_4$ cycled at 60 ^{o}C with a scan rate of 0.1 C.

Chapter 4

Polymer Composite Electrolytes Having Core-Shell Silica Fillers with Anion-Trapping Boron Moiety in the Shell Layer for All-Solid-State Lithium-Ion Batteries

4.1. Introduction

Solid polymer electrolytes (SPEs) for all-solid-state lithium-ion battery applications have been extensively studied to satisfy several requirements for next generation of energy storage and conversion devices especially related with safety issues.[1-7] Since currently used liquid electrolyte systems based on organic carbonate solvents have serious safety problems caused by leakage of liquids, their high temperature applications have been limited. On the other hand, SPEs having dimensional/thermal stability at high temperature can widen the applications of lithium-ion batteries for electrical vehicles and electricity storage systems.[2] Furthermore, lithium metal anode possessing large capacity (3,860 mAh g^{-1}) can be more easily applied to the lithium battery systems using SPEs because SPE layers on the anode surface can prevent exposure of explosive lithium metal and at the same time suppress growth of lithium dendrite.[8-10] However, intrinsic low ionic conductivity originating from slow segmental motion of the solid polymer chains at ambient temperature still has to be increased for practical applications.

Among various strategies to develop the SPEs exhibiting high ionic

conductivity combined with excellent mechanical stability, polymer composite electrolyte systems containing fillers such as carbon or ceramic materials have been suggested.[6, 11-14] In particular, silica particles have been known as effective filler materials that can enhance both ionic conductivity and mechanical stability of the polymer electrolytes.[13-21] Furthermore, silica particle can suppress formation of irregular passivation layers at the lithium anode surface.[22, 23] Since boron has empty *p*-orbital that can interact with basic anion of lithium salt, chemical additives having boron moiety have been known to increase lithium transference number in the electrolyte systems; lithium transference number is defined as relative amount of the lithium ion transport compared to that of the counter anion.[24-26] Therefore, a series of researches have been performed to prepare polymers or low molecular weight compounds containing boron moieties as electrolytes or additive materials to improve electrochemical properties and cycle performance of the lithium-ion batteries.[21, 24, 25, 27-33]

Recently, organic/inorganic hybrid branched-graft copolymers (BCP) comprising poly(ethylene glycol) and polyhedral oligomeric silsesquioxane (POSS) moieties prepared in our group was reported as SPE for all-solid-state lithium-ion batteries (Figure 4.1).[7] BCP was

found to be promising polymer materials for the SPEs at high-temperature due to its good dimensional/thermal stability at elevated temperature. Still, ionic conductivity (1.1×10^{-5} S/cm at 30 ^{o}C) and cycle performance of the BCP need to be improved. As a continuous effort to improve the performance of all-solid-state lithium-ion batteries, herein, we firstly prepared BCP-based polymer composite electrolyte systems exhibiting high ionic conductivity and mechanical stability using core-shell silica particles having boron moiety in the shell layer as filler materials. The core-shell silica particles were found to improve mechanical stability, ionic conductivity, and transference number of the BCP matrix due to rigid silica core structures and boron moiety in the shell layers. Furthermore, excellent cycle performance was observed from the all solid-state lithium-ion battery system prepared using this polymer composite electrolyte.

4.2. Experimental

4.2.1. Materials

2,2'-Azobis(isobutyronitrile) (AIBN, Junsei) was recrystallized from

ethanol prior to use. Poly(ethylene glycol) methyl ether methacrylate (PEGMA, average M_n = 475 g mol^{-1}) and ethylene glycol dimethylacrylate (EGDMA) was purchased from Aldrich and passed through an alumina column prior to polymerization. MethacrylisobutylPOSS® (3-(3,5,7,9,11,13,15-heptaisobutyl-pentacyclo[9.5.1.$1^{3,9}$.$1^{5,15}$.$1^{7,13}$]octasiloxane-1-yl)propyl methacrylate, MA-POSS) was purchased from Hybrid Plastics (product no. MA0702) and used as received. Tetrahydrofuran (THF) was freshly distilled from sodium/benzophenone under a nitrogen atmosphere. Lithium perchlorate ($LiClO_4$, >98%, Aldrich) was dried under high vacuum at 130 ^oC for 24 h and subsequently placed in an argon filled glove box. Poly(ethylene glycol) methacrylate (average M_n = 500 g mol^{-1}), 2,5-dimethylhexane-2,5-diol, trimethyl borate, tetraethyl orthosilicate (TEOS), chloro(dimethyl)vinylsilane, and 30 % of ammonium hydroxide solution were purchased from Aldrich. The chain transfer agent (CTA), 2-cyanoprop-2-yl-1-dithionaphthalate (CPDN), was synthesized as previously described.[34] All the other reagents and solvents were obtained from reliable commercial sources and used as received.

4.2.2. Synthesis of organic/inorganic hybrid branched-graft copolymer (BCP)

BCP comprising 21 mol % of MA-POSS and 79 mol % of PEGMA moiety was synthesized *via* reversible addition-fragmentation transfer (RAFT) polymerization as follows. PEGMA (5.0 g, 10.5 mmol), MA-POSS (2.80 g, 2.78 mmol), EGDMA (0.042 g, 0.021 mmol), CPDN (0.029 g, 0.10 mmol), and AIBN (0.006 g, 0.034 mmol) were dissolved in 12 mL of distilled THF and the solution was degassed by three repetitive freeze-pump-thaw processes to remove oxygen. Polymerization was conducted in an oil bath thermostated at 85 ^{o}C for 21 h under N_2 atmosphere. After the polymerization, unreacted monomers were removed by precipitation in *n*-hexane three times. After dried under vacuum at room temperature for 3 days, rubbery solid product was obtained with 65 % of yield. ^{1}H NMR [300 MHz, $CDCl_3$, δ. (ppm), TMS ref] of BCP: 4.08 (C*H*$_2$-O-C(O)), 3.48-3.85 (C*H*$_2$-C*H*$_2$-O), 3.38 (C*H*$_3$-O), 1.85 (isobutyl, C*H*), 1.53-2.05 (methacrylate backbone, C*H*$_2$-C(CH$_3$)(C=O)), 0.95 (isobutyl, C*H*$_3$), 0.78-1.11 (methacrylate backbone, CH$_2$-C(C*H*$_3$)(C=O)), 0.6 (isobutyl, C*H*$_2$).

4.2.3. Synthesis of PEGMA containing boronic ester group (B-PEGMA)

2,5-Dimethylhexane-2,5-diol (5.0 g, 0.034 mol) and trimethyl borate (3.8 mL, 0.034 mol) were dissolved in 50 mL of anhydrous acetonitrile, and the solution was stirred at 65 ^{o}C for 1 h under N_2 purging condition. Poly (ethylene glycol) methacrylate (M_n = 500 g mol^{-1}) (12 g, 0.034 mol) was subsequently added to the solution and stirred at 65 ^{o}C for another 3 h. After the reaction, residual solvent was removed under reduced pressure by evaporation. The crude product was dissolved in toluene and cooled to room temperature. Insoluble part was removed by filtration and toluene was removed under reduced pressure at 60 ^{o}C. After dried under vacuum at room temperature for 24 h, PEGMA containing boronic ester group was obtained with 97 % of yield. The obtained product was stored in a vacuum oven not to contact with moisture that can hydrolyze the product. PEGMA containing boronic ester group is abbreviated as B-PEGMA. ^{1}H NMR [300 MHz, $CDCl_3$, δ (ppm), TMS ref] of B-PEGMA: 5.57-6.16 (CH_2-C(CH_3)(C=O), 2H), 3.48-3.85 (CH_2-CH_2-O,

40H), 1.97 (CH_2-C(C*H*$_3$)(C=O), 3H), 1.56 (methylene, C(CH_3)$_2$-C*H*$_2$-C*H*$_2$-C(CH_3)$_2$, 4H), 1.24 (methyl, C(C*H*$_3$)$_2$-CH_2-CH_2-C(C*H*$_3$)$_2$, 12H). Elemental analysis: Found (%): C, 56.2144; H, 8.9431; O, 29.0174. Calcd. for $C_{30}H_{57}O_{13}B$: C, 56.6929; H, 8.9763; O, 32.7559.

4.2.4. Preparation of silica particle having vinyl group (Vinyl Si)

Silica particle having average diameter of about 200 nm was prepared by Stö ber method. NH_4OH (1.8 g, 0.05 mol) was dissolved in a mixed solvent (water-ethanol mixture (5:1 v/v)) and resultant solution was added to a 500 mL one-neck round bottomed flask equipped with a magnetic stirring bar. TEOS (6.3 mL, 0.028 mol) was added to the solution and then hydrolysis and condensation reactions were conducted in an oil bath thermostated at 25 ^oC for 1 h under N_2 atmosphere. After the flask was removed from the oil bath, unreacted TEOS was thoroughly removed by several centrifugal washing with isopropanol. Obtained silica particle was dried under high vacuum at 60 ^oC for 24 h. After drying, 2 g of silica particle was further reacted with 0.2 mL of chloro(dimethyl)vinylsilane in 100 mL of mixed

solvent (water-ethanol mixture (5:1 v/v)) at 50 ^{o}C for 24 h. Obtained silica particle having vinyl group was dried under high vacuum at 60 ^{o}C for 24 h. For the convenience, silica particle having vinyl group is abbreviated as vinyl Si.

4.2.5. Preparation of core-shell silica particles (Si-P and Si-B)

0.2 g of vinyl Si was grinded and dispersed in 10 mL of distilled THF followed by ultrasonication for 30 min. 0.8 g of PEGMA and 0.04 g of AIBN were dissolved in 5 mL of distilled THF and transferred to the silica dispersed solution. The resultant solution was transferred to a 50 mL Schlenk flask equipped with a magnetic stirring bar and a condenser. The solution was degassed by three consecutive freeze-pump-thaw cycles to remove oxygen and dispersed under sonication for 30 min right before the polymerization, and then it was heated to 70 ^{o}C for 24 h under N_2 atmosphere to convert the monomer, PEGMA, into the polymer, P(PEGMA). The unreacted monomers and free polymers unattached to the silica surface were removed by washing with THF and resultant core-shell silica particle was collected by centrifuge process. Core-shell silica particle having P(PEGMA) in

the shell layer was obtained in 53 % of yield after drying under high vacuum at 60 ^{o}C for 24 h. Core-shell silica particle having P(B-PEGMA) in the shell layer was also obtained in 61 % of yield using same process used for the core-shell silica particle having P(PEGMA) in the shell layer except the monomer. The core-shell silica particles with P(PEGMA) in the shell layer and with P(B-PEGMA) in the shell layer are abbreviated as Si-P and Si-B, respectively.

4.2.6. Detachment of P(PEGMA) and P(B-PEGMA) in the shell layer of Si-P and Si-B

100 mg of core-shell silica particle was dispersed in 30 mL of THF under sonication and 5 mL of hydrofluoric acid (HF) was added to the dispersed solution. Since HF is a highly corrosive chemical known as a contact poison, it was handled very carefully inside of a fume hood and stored in Teflon or polyethylene container because it even reacts with glass. The solution was stirred at room temperature for 24 h to detach the shell layer from the silica core. The resultant solution was precipitated in *n*-hexane with several times until the trace of HF was removed. Residual solvent was evaporated at reduced pressure and

further dried under high vacuum at 60 ^{o}C for 24 h.

4.2.7. Preparation of polymer composite electrolytes (BCP-vinyl Si, BCP-Si-P, and BCP-Si-B)

Solid-state polymer composite electrolytes containing BCP (M_w = 16,200), $LiClO_4$, and core-shell silica fillers in various compositions were prepared by a solution casting technique. Doping levels of $LiClO_4$ are defined as a ratio of the number of lithium cations (Li^+) to that of ethylene oxide (EO) repeating unit ([Li]/[EO] = 0.07) in the polymers. 0.1 g of polymer and given amounts of $LiClO_4$ were dissolved in 0.5 mL of distilled THF and homogeneous solutions were obtained. Different amount of filler was added to the solution and stirred at room temperature for 1 day and then additionally dispersed under sonication for 30 min right before casting process. After that, the solution was cast onto a Teflon plate and dried at room temperature for 24 h. Subsequently, it was further dried under high vacuum at room temperature. Finally, film was peeled off from the Teflon plate and the resultant film was placed in a high vacuum condition for a week at 60 ^{o}C prior to measure ionic conductivities.

Thickness of the films measured by a micrometer (Mitutoyo, 293-330 IP 65 water resistant) was in a range of 200 - 230 μm. For the sake of convenience, polymer composite electrolytes having vinyl Si, Si-P, and Si-B are abbreviated as BCP-vinyl Si, BCP-Si-P, and BCP-Si-B, respectively, and the numbers after the abbreviations represent content of the fillers. For example, BCP-Si-B 10, BCP-Si-B 20, and BCP-Si-B 30 represent that they contain 10, 20, and 30 wt% of Si-B, respectively.

4.2.8. Cell fabrication and electrochemical characterization

Electrochemical stability of the polymer composite electrolytes was evaluated using linear sweep voltammetry (LSV). Cell was assembled by sandwiching electrolyte between stainless steel (working electrode) and lithium metal (reference electrode) in 2032 coin cell. The cell was swept in a potential range from 3 V to 7 V (versus Li/Li^+) at a scan rate of 1 mV/s at 60 ^oC. Charge/discharge test of all-solid-state lithium-ion battery was performed at cutoff voltages of 2.0 ~ 3.8 V versus Li/Li^+ at 60 ^oC with a current density of 0.1 C, where 1.0 C rate corresponds to a current density of 294 mAg^{-1}. V_2O_5 (70 wt%) was used as cathode active material and dispersed in *N*-methyl-2-

pyrrolidone (NMP) with carbon black (20 wt%) and PVDF (10 wt%). The resultant slurry was deposited and cast onto an aluminium current collector using doctor blade. Residual NMP was completely dried under vacuum condition at 120 ^{o}C for 24 h. The obtained cathode sheet, lithium metal, and polymer composite electrolytes were punched into disks and assembled together in 2032 coin cell to form Li/SPE/V_2O_5 cell. All components were assembled in argon filled glove box (H_2O < 0.5 ppm, O_2 < 0.5 ppm).

4.2.9. Measurement of lithium transference number

Lithium transference number (T_{Li+}) was determined using DC polarization/AC impedance combination method. Polymer composite electrolyte was sandwiched between two non-blocking lithium metal disks to form a symmetrical Li/electrolyte/Li coin cell. The cell was polarized by a constant DC voltage of 10 mV and following current values were monitored until steady-state current was observed. Initial and steady-state resistances of the cell were also measured. From this method, T_{Li+} was determined by following equation (1):

$$T_{Li+} = \frac{I_s(V - I_i R_i)}{I_i(V - I_s R_s)} \quad (1)$$

where V indicates a constant DC voltage applied to the cell; R_i and R_s are initial and steady-state resistances, respectively; I_i and R_s are initial and steady-state currents, respectively.

4.2.10. Characterization

^{1}H and ^{13}C NMR spectra were recorded on an AscendTM 400 spectrometer (300 MHz) using $CDCl_3$ (Cambridge Isotope Laboratories) as a solvent at room temperature, with TMS as a reference. Solid-state ^{11}B magic angle spinning (MAS) NMR spectra were recorded on a JeolJNM-LA400 spectrometer (400 MHz) with 7 kHz MAS. Elemental analysis results were obtained with Flash 1112/2000 EA instrument (Thermo Fisher Scientific Inc, USA). Molecular weights (M_n, M_w) and polydispersity index (PDI) were analyzed by gel permeation chromatography (GPC). Relative molecular weight was measured by GPC equipped with a Waters 515 HPLC pump and three columns including PLgel 5.0 μm guard, MIXED-C and MIXED-D from Polymer Laboratories in series with a Viscotek LR125 laser refractometer. The system with a refractive index (RI) detector was calibrated using polystyrene standards from

Polymer Laboratories. The resulting data was analyzed using the Omnisec software. HPLC grade THF (J. T. Baker) was used as the eluent at a flow rate of 1.0 mL min^{-1} at 35 ^{o}C. The thermal transition temperatures of the polymers were examined by differential scanning calorimetry (DSC) using TA Instruments DSC-Q1000 under a nitrogen atmosphere. Samples with a typical mass of 3-7 mg were encapsulated in sealed aluminum pans. The samples were first heated to 150 ^{o}C and then quenched to -80 ^{o}C. This was followed by a second heating scan from -80 ^{o}C to 150 ^{o}C at a heating rate of 10 ^{o}C min^{-1}. The thermal stability of the polymers was investigated by thermogravimetric analysis (TGA) using TA Instruments TGA Q-5000IR under nitrogen atmosphere. The samples were maintained at 130 ^{o}C for 10 min to remove residual water molecules, and then heated to 800 ^{o}C at a heating rate of 10 ^{o}C min^{-1}. FT-IR spectra were recorded in the absorption mode on Nicolet 6700 spectrophotometer with a resolution of 4 cm^{-1} in the vibrational frequency range from 400 to 4000 cm^{-1}. Field-emission scanning electron microscopy (FE-SEM) was performed on a JEOL JSM-6700F with an accelerating voltage of 10 kV. Transmission electron microscopy (TEM) was performed on a LIBRA 120 with an accelerating voltage of 120 kV. The mechanical

properties were measured using a universal testing machine (LS1SC, LLOYD Instruments). The dumbbell specimens were prepared using the ASTM standard D638 (Type V specimens dog-bone shaped samples). The tensile properties of the membrane samples were measured with a gauge length and cross head speed of 15 mm and 5 mm/min, respectively. Five specimens for each sample were tested and average value was calculated. The ionic conductivity of the SPEs was analyzed by complex impedance spectroscopy between 10 to 80 ^{o}C with a Zahner Electrik IM6 apparatus in the frequency range of 0.1 Hz to 1 MHz and an applied voltage of 10 mV. The real part of the impedance at the minimum of imaginary part was used as the resistance to calculate the conductivity of the SPEs. The samples for the measurements were prepared by sandwiching the SPEs between two stainless-steel electrodes into a thickness of 200-300 μm. Each sample was allowed to equilibrate for 30 min at each temperature prior to taking measurements. The ionic conductivity (σ) was calculated from the electrolyte resistance (R) obtained from the impedance spectrum, the electrolyte thickness (d) and the area of the electrode (A) using the equation, $\sigma = (1/R) \times (d/A)$. Electrochemical stability was evaluated by linear sweep voltammetry (LSV) using a

potentiostat (VMP3, Biologics) at 60 ^{o}C at scan rate of 1 mV/s. Charge/discharge test of all-solid-state lithium-ion battery was performed with a WBCS3000 battery cycler (WonATech) at 60 ^{o}C.

4.3. Results and Discussion

4.3.1. Synthesis and characterization of core-shell silica particles

Core-shell silica particle having boron moiety in the shell layer was prepared to be used as filler materials to enhance ionic conductivity, lithium transference number, mechanical stability, and cycle performance of the polymer matrix, BCP, and overall concept of this study is illustrated in Figure 4.2. PEGMA containing boronic ester group (B-PEGMA) was prepared to incorporate boron moiety in the shell layer of the silica particle as presented in Figure 4.3. Bulky 2,5-dimethylhexyl group can increase stability of the boronic ester group from possible hydrolysis by moisture during sample preparation procedures.[35] The formation of B-PEGMA was confirmed using ^{1}H NMR analysis (Figure 4.4(a)). Proton peaks at 1.25 and 1.63 ppm

(signals a and b) represent presence of alkyl and ethylene groups of the boronic ester, verifying successful incorporation of boron moiety into the PEGMA. Signals d at 3.5 – 4.5 ppm are assigned to ethylene oxide units and signals c, e, and f are attributed to methacrylate group of the B-PEGMA. The presence of boron moiety in the B-PEGMA was further confirmed by ^{11}B NMR analysis as shown in Figure 4.4(b). Broad peak at about 20 ppm corresponds to characteristic signal of tri-coordinate boron atoms. ^{13}C NMR and FT-IR analysis were also conducted to confirm the structure of B-PEGMA (Figure 4.5 and Figure 4.6, respectively).

Core-shell silica particles having P(PEGMA) and P(B-PEGMA) in the shell layers abbreviated as Si-P and Si-B, respectively, were prepared as presented in Figure 4.7. Silica particle having reactive vinyl groups on surface (vinyl Si) was synthesized by hydrolysis and condensation reactions of TEOS followed by coupling reaction with chloro(dimethyl)vinylsilane. Uniform spherical shaped vinyl Si having a diameter about 200 nm was obtained and observed by SEM and TEM images as shown in Figure 4.4(a) and 4.4(b), respectively. P(PEGMA) and P(B-PEGMA) can be incorporated on the shell layer of the silica particle by reaction of vinyl Si with PEGMA and B-

PEGMA, respectively, in presence of AIBN. Radical chain polymerization of the monomers, PEGMA and B-PEGMA, can produce free polymer chains (P(PEGMA) and P(B-PEGMA), respectively) unattached to the vinyl Si, while chain transfer of radical to the vinyl groups on vinyl Si can produce shell layers of P(PEGMA) and P(B-PEGMA) chains in Si-P and Si-B, respectively. The free polymers could be easily separated by washing with THF (good solvent for the free polymer) and centrifuge process as described in the experimental section. The formation of the shell layers on Si-P and Si-B could be confirmed with TEM images and their thicknesses were found to be about 20 nm (Figure 4.8(c) and 4.8(d)). Characterization of vinyl Si, Si-P, and Si-B was further conducted using FT-IR analysis as shown in Figure 4.9. Two IR peaks at around 1410 and 1630 cm^{-1} are attributed to vinyl groups on the vinyl Si surface. After radical chain polymerization of the monomers with vinyl Si and AIBN, intensities of vinyl peaks significantly decrease and new absorption peaks at around 1729 cm^{-1} corresponding to carbonyl groups of methacrylate group in the shell layer appear from both Si-P and Si-B, indicating successful incorporation of the polymers (P(PEGMA) and P(B-PEGMA)) from PEGMA and B-PEGMA. Furthermore, presence

of boron moiety in the shell layer on Si-B was additionally confirmed with solid-state ^{11}B MAS NMR analysis; boron signal at about 20 ppm was clearly observed as shown in Figure 4.10, indicating that boronic ester group remains during polymerization and purification procedures without hydrolysis reaction, if any, due to the sterically hindered structure of 2,5-dimethylhexyl group.

The amounts of unattached free polymers and polymers attached on the shell layer could be estimated by TGA analysis for the samples obtained before and after purification process as shown in Figure 4.11. TGA curves of core-shell silica particles (Si-P and Si-B) after removing the unattached free polymers by purification process show gradual weight loss with an onset temperature at around 300 ^{o}C, while that of the vinyl Si shows only small change of weight. Since the residual weight at 800 ^{o}C in TGA curves have been attributed to the silica core, weight differences between vinyl Si and core-shell silica particles at 800 ^{o}C could be attributed to the amount of polymers in the shell layers.[36] The amounts of polymer shell layer on Si-P and Si-B were found to be close about 35 wt%, indicating that reactivity of two monomers, PEGMA and B-PEGMA, in polymerization is very close. The weight differences between the TGA curves at 800 ^{o}C

before and after purification process could be attributed to the amounts of unattached free polymers[37], and they were found to be 39 wt% and 44 wt% for the free P(B-PEGMA) and free P(PEGMA), respectively.

The molecular weights of detached polymers from Si-P and Si-B by etching process using HF solution were measured by GPC and they were found to be 8,500 for P(B-PEGMA) from Si-B and 7,900 for P(PEGMA) from Si-P, respectively. The molecular weights of unattached free polymers were found to be 12,300 and 11,700 for free P(B-PEGMA) and P(PEGMA), respectively. The smaller molecular weight of detached polymers from Si-B and Si-P than those of free polymers could be ascribed to steric effect; radicals on the silica surface should be much sterically hindered than those in the free polymer chains and then they become less reactive.[38]

4.3.2. Preparation of polymer composite electrolytes (BCP-vinyl Si, BCP-Si-P, and BCP-Si-B)

Polymer composite electrolytes containing different amounts of vinyl Si, Si-P, and Si-B were prepared to study the effects of silica cores and

shell layers on various physicochemical and electrochemical properties of the SPEs. Free-standing films of the polymer composite electrolytes containing various filler contents (10, 20, and 30 wt%) (Figure 4.12) could be easily prepared and their transparent and/or translucent states indicate that the fillers are more or less well-dispersed in the polymer matrix without much aggregation. Furthermore, all the electrolytes are flexible and physically stable. When the polymer composite electrolytes were prepared using larger filler content than 30 wt%, electrolyte films became quite opaque and brittle, indicating that the fillers are aggregated forming large separated domains. Therefore, 30 wt% of filler content was decided to be the maximum content for preparation of the polymer composite electrolytes. $LiClO_4$ was chosen as a lithium salt for the preparation of polymer composite electrolytes because boron has been known to be more strongly interacted with hard Lewis basic anions such as $CF_3SO_3^-$ and ClO_4^- than soft basic anions such as $N(CF_3SO_2)_2^-$.[39] The concentration of $LiClO_4$ was fixed as [Li]/[EO] = 0.07 based on our previous studies on pure polymer electrolyte systems using the polymer matrix materials, BCP, used in this study; maximum ionic conductivity was observed at this concentration.[6, 7] SEM image of

BCP-vinyl Si 30 shows aggregated particles, while those of BCP-Si-P 30 and BCP-Si-B 30 show well-dispersed particles as shown in Figure 4.13. Therefore, core-shell silica particles (Si-P and Si-B) are much more compatible with the polymer matrix than vinyl Si without the shell layers. Obviously, shell layers comprising P(PEGMA) or P(B-PEGMA) can increase compatibility between fillers and polymer matrix because PEGMA units in the polymer matrix, BCP, can be well interacted with the same ethylene oxide units in the shell layers on Si-P and Si-B. On the contrary, BCP is not compatible with more or less hydrophobic vinyl Si having vinyl groups on the surface.[40, 41] In polymer composite electrolyte systems, it is very desirable for the fillers to be well-dispersed because aggregated filler domains can act as barriers to prevent ion transport.[6, 42]

4.3.3. Mechanical and electrochemical stability of polymer composite electrolytes

Mechanical reinforcement effect of the core-shell silica fillers was studied by measuring mechanical properties such as Young's modulus, tensile strength, and elongation at break from stress-strain curves as

presented in Figure 4.14 and these values are listed in Table 4.1. It was found that incorporation of core-shell silica fillers (Si-P and Si-B) increases both Young's modulus and tensile strength of the electrolytes, which is attributed to reinforcement effect of rigid inorganic silica core well-dispersed in the polymer matrix. For example, 30 wt% of Si-P increases Young's modulus and tensile strength by 23 and 7 times, respectively, and 30 wt% of Si-B increases them by 25 and 8 times, respectively, compared with those of polymer matrix, BCP. The percentage of elongation at break was found to decrease with the increase of filler contents. Similar increases in mechanical strength and decrease in flexibility have been reported by other groups.[32, 34, 35] Mechanical properties of BCP-vinyl Si could not be obtained because dog-bone samples are too brittle to maintain their shapes during the measurement in testing equipment. Since hydrophobic vinyl Si particles are aggregated in the polymer matrix (see Figure 4.13(a)), the electrolytes are not physically stable.[43] Therefore, it is worthy to note that P(PEGMA) and P(B-PEGMA) in the shell layers increase compatibility with BCP, and then mechanically stable polymer composite electrolytes could be obtained.

The incorporation of core-shell silica fillers was found to improve

thermal/dimensional stability of the polymer matrix, BCP. When the BCP was heated to 100 ^{o}C, it shrank to smaller size and converted to a waxy state within 2 min, because T_gs of P(PEGMA) segments and POSS moiety in BCP are below 100 ^{o}C like about –67 ^{o}C and 76 ^{o}C, respectively.[7] In contrast, when BCP-Si-B having different amount of Si-B were heated to 100 ^{o}C, all the electrolytes maintain their shapes, sizes, and solid-state even after several days at 100 ^{o}C, indicating that these polymer composite electrolytes could be used for high-temperature applications. The photographs of electrolytes at 25 ^{o}C and 100 ^{o}C are presented in Figure 4.15.

Electrochemical stability of polymer composite electrolytes was evaluated using linear sweep voltammetry. Figure 4.16 shows linear sweep voltammogram of BCP, BCP-Si-P 30, and BCP-Si-B 30 having the maximum filler content, 30 wt%. The abrupt rise in current corresponding to decomposition of electrolyte limits operation voltage range of electrodes. It was revealed that BCP, BCP-Si-P, and BCP-Si-B exhibit wide electrochemically stable window (~ 4.3 V), indicating that these electrolytes are not degraded within a voltage range of 4 V class cathode materials.

4.3.4. Ion transport properties

Figure 4.17 shows ionic conductivities of polymer composite electrolytes containing different filler contents (10, 20, and 30 wt%) at 30 ^{o}C. Ionic conductivity of polymer composite electrolytes having filler contents larger than 30 wt% could not be measured because they are not mechanically stable as described previously. When the core-shell silica fillers (Si-P and Si-B) were introduced, ionic conductivity continuously increases with the filler content up to 30 wt%. On the contrary, ionic conductivity of the polymer composite electrolyte having vinyl Si without any shell layers continuously decreases with the filler content due to poor dispersion state of hydrophobic vinyl Si which disturbs the ion conduction.[14, 16] Furthermore, the incorporation of vinyl Si dilutes the concentration of ion-conducting ethylene oxide units in the polymer composite electrolytes, resulting in decrease of ionic conductivity, while both Si-P and Si-B do not decrease that much because they have additional ion-conducting polymer shell. Interestingly, this ionic conductivity behavior is well consistent with trends in free anion (ClO_4^-) fraction (Figure 4.18). The free anion fraction was calculated using FT-IR analysis method.[30] Thus, the

more free ions in the electrolyte system, the larger the ionic conductivity. When vinyl Si was used as filler, free anion fraction was found to be even smaller than that of the BCP without any filler, and it decreases with the increase in filler content. Obviously, aggregated hydrophobic vinyl Si fillers in the polymer matrix decrease interfacial area of fillers interacting with lithium salts and serve as a barrier disturbing the ion transport.[44] Free anion fraction values of BCP-Si-B are larger than those of BCP-Si-P or BCP-vinyl Si, indicating that boron moiety in Si-B effectively increases the amount of dissociated lithium salt, because boron moiety can trap the anion. Furthermore, increase in Si-B content further increases the free anion fraction values, while increase in Si-P does not increase the free anion fraction value much. Still, the free anion fraction values of BCP-Si-P are larger than those of BCP because free volume can be increased by the incorporation of silica fillers in well-dispersed state.[42, 45] Since the number and mobility of both cation and anion can affect the ionic conductivity, one might claim that Si-B can decrease the ionic conductivity because it traps the anion, thereby decreasing the mobility of the anion. Still, ionic conductivities of BCP-Si-B are larger than those of BCP-Si-P, possibly because the increase in

number of dissociated free lithium cation can positively offset the decrease in anion mobility by boron moiety.

The anion-trapping effect of boron moiety in BCP-Si-B could be figured out by observing glass transition temperature (T_g) behaviors of P(PEGMA) and P(B-PEGMA) detached from Si-P and Si-B by HF etching process. Figure 4.19 shows glass transition temperatures (T_g) of detached P(PEGMA) and P(B-PEGMA) with and without lithium salt and core-shell silica fillers; Si-P and Si-B having lithium salt. Although the T_g values of detached P(PEGMA) and P(B-PEGMA) without any lithium salt are quite close as observed at –65 and –68 ^{o}C, respectively, their melting transition peaks are observed at same temperature (–4 ^{o}C) by side chain crystals formed by same ethylene oxide units in the side chains of polymers. The slightly smaller T_g value of P(B-PEGMA) than that of P(PEGMA) could be ascribed to the bulky boronic ester group that can easily increase free volume of the polymers, resulting in decreasing the T_g.[7, 46, 47] When lithium salt ([Li]/[EO]=0.07) is added to the polymers, melting transition peaks disappear because lithium salt can suppress the crystallization of the side chains.[48] T_gs of both P(B-PEGMA) and P(PEGMA) are increased by the addition of lithium salt because pseudo-crosslinked

structures formed by interactions between ethylene oxide units and lithium cation can decrease chain mobility.[49] Furthermore, T_g values of detached P(B-PEGMA) (–40 ^{o}C) and attached P(B-PEGMA) on the Si-B (-37 ^{o}C) are quite larger than those of the detached P(PEGMA) (–56 ^{o}C) and attached P(PEGMA) on the Si-P (-52 ^{o}C), respectively. The larger T_g values of the polymer chains attached on the silica particles than those of the detached polymer chains are because the polymer chains on the silica particles are less mobile than the corresponding free polymer chains.[51] The larger T_g values of P(B-PEGMA) having $LiClO_4$ than those of P(PEGMA) can be ascribed to the decrease in the chain mobility because larger amount of lithium salts are dissociated in the P(B-PEGMA) due to the anion-trapping boron moiety. It has been generally reported that polymers having larger amounts of lithium salt exhibit larger T_g value because lithium cation can act as a transient crosslinking agent.[52] In addition, interaction between boron moiety in P(B-PEGMA) and anion of lithium salt by acid-base interaction can also decrease the chain mobility.

Although the chain mobility of ion-conducting segments decreases with the incorporation of boron moiety in the shell layer, ionic

conductivity of BCP-Si-B is still larger than that of BCP-Si-P because large amount of charge carriers by boron moiety can offset the decrease in chain mobility. It is also well known that filler particles can provide additional ion-conducting pathway to facilitate the ion transport by increasing the free volume of the polymer matrix.[42]

To evaluate the anion-trapping effect of boron moiety quantitatively, lithium transference numbers (T_{Li+}) of the polymer composite electrolytes were measured using DC polarization/AC impedance combination method (Figure 4.20).[50] T_{Li+} of BCP-Si-B linearly increases with the filler content and maximum T_{Li+} value of 0.67 was observed for BCP-Si-B 30. T_{Li+} of BCP-Si-P also increases with the filler content, while the increase is much less compared to that of BCP-Si-B. Therefore, boron moiety in Si-B can more effectively trap the anion of the lithium salt than the pure ethylene oxide moiety in Si-P, resulting in larger T_{Li+} values. T_{Li+} values of BCP-vinyl Si were found to even decrease with the filler content. Since vinyl Si particles are poorly dispersed in the polymer matrix, BCP, they probably act as barriers for ion transport. Furthermore, aggregation of filler decreases interfacial area interacting with the lithium salt, resulting in smaller dissociation of the lithium salt.[41, 44] For the same reasons, BCP-

vinyl Si show smaller ionic conductivity value than those of BCP-Si-B and BCP-Si-P. This kind of behavior has been reported by other groups.[44, 51] In our case, Si-P and Si-B can increase both T_{Li+} and ionic conductivity because they are compatible with the polymer matrix and also increase dissociation of the lithium salt.

The effect of lithium salt on the ion transport properties was also investigated using other lithium salts such as $LiCF_3SO_3$ and LiTFSI (Figure 4.21). It was found that ionic conductivity and transference number values of BCP-Si-B 30 having $LiClO_4$ and $LiCF_3SO_3$ are larger than those of BCP-Si-B 30 having LiTFSI because boron can interact with hard Lewis basic anions such as $CF_3SO_3^-$ and ClO_4^- more strongly than soft basic anions such as $N(CF_3SO_2)_2^-$.[40] Comparing $CF_3SO_3^-$ and ClO_4^-, the polymer composite electrolyte having $LiClO_4$ shows slightly larger values than that having LiTFSI.

Since Si-B is very effective filler materials to improve the electrochemical properties of BCP due to the anion-trapping ability of the boron moiety, P(B-PEGMA) itself without the silica core part can also improve those properties. However, when about 10 wt% of P(B-PEGMA) was mixed with BCP, the resulting mixture turned into a wax state because P(B-PEGMA) has very low T_g value as shown in

Figure 4.19. Since the main objective of this study is to develop a novel solid polymer electrolyte system for all-solid-state lithium-ion batteries, we did not try to prepare the polymer electrolytes using P(B-PEGMA). The effect of the boron moiety for the electrolytes in liquid or wax state was already reported by others before.[24,27,29-32]

4.3.5. Interfacial compatibility and cycle performance

Since lithium metal easily reacts with any kinds of compounds in electrolytes including oxygen and residual solvents, passivating solid electrolyte interphase (SEI) layers are inevitably formed at the interface between lithium metal anodes and electrolytes, resulting in increase of interfacial resistance.[52, 53] Although the SEI layers can suppress further possible side reactions between lithium and impurities, they can also increase interfacial resistance against efficient charge transport and accelerate growth of lithium dendrites especially when they have irregular structures.[54-56] Inorganic filler materials such as silica, zeolite, and metal organic framework (MOF) have been known to suppress formation of irregular passivating layer effectively by decreasing exposed surface area of the lithium metal

interacting with the electrolyte.[22, 23, 57, 58] Furthermore, silica particles have been known to suppress the interfacial side reactions because they can trap organic impurities including solvents by interactions between the organic impurities and polar groups on silica surface.[23, 59]

Interfacial resistances of polymer composite electrolytes were measured using symmetrically assembled Li/electrolyte/Li coin cells stored under open-circuit condition at 60 ^{o}C for 50 days to estimate the formation of SEI layers and compatibility of the electrolytes with the lithium metal anode. As shown in Figure 4.22, interfacial resistance of BCP without filler increases rapidly with storage time and their resistance values are much larger than those of polymer composite electrolytes having fillers. Therefore, it can be concluded that stable interfacial SEI layers are formed at the lithium metal surface for the polymer composite electrolytes having fillers. Although the interfacial resistance values of BCP-vinyl Si are smaller than that of BCP, they are still larger than those of BCP-Si-P and BCP-Si-B; poorly dispersed vinyl Si particles cannot effectively suppress the increase of interfacial resistance. It was further revealed that increase of Si-B content from 10 wt% to 30 wt% decreases interfacial

resistances (see Figure 4.23), indicating that larger amount of compatible Si-B fillers can more effectively decrease the exposed surface area of lithium metal and side reactions.

Figure 4.24 shows cycle performance of all-solid-state batteries assembled with Li/SPEs/V_2O_5, where SPEs are BCP, BCP-Si-P 30, and BCP-Si-B 30, respectively. Filler content was fixed as 30 wt% because the maximum ionic conductivities were observed at this concentration. Liquid electrolytes have been known to be not stable at high temperature due to their volatility and flammability, resulting in serious safety problems.[60] In contrast, our SPEs show stable cycle behavior at 60 ^{o}C for 50 cycles. The initial capacity value of BCP-Si-B 30 is 291 mAh g^{-1}, which is very close to the theoretical capacity of V_2O_5, and BCP-Si-B exhibited larger capacity and retention values than those of BCP or BCP-Si-P due to the larger ionic conductivity, anion-trapping effect of boron moiety, and smaller interfacial resistance. As a result, BCP-Si-B 30 shows large capacity value and retention (80 %) than BCP and BCP-Si-P 30; the retentions of BCP and BCP-Si-P 30 are 65 % and 64 %, respectively. Therefore, it was clearly demonstrated that the incorporation of boron moiety in the SPEs remarkably increases both capacity and retention. Further works

to study the cycle performance on rate property, cycle reversibility, and high-temperature condition over 60 ^{o}C are under progress.

4.4. Conclusions

In this study, core-shell silica particles with ion-conducting poly(ethylene glycol) and anion-trapping boron moiety in the shell layer were prepared and used as filler materials of polymer composite electrolytes for all-solid-state lithium-ion battery applications. Mechanical strength and thermal stability of the polymer matrix were increased by incorporating core-shell silica particle into the polymer matrix. Furthermore, dimensional stability of the polymer composite electrolytes maintained even at elevated temperature up to 100 ^{o}C, suggesting possible applications for high-temperature batteries. Maximum ionic conductivity of 1.6×10^{-4} S/cm at 30 ^{o}C was achieved when 30 wt% of core-shell silica particle having boron moiety in the shell layer was incorporated and this value is one order of magnitude higher than that of the polymer matrix because boron moiety effectively traps anion of lithium salt, thereby increasing the amount of dissociated lithium ion. Moreover, excellent interfacial

compatibility between polymer composite electrolytes and lithium metal anode was observed since well-dispersed fillers act as protective layer on lithium surface by suppressing possible interfacial side reactions. All of these electrochemical advantages of polymer composite electrolytes contribute to obtain excellent cycle performance at high temperature, 60 ^{o}C.

4.5. References

[1] J. M. Tarascon and M. Armand, *Nature* **2001,** *414*, 359-367.

[2] W. H. Meyer, *Adv. Mater.* **1998,** *10*, 439-448.

[3] D. G. Kim, J. M. Shim, J. H. Lee, S. J. Kwon, J. H. Baik and J. C. Lee, *Polymer* **2013,** *54*, 5812-5820.

[4] D. G. Kim, H. S. Sohn, S. K. Kim, A. Lee and J. C. Lee, *J. Polym. Sci., Part A: Polym. Chem.* **2012,** *50*, 3618-3627.

[5] S. K. Kim, D. G. Kim, A. Lee, H. S. Sohn, J. J. Wie, N. A. Nguyen, M. E. Mackay and J. C. Lee, *Macromolecules* **2012,** *45*, 9347-9356.

[6] J. Shim, D. G. Kim, H. J. Kim, J. H. Lee, J. H. Baik and J. C. Lee, *J. Mater. Chem. A* **2014,** *2*, 13873-13883.

[7] J. Shim, D.-G. Kim, J. H. Lee, J. H. Baik and J.-C. Lee, *Polym. Chem.* **2014,** *5*, 3432-3442.

[8] R. Khurana, J. L. Schaefer, L. A. Archer and G. W. Coates, *J. Am. Chem. Soc.* **2014,** *136*, 7395-7402.

[9] S. H. Kim, K. H. Choi, S. J. Cho, E. H. Kil and S. Y. Lee, *J. Mater. Chem. A* **2013,** *1*, 4949-4955.

[10] S. Liu, N. Imanishi, T. Zhang, A. Hirano, Y. Takeda, O. Yamamoto and J. Yang, *J. Electrochem. Soc.* **2010,** *157*, A1092-A1098.

[11] D. Zhou, X. G. Mei and J. Y. Ouyang, *J. Phys. Chem. C* **2011,** *115*, 16688-16694.

[12] C. Y. Tang, K. Hackenberg, Q. Fu, P. M. Ajayan and H. Ardebili, *Nano Lett.* **2012,** *12*, 1152-1156.

[13] S. H. Ju, Y. S. Lee, Y. K. Sun and D. W. Kim, *J. Mater. Chem. A* **2013,** *1*, 395-401.

[14] X. L. Hu, G. M. Hou, M. Q. Zhang, M. Z. Rong, W. H. Ruan and E. P. Giannelis, *J. Mater. Chem.* **2012,** *22*, 18961-18967.

[15] Y. S. Lee, S. H. Ju, J. H. Kim, S. S. Hwang, J. M. Choi, Y. K. Sun, H. Kim, B. Scrosati and D. W. Kim, *Electrochem. Commun.* **2012,** *17*, 18-21.

[16] Y. W. Chen-Yang, Y. L. Wang, Y. T. Chen, Y. K. Li, H. C. Chen and H. Y. Chiu, *J. Power Sources* **2008,** *182*, 340-348.

[17] K. Jeddi, K. Sarikhani, N. T. Qazvini and P. Chen, *J. Power Sources* **2014,** *245*, 656-662.

[18] Z. Jia, W. Yuan, H. Zhao, H. Y. Hu and G. L. Baker, *RSC Adv.* **2014,** *4*, 41087-41098.

[19] J. L. Nugent, S. S. Moganty and L. A. Archer, *Adv. Mater.* **2010,** *22*, 3677-3680.

[20] Y. Y. Lu, S. S. Moganty, J. L. Schaefer and L. A. Archer, *J. Mater. Chem.* **2012,** *22*, 4066-4072.

[21] J. L. Schaefer, D. A. Yanga and L. A. Archer, *Chem. Mater.* **2013,** *25*, 834-839.

[22] S. Liu, N. Imanishi, T. Zhang, A. Hirano, Y. Takeda, O. Yamamoto and J. Yang, *J. Power Sources* **2010,** *195*, 6847-6853.

[23] H. J. Walls, J. Zhou, J. A. Yerian, P. S. Fedkiw, S. A. Khan, M. K. Stowe and G. L. Baker, *J. Power Sources* **2000,** *89*, 156-162.

[24] H. S. Lee, X. Q. Yang, C. L. Xiang, J. McBreen and L. S. Choi, *J. Electrochem. Soc.* **1998,** *145*, 2813-2818.

[25] R. Kurono, M. A. Mehta, T. Inoue and T. Fujinami, *Electrochim. Acta* **2001,** *47*, 483-487.

[26] F. Jakle, *Coord. Chem. Rev.* **2006,** *250*, 1107-1121.

[27] T. Mizumo, K. Sakamoto, N. Matsumi and H. Ohno, *Electrochim. Acta* **2005,** *50*, 3928-3933.

[28] K. L. Mathews, A. M. Budgin, S. Beeram, A. T. Joenathan, B. D. Stein, U. Werner-Zwanziger, M. Pink, L. A. Baker, W. E. Mahmoud, J. P. Carini and L. M. Bronstein, *J. Mater. Chem. A* **2013,** *1*, 1108-1116.

[29] L. F. Li, H. S. Lee, H. Li, X. Q. Yang and X. J. Huang, *Electrochem. Commun.* **2009,** *11*, 2296-2299.

[30] Y. M. Lee, J. E. Seo, N. S. Choi and J. K. Park, *Electrochim. Acta* **2005,** *50*, 2843-2848.

[31] N. S. Choi, S. W. Ryu and J. K. Park, *Electrochim. Acta* **2008,** *53*, 6575-6579.

[32] N. S. Choi, Y. M. Lee, K. Y. Cho, D. H. Ko and J. K. Park, *Electrochem. Commun.* **2004,** *6*, 1238-1242.

[33] A. Chakrabarti, R. Filler and B. K. Mandal, *J. Solid State Electrochem.* **2008,** *12*, 269-272.

[34] M. Benaglia, E. Rizzardo, A. Alberti and M. Guerra, *Macromolecules* **2005,** *38*, 3129-3140.

[35] H. G. Kuivila, A. H. Keough and E. J. Soboczenski, *J. Org. Chem.* **1954,** *19*, 780-783.

[36] L. J. Zhu, L. P. Zhu, Y. F. Zhao, B. K. Zhu and Y. Y. Xu, *J. Mater. Chem. A* **2014,** *2*, 15566-15574.

[37] T. Borase, M. Iacono, S. I. Ali, P. D. Thornton and A. Heise, *Polym. Chem.* **2012,** *3*, 1267-1275.

[38] B. Bailly, A. C. Donnenwirth, C. Bartholome, E. Beyou and E. Bourgeat-Lami, *Macromol. Res.* **2008**, *16*, 134-481.

[39] Y. Kato, K. Suwa, H. Ikuta, Y. Uchimoto, M. Wakihara, S. Yokoyama, T. Yabe and M. Yamamoto, *J. Nanomater.* **2006,** *76371*, 1-10.

[40] L. X. Xu, F. Xu, F. Chen, J. T. Yang and M. Q. Zhong, *J. Mater. Chem.* **2003,** *13*, 280-285.

[41] M. Z. Rong, M. Q. Zhang, Y. X. Zheng, H. M. Zeng, R. Walter and K. Friedrich, *J. Nanomater.* **2012,** *457967*, 1-10.

[42] Q. Li, E. Wood and H. Ardebili, *J. Power Sources* **2003,** *117*, 124-130.

[43] S. Ishibe, K. Anzai, J. Nakamura, Y. Konosu, M. Ashizawa, H. Matsumoto and Y. Tominaga, *Appl. Phys. Lett.* **2013,** *102*, 243903.

[44] J. Y. Xi and X. Z. Tang, *React. Funct. Polym.* **2014,** *81*, 40-44.

[45] T. C. Merkel, B. D. Freeman, R. J. Spontak, Z. He, I. Pinnau, P. Meakin and A. J. Hill, *J. Power Sources* **2015,** *279*, 405-412.

[46] H.-S. Ryu, D.-G. Kim and J.-C. Lee, *Macromol. Res.* **2010,** *18*, 1021-1029.

[47] H.-S. Ryu, D.-G. Kim and J.-C. Lee, *Polymer* **2010,** *51*, 2296-2304.

[48] T. J. Singh and S. V. Bhat, *Bull. Mater. Sci.* **2003,** *26*, 707-714.

[49] Y. Tominaga, N. Takizawa and H. Ohno, *Electrochim. Acta* **2000,** *45*, 1285-1289.

[50] P. G. Bruce, J. Evans and C. A. Vincent, *Solid State Ionics* **1988,** *28*, 918-922.

[51] S. Kim and S. J. Park, *Electrochim. Acta* **2007,** *52*, 3477-3484.

[52] R. Younesi, M. Hahlin, M. Roberts and K. Edstrom, *J. Power Sources* **2013,** *225*, 40-45.

[53] A. Lewandowski, A. Swiderska-Mocek and L. Waliszewski, *J. Solid State Electrochem.* **2012,** *16*, 3391-3397.

[54] S. M. Choi, I. S. Kang, Y. K. Sun, J. H. Song, S. M. Chung and D. W. Kim, *J. Power Sources* **2013,** *244*, 363-368.

[55] S. H. Lee, J. R. Harding, D. S. Liu, J. M. D'Arcy, Y. Shao-Horn and P. T. Hammond, *Chem. Mater.* **2014,** *26*, 2579-2585.

[56] F. Ding, W. Xu, G. L. Graff, J. Zhang, M. L. Sushko, X. L. Chen, Y. Y. Shao, M. H. Engelhard, Z. M. Nie, J. Xiao, X. J. Liu, P. V.

Sushko, J. Liu and J. G. Zhang, *J. Am. Chem. Soc.* **2013,** *135*, 4450-4456.

[57] C. Gerbaldi, J. R. Nair, M. A. Kulandainathan, R. S. Kumar, C. Ferrara, P. Mustarelli and A. M. Stephan, *J. Mater. Chem. A*, **2014**, *2*, 9948-9954.

[58] J. Y. Xi, X. P. Qiu, M. Z. Cui, X. Z. Tang, W. T. Zhu and L. Q. Chen, *J. Power Sources*, **2006**, *156*, 581-588.

[59] W. L. Qiu, X. H. Ma, Q. H. Yang, Y. B. Fu and X. F. Zong, *J. Power Sources*, **2004**, *138*, 245-252.

[60] K. Murata, S. Izuchi and Y. Yoshihisa, *Electrochim. Acta*, **2000**, *45*, 1501-1508.

Table 4.1. Mechanical properties of BCP and polymer composite electrolytes (BCP-Si-B and BCP-Si-P) having different amount of filler.

	Filler content (wt%)	Young's modulus (MPa)	Tensile strength (MPa)	Elongation at break (%)
BCP	0	12.23 ± 1.1	1.01 ± 0.1	22.8 ± 1.3
BCP-vinyl Si			N/A[a]	
BCP-Si-B 10	10	39.20 ± 0.2	2.32 ± 0.1	18.2 ± 0.6
BCP-Si-B 20	20	154.7 ± 0.7	5.27 ± 0.2	11.4 ± 0.2
BCP-Si-B 30	30	302.6 ± 2.4	8.24 ± 0.4	6.59 ± 0.5
BCP-Si-P 10	10	40.43 ± 1.2	1.20 ± 0.2	20.1 ± 1.2
BCP-Si-P 20	20	127.9 ± 0.8	5.82 ± 0.4	13.4 ± 1.4
BCP-Si-P 30	30	281.5 ± 1.9	7.15 ± 0.5	7.19 ± 0.9

[a] The mechanical properties of BCP-vinyl Si samples could not be obtained because they are too brittle.

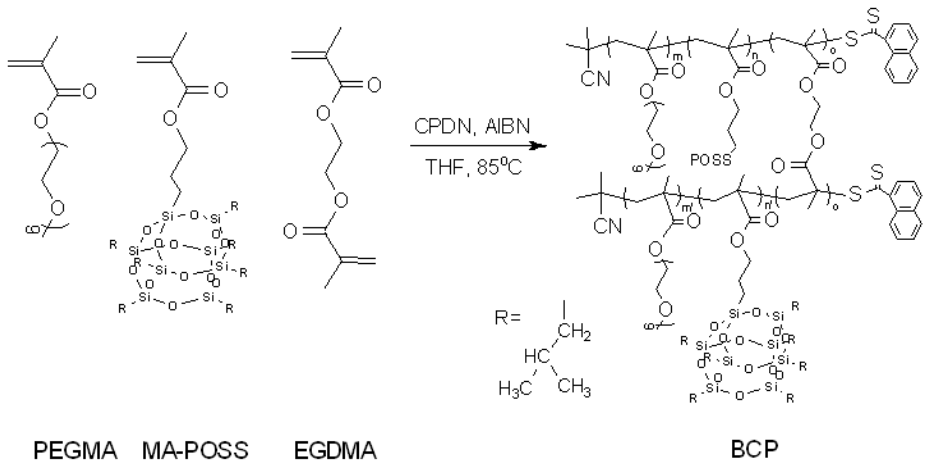

Figure 4.1. Synthesis of organic/inorganic hybrid branched-graft copolymer (BCP) *via* RAFT polymerization.

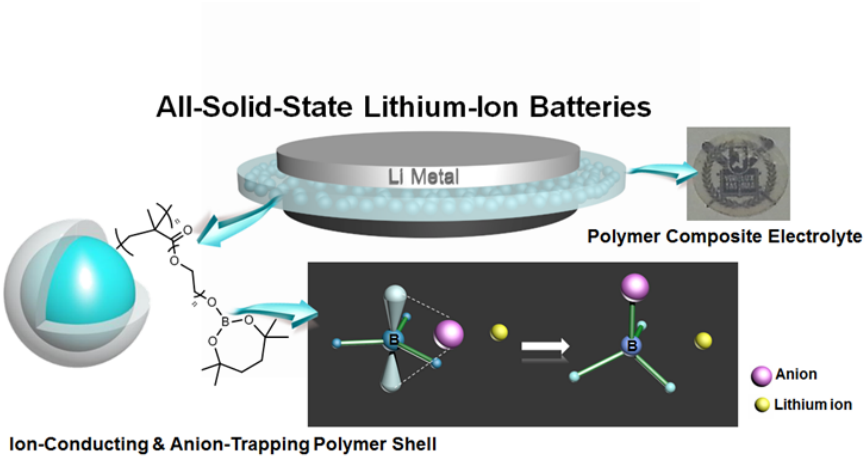

Figure 4.2. Conceptual illustration of polymer composite electrolytes containing core-shell silica filler having ion-conducting poly(ethylene glycol) and anion-trapping boron moiety in the shell layer.

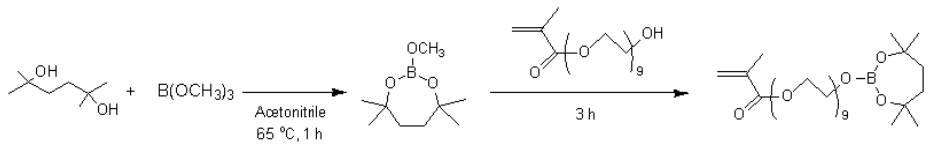

Figure 4.3. Synthesis of PEGMA containing boronic ester group (B-PEGMA).

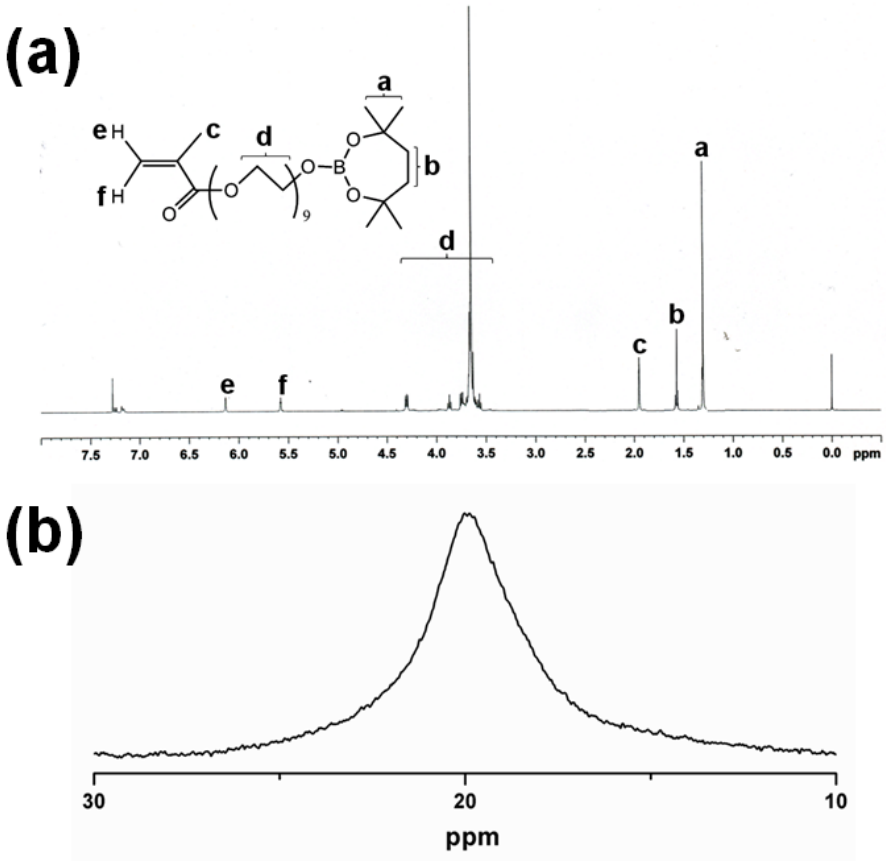

Figure 4.4. (a) ^{1}H NMR spectrum and (b) ^{11}B NMR spectrum of B-PEGMA.

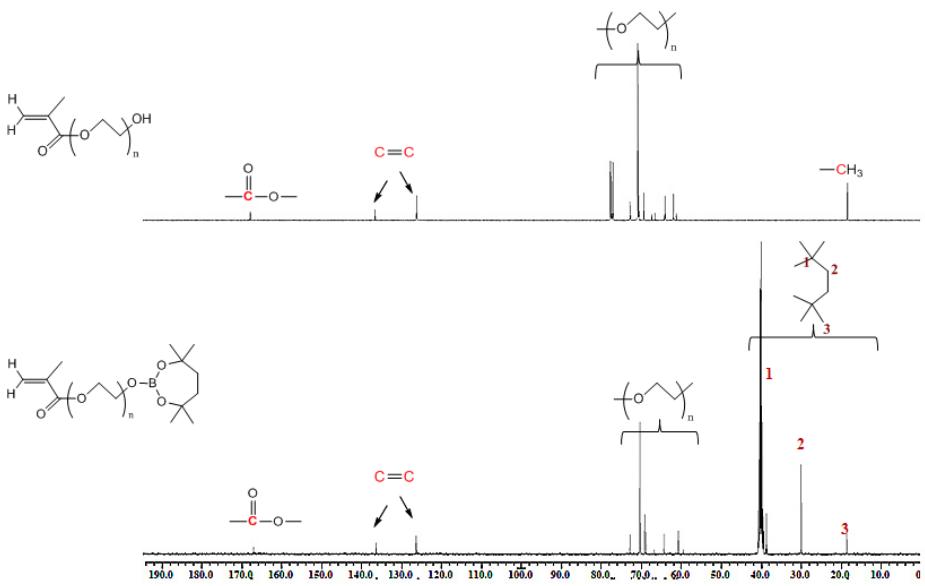

Figure 4.5. ^{13}C NMR of PEGMA and B-PEGMA.

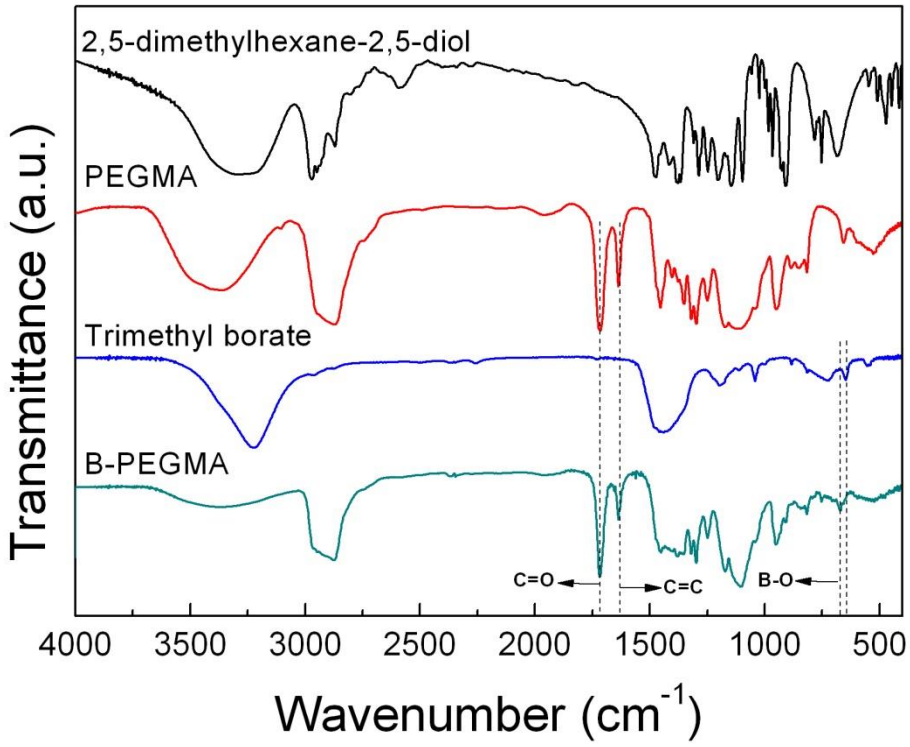

Figure 4.6. FT-IR spectra of B-PEGMA and reactants; 2,5-dimethylhexane-2,5-diol, PEGMA, and trimethyl borate.

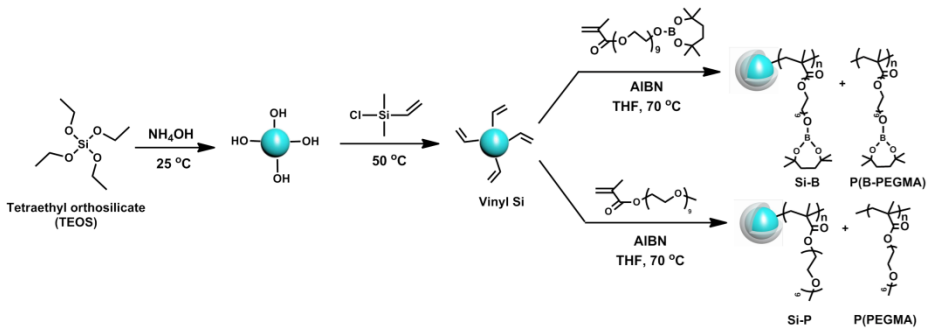

Figure 4.7. Preparation of core-shell silica particles having P(B-PEGMA) and P(PEGMA) in the shell layers abbreviated as Si-B and Si-P, respectively.

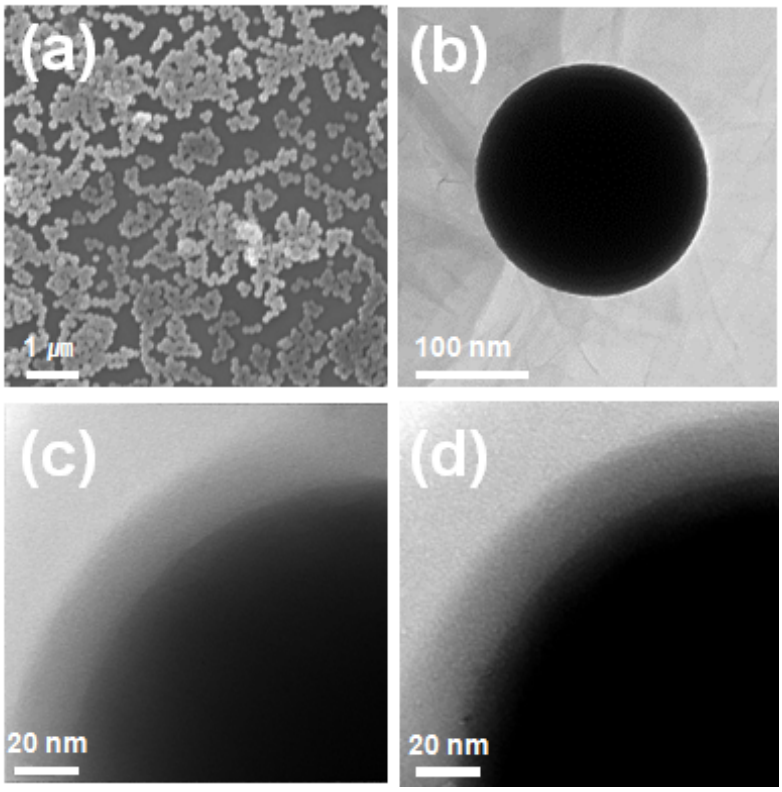

Figure 4.8. (a) SEM micrograph of vinyl Si and TEM micrographs of (b) vinyl Si, (c) Si-P, and (d) Si-B.

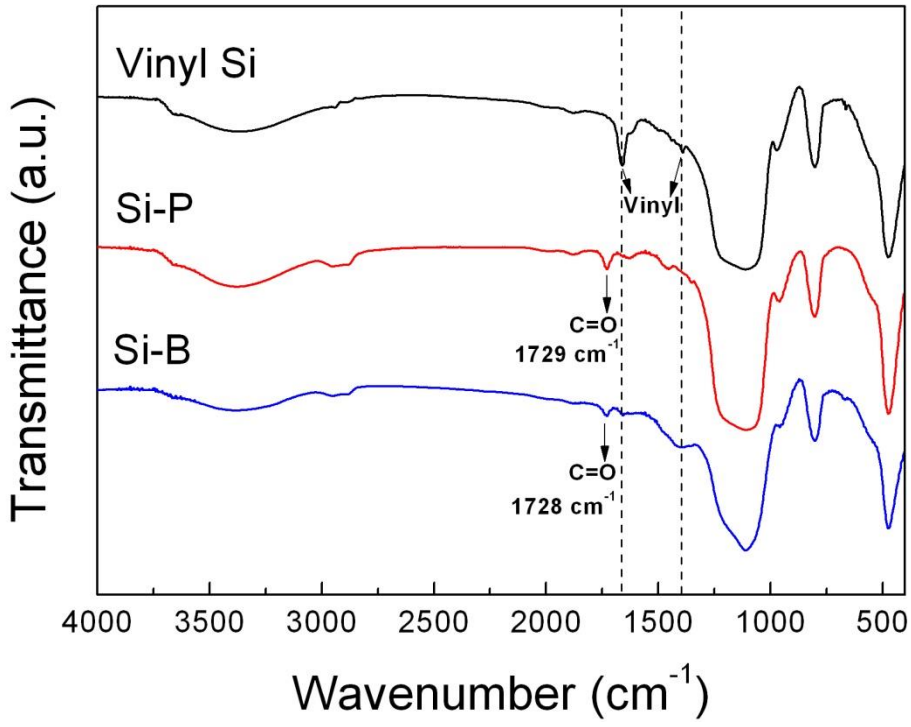

Figure 4.9. FT-IR spectra of vinyl Si, Si-P, and Si-B.

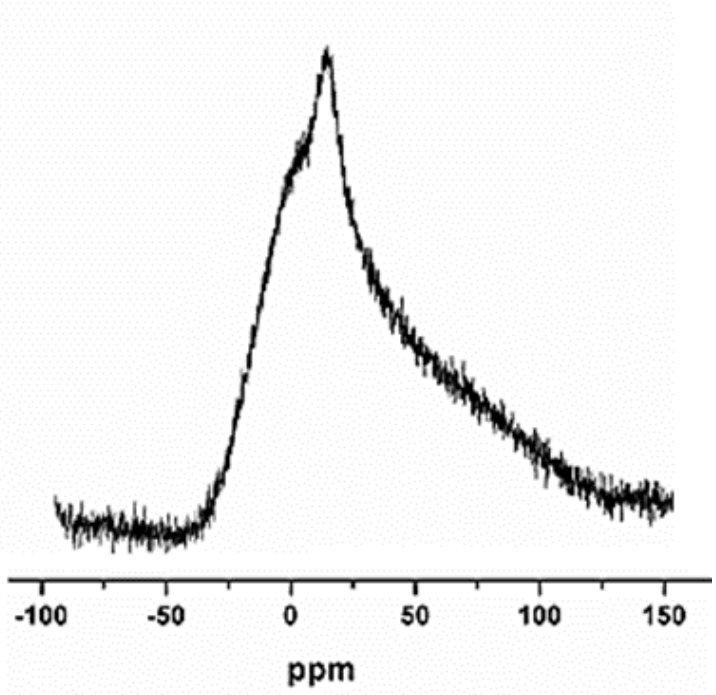

Figure 4.10. Solid-state ^{11}B MAS NMR of Si-B.

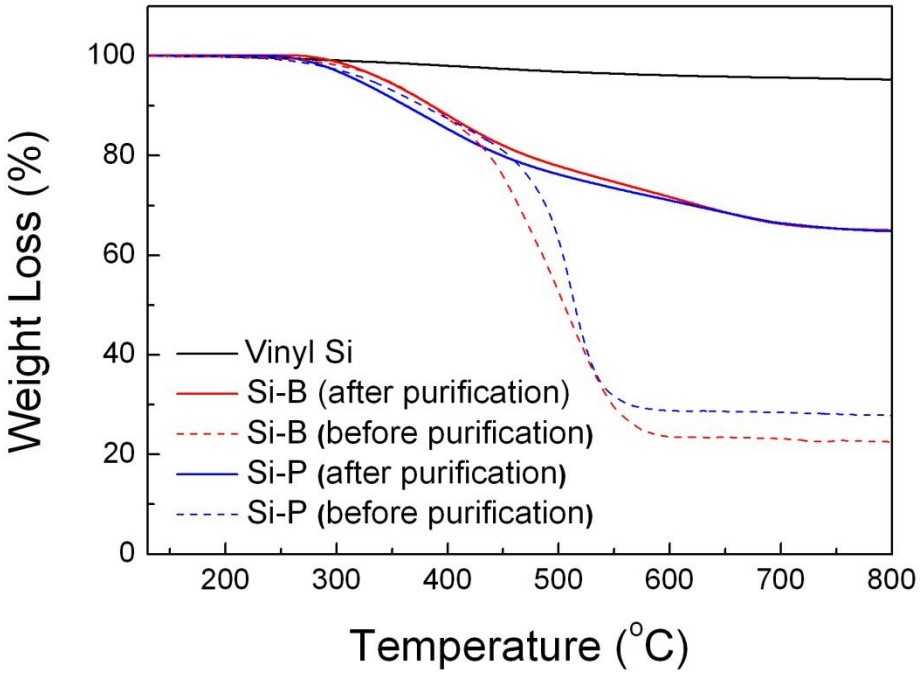

Figure 4.11. TGA profiles of vinyl Si, Si-B, and Si-P (before and after purification process).

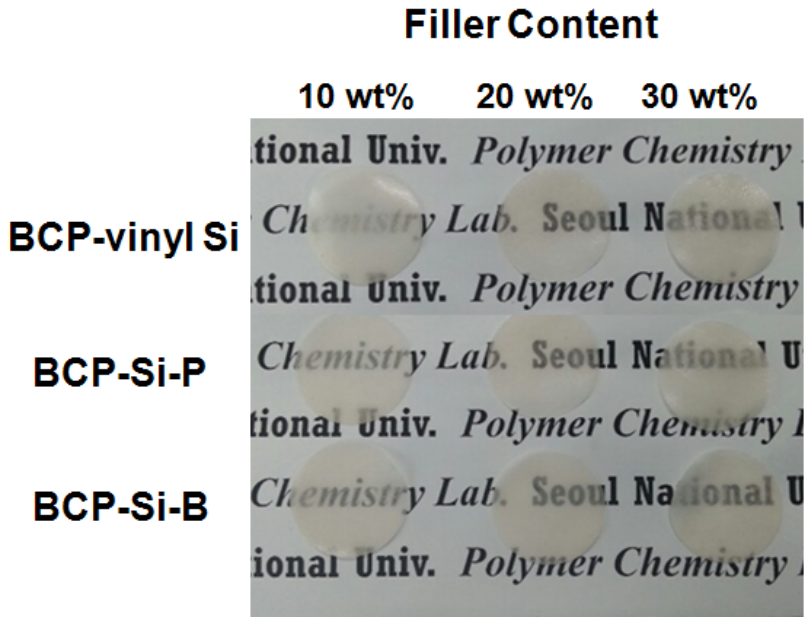

Figure 4.12. Photographs of polymer composite electrolytes (BCP-vinyl Si, BCP-Si-P, and BCP-Si-B) having different amount of vinyl Si, Si-P, and Si-B containing $LiClO_4$ ([Li]/[EO] = 0.07).

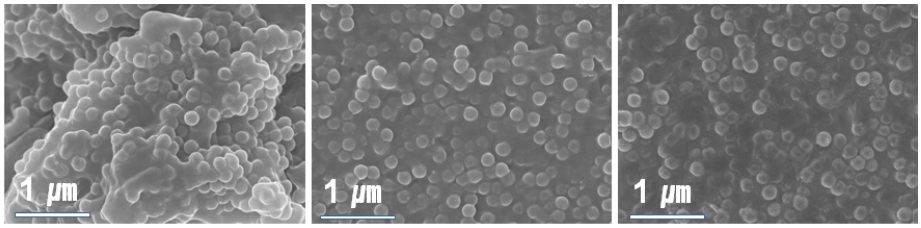

Figure 4.13. SEM images of (a) BCP-vinyl Si 30, (b) BCP-Si-P 30, and (c) BCP-Si-B 30.

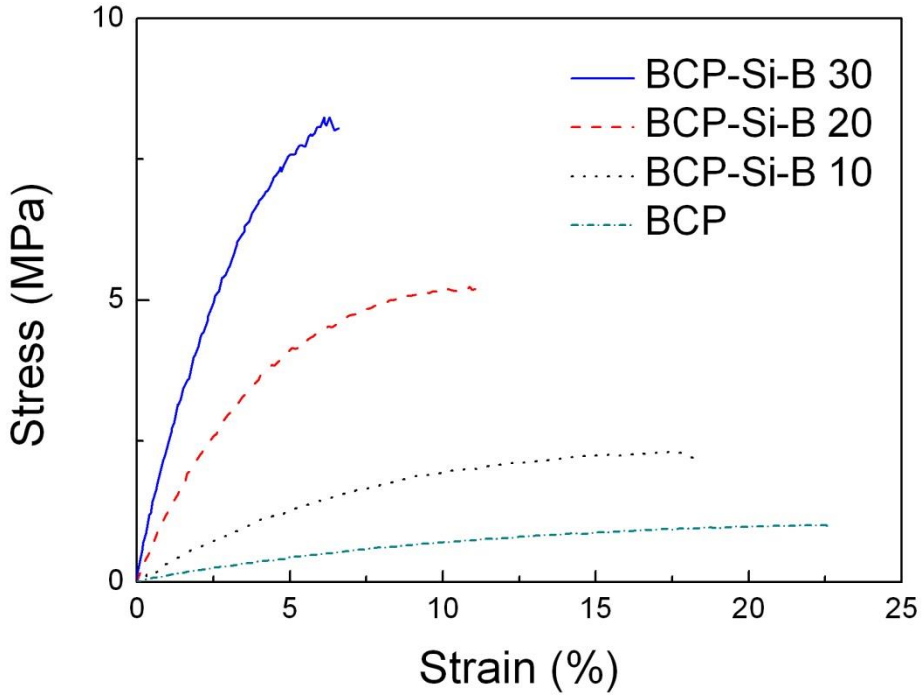

Figure 4.14. Stress-strain curves of BCP and BCP-Si-B having different amount of Si-B, where BCP-Si-B 10, BCP-Si-B 20, and BCP-Si-B 30 represent that they contain 10, 20, and 30 wt% of Si-B, respectively.

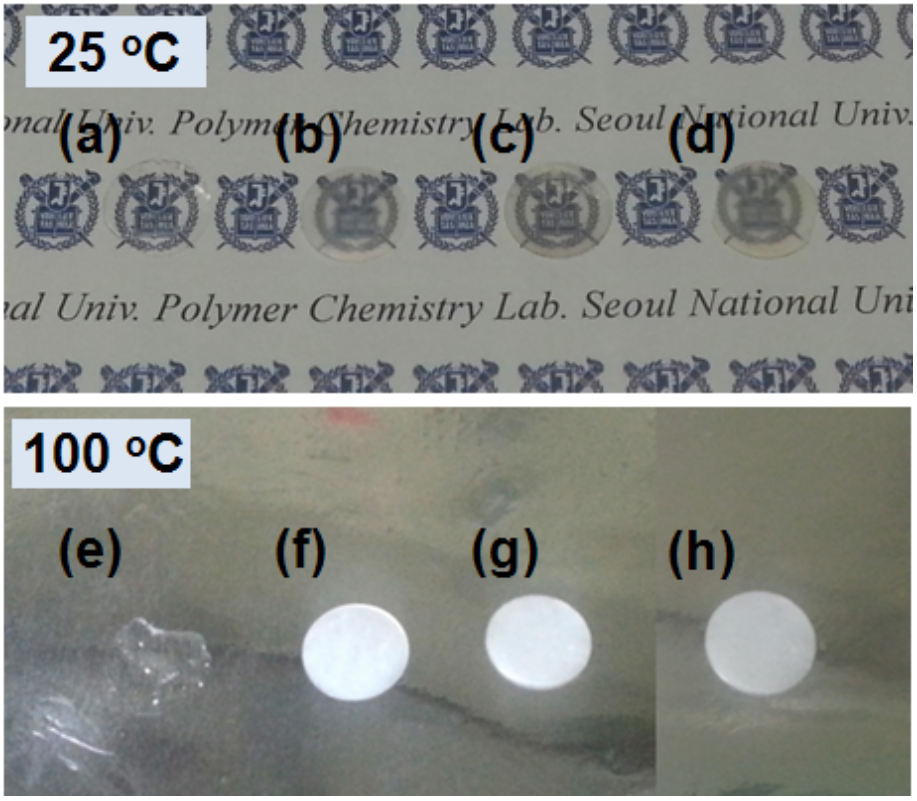

Figure 4.15. Photographs of (a) BCP, (b) BCP-Si-B 10, (c) BCP-Si-B 20, and (d) BCP-Si-B 30 at 25 ^{o}C and (a) BCP, (b) BCP-Si-B 10, (c) BCP-Si-B 20, and (d) BCP-Si-B 30 at 100 ^{o}C.

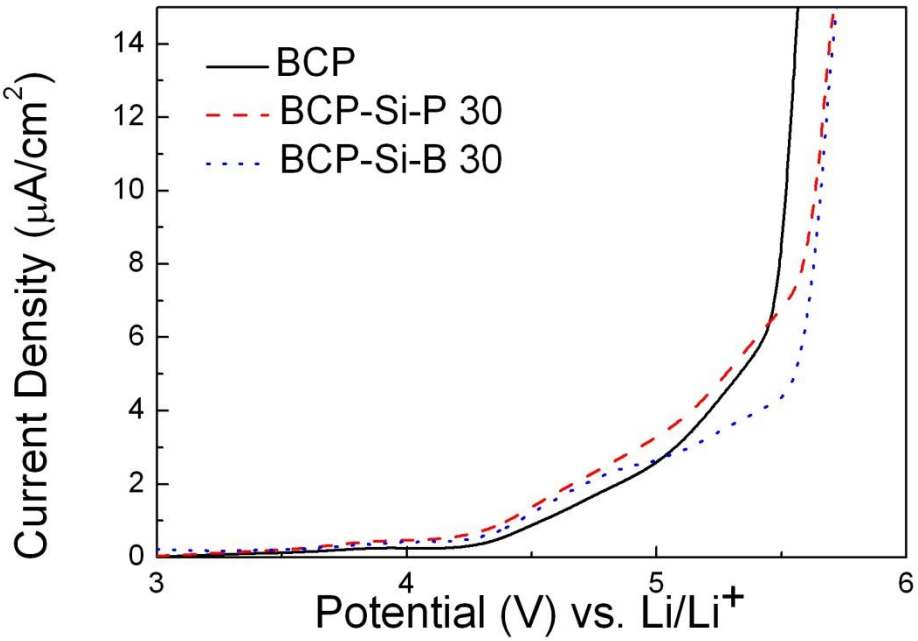

Figure 4.16. Linear sweep voltammogram of BCP and polymer composite electrolytes having 30 wt% of Si-P and Si-B (BCP-Si-P 30 and BCP-Si-B 30) at 60 ^{o}C with a scan rate of 1 mV/s.

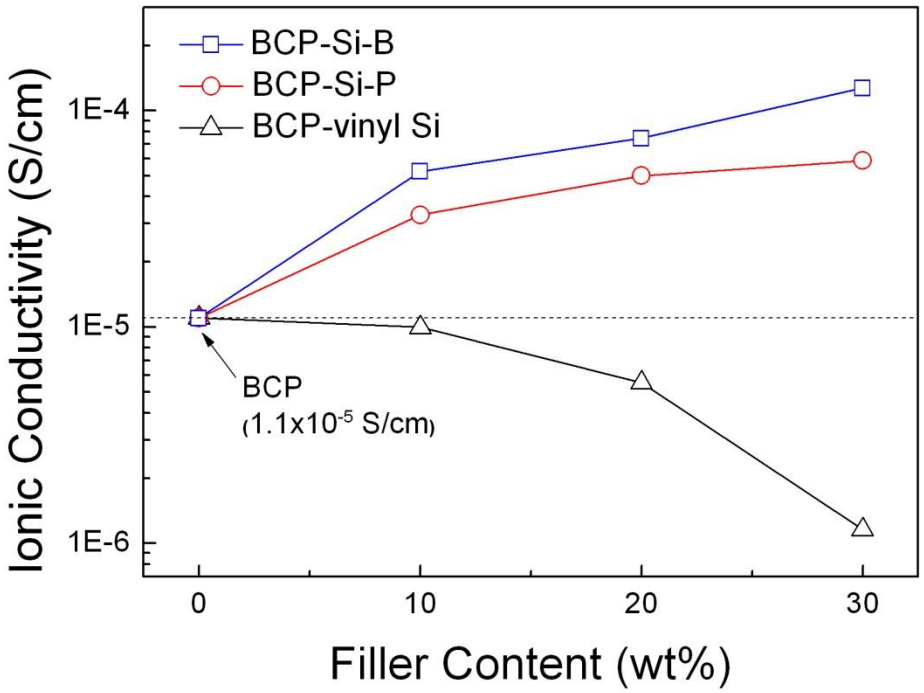

Figure 4.17. Ionic conductivities of polymer composite electrolytes (BCP-Si-B, BCP-Si-P, and BCP-vinyl Si) having different amount of filler at 30 ^{o}C.

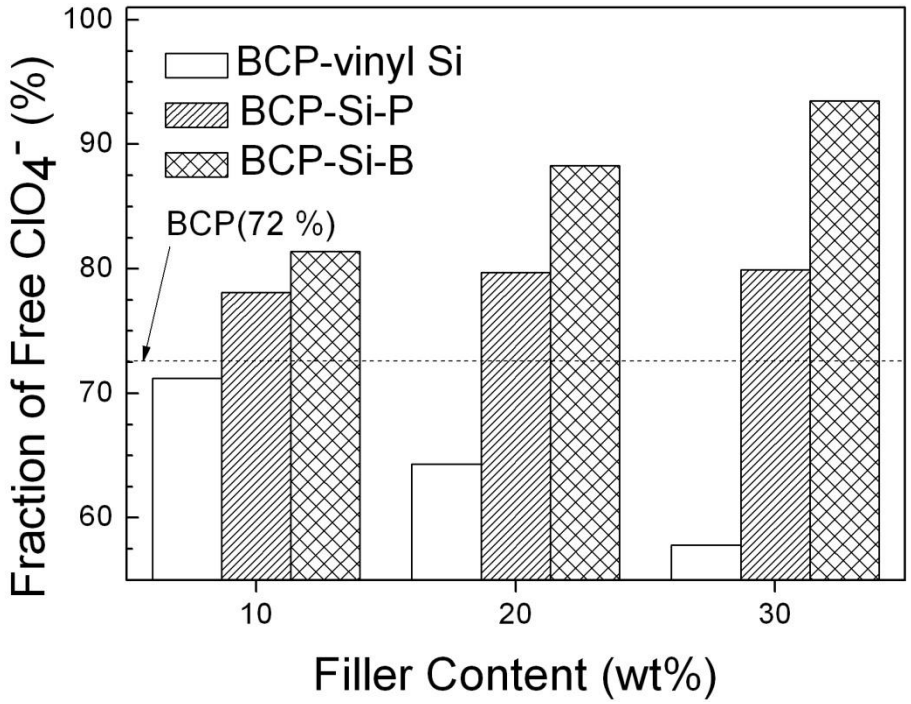

Figure 4.18. Fractions of free ClO_4^- anion of polymer composite electrolytes (BCP-vinyl Si, BCP-Si-P, and BCP-Si-B) having different amount of filler.

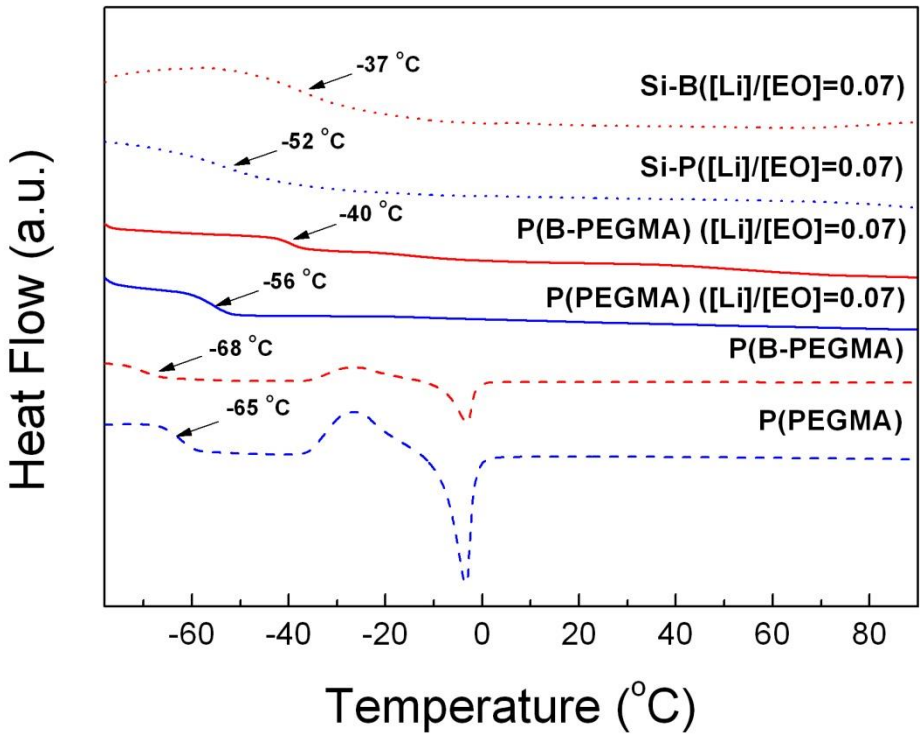

Figure 4.19. DSC thermogram of detached P(B-PEGMA) and P(PEGMA); with and without $LiClO_4$ and core-shell silica fillers; Si-P and Si-B with $LiClO_4$.

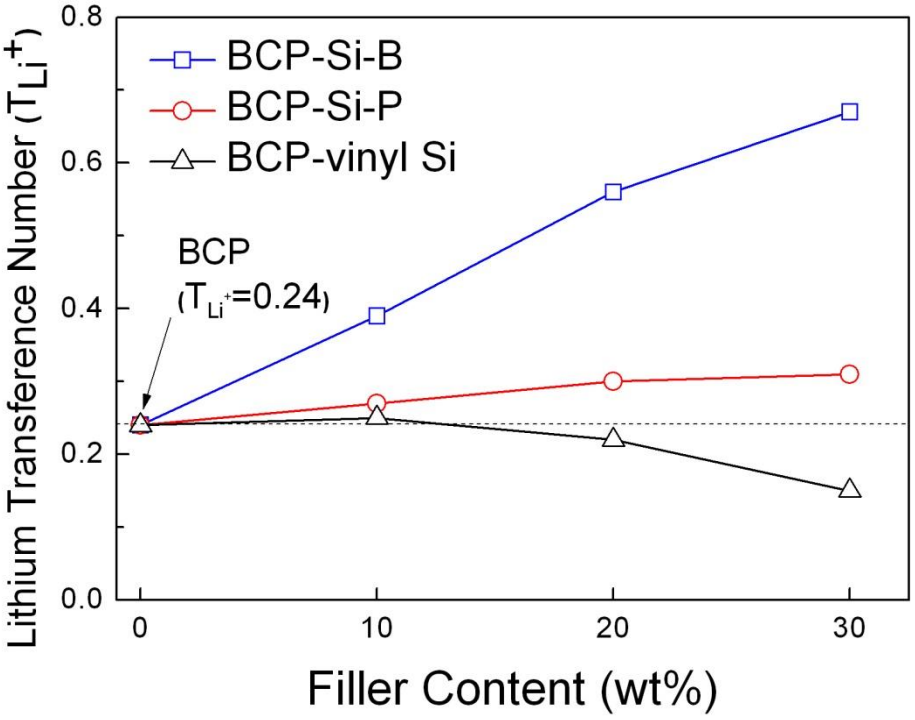

Figure 4.20. Lithium transference numbers of polymer composite electrolytes (BCP-Si-B, BCP-Si-P, and BCP-vinyl Si) having different amount of filler at 60 ^{o}C.

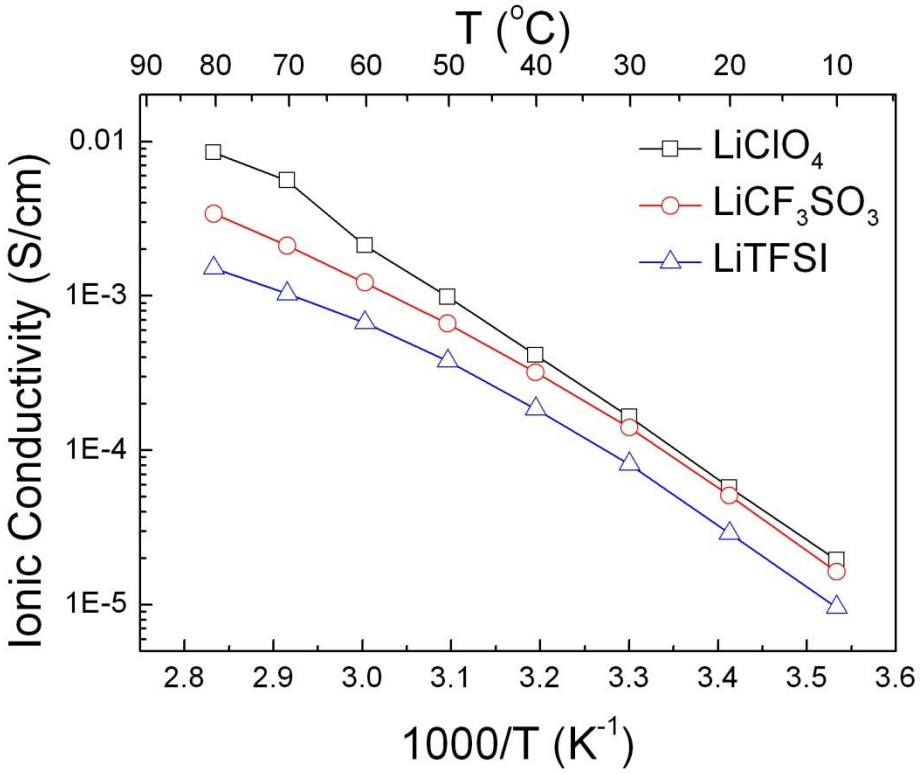

Figure 4.21. (a) Ionic conductivity and (b) lithium transference number of BCP-Si-B 30 containing $LiClO_4$, $LiCF_3SO_3$, and LiTFSI.

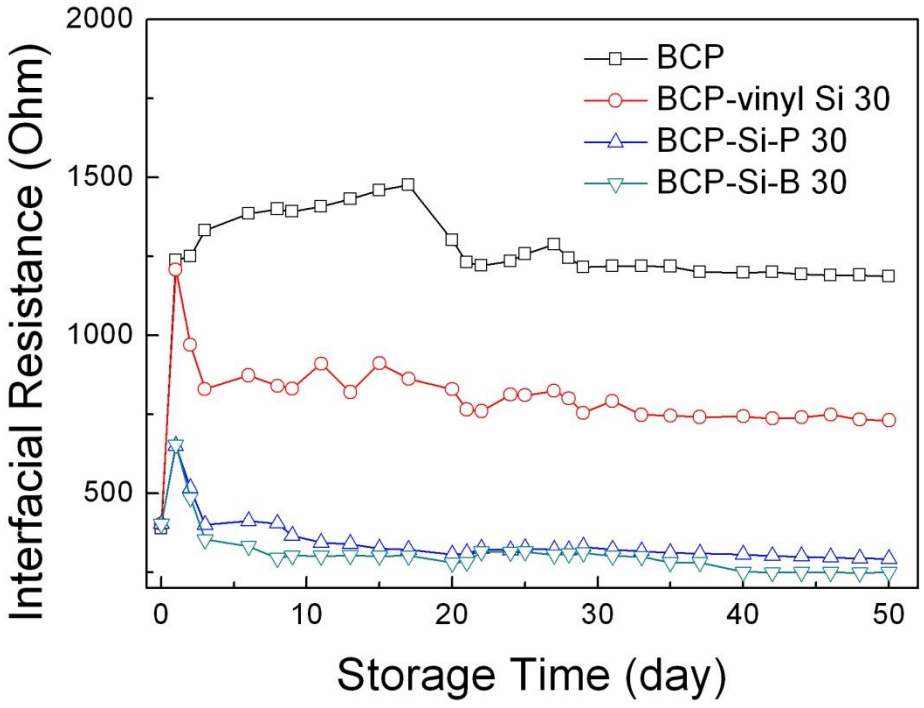

Figure 4.22. Interfacial resistances of symmetrically assembled Li/electrolyte/Li coin cells stored under open-circuit condition at 60 ^{o}C as a function of storage time, where BCP and the polymer composite electrolytes having 30 wt% of fillers (BCP-vinyl Si 30, BCP-Si-P 30, and BCP-Si-B 30) were used as electrolytes.

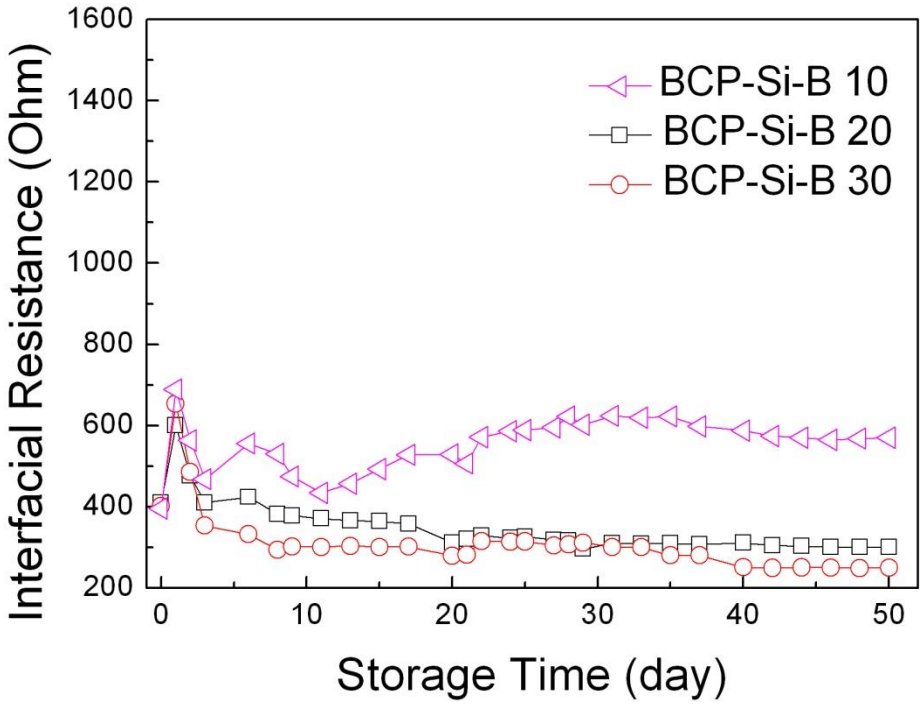

Figure 4.23. Interfacial resistances of symmetrically assembled Li/electrolyte/Li coin cells stored under open-circuit condition at 60 ^{o}C as a function of storage time, where BCP-Si-B having different amount of Si-B was used as electrolytes.

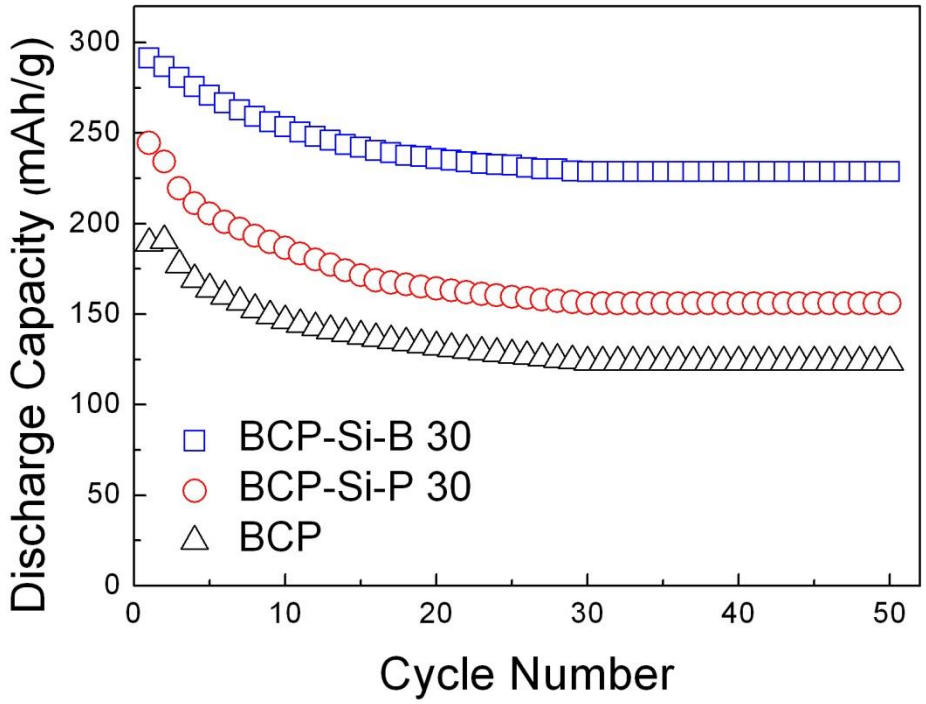

Figure 4.24. Discharge capacity profiles of all-solid-state Li/SPEs/V_2O_5 cell cycled at 60 ^oC with a scan rate of 0.1 C, where the SPEs are BCP and and the polymer composite electrolytes containing 30 wt% of fillers (BCP-Si-B 30 and BCP-Si-P 30).

Chapter 5

Gel Polymer Electrolyte Containing 2D Boron Nitride Nanoflakes as a Multifunctional Additive for Safe Lithium Metal Batteries

5.1. Introduction

Lithium metal batteries (LMBs), which utilize metallic lithium (Li) as the anode, have received considerable attention as an attractive alternative to conventional lithium-ion batteries (LIBs) for meeting the requirements of electric vehicles and energy storage systems.[1, 2] Li metal, as the lightest metal among all the metallic elements, possesses the highest theoretical specific capacity (3860 mAh g^{-1}) and the lowest redox potential (–3.04 V *vs.* the standard hydrogen electrode) to achieve high energy density and high voltage batteries.[2] Moreover, Li metal anode enables the use of high capacity, unlithiated cathode materials such as sulfur and oxygen as well as the elimination of the current collectors in conventional anodes.[1-3] However, practical applications of LMBs are currently limited by the uncontrolled formation and growth of Li dendrites during repeated charge/discharge cycles, which lead to short cycle life and serious safety issues including internal short circuits and thermal runaway of the batteries.[3]

To control the Li dendrites, different strategies such as *in situ* formation of stable solid-electrolyte interphase (SEI) layers[4, 5] or self-healing electrostatic shield[6] by electrolyte additives, *ex situ* protective coating

of the Li anode[7, 8], and application of solid electrolytes with high modulus and high Li^+ transference number (t_{Li+})[9, 10] have been investigated over the years. In general, there are two main theoretical frameworks for understanding the suppression of Li dendrites. One model by Chazalviel *et. al.* suggests that higher ionic conductivity and higher t_{Li+} of electrolytes can restrain the nucleation of Li dendrites by mitigating anion depletion-induced large electric fields near the Li electrode.[11] The other is the Monroe and Newman model that describes the suppression of Li dendrite growth by mechanical blocking using electrolytes with high shear modulus about twice that of the Li metal.[12] Based on these theoretical frameworks, the use of solid electrolytes with high modulus and high t_{Li+} is considered as one of the most promising approaches. However, the solid electrolytes have intrinsic drawbacks for practical applications, such as insufficient ionic conductivities at room temperature for solid polymer electrolytes and difficult fabrication and handling processes for solid ceramic electrolytes.[13] While gel polymer electrolytes (GPEs) are suitable to resolve these issues by taking advantages of their ease of fabrication, high ionic conductivity, and excellent electrochemical performance, there have been only a few reports concerning Li dendrite suppression

by GPEs.[14-18] In order to utilize the GPEs for LMB applications, their ionic conductivity and mechanical modulus have been further improved by introducing inorganic fillers, such as SiO_2, Al_2O_3, and TiO_2.[18, 19] However, in most cases, a large amount of fillers were required to mechanically block the Li dendrite growth, while also sacrificing the ionic conductivity.[15] To the best of our knowledge, there has been no published paper that demonstrates the fabrication of Li dendrite-suppressing GPEs with all the desirable properties of high ionic conductivity, high t_{Li+}, and high shear modulus *via* small addition (< 1 wt%) of inorganic fillers.

Recently, 2D nanomaterials, such as graphene and graphene analogues, have been studied extensively for a wide range of applications, due to their attractive properties originating from the ultrathin structure with a high degree of anisotropy and chemical functionality.[20, 21] Especially, the large enhancement of physical and chemical properties of diverse composites has been reported even with slight addition of the 2D nanomaterials as a functional nanofiller, which is ascribed to their large surface area providing efficient interfacial interactions with the polymer matrices.[22] Few layered hexagonal boron nitride (BN), as one of the graphene analogues, not only shares common properties with

it, such as high mechanical strength and thermal conductivity, but also exhibits other interesting properties owing to its unique structural features.[23] In contrast to the C-C bonds of graphene, the B-N bonds of BN show partially ionic character; the higher electronegativity of N atoms makes the lone pair electrons in the N p_z orbital only partially delocalized with the empty B p_z orbital and electron pairs in sp^2-hybridized B-N bonds are also more confined to the N atoms.[20, 23] These characteristics lead to the intrinsic electrically insulating property and superior thermal and electrochemical stability of the BN,[20, 23] which are prerequisites for the electrolyte applications. In addition, the BN possesses a large amount of electron-deficient B atoms to interact with Lewis bases,[24-26] also making it an attractive candidate for GPE additives to increase the t_{Li+} by trapping the anions of electrolytes, although this feature has not yet been fully elucidated in the literature.

There have been a few reports on the battery applications of the BN, presenting its use in ionic liquid-based composite electrolytes[27, 28] and stable coating layers on Li metal anode[29, 30] and separator[31], but its remarkable ability for suppressing the Li dendrites as a GPE additive has not been previously explored. Here, we report for the first

time a simple and effective strategy to prepare a Li dendrite-suppressing GPE using perfluoropolyether (PFPE)-functionalized 2D BN nanoflakes (BNNFs) as a multifunctional additive. It is demonstrated that even a minimal addition (0.5 wt%) of the PFPE-functionalized BNNFs into the GPE can provide an unprecedented combination of high ionic conductivity, high t_{Li+}, and high mechanical modulus, which all contribute to the effective suppression of Li dendrites for LMBs with excellent electrochemical and safety performance.

5.2. Experimental

5.2.1. Materials

Krytox® acid ($F(CF(CF_3)CF_2O)_nCF(CF_3)COOH$, n=14.1) was received from Dupont. Hexagonal boron nitride (BN, MK-hBN-N70, Lower Friction), poly(vinylidene fluoride-*co*-hexafluoropropylene) (PVH) (90 mol% of vinylidene fluoride and 10 mol% of hexafluoropropylene, average M_n = 110,000 g mol^{-1}, M_w = 455,000 g mol^{-1}), 1-pyrenemethanol, and thionyl chloride were purchased from

Aldrich and used as received. Methyl nonafluorobutyl ether were purchased from TCI and stored over 3 Å molecular sieves prior to use. 1.0 M lithium bis(trifluoromethane sulfonyl)imide (LiTFSI) in a mixture of ethylene carbonate (EC) and diethylene carbonate (DEC) (1:1 vol%) was purchased from PANAXETEC. Co., Ltd. Microporous polyolefin membrane (Celgard, 25 μm thickness, PE/PP/PE trilayer, Celgard® 2325) was obtained from Celgard, LLC and used for comparison purposes. All other reagents and solvents were obtained from reliable commercial sources and used as received.

5.2.2. Synthesis of pyrene with a perfluoropolyether chain (PFPE-Pyrene)

Krytox® acid (5.0 g, 2.0 mmol) was dissolved in 20 mL of methyl nonafluorobutyl ether and the resultant solution was added to a 100 mL of two-neck round bottomed flask equipped with a condenser and a magnetic stirring bar. The solution was heated at 60 ^{o}C for 1 h in an oil bath under nitrogen atmosphere. Thionyl chloride (0.48 g, 4.0 mmol) and pyridine (0.079 g, 1.0 mmol) were added to the solution and stirred for 16 h. To obtain the product, the resultant salt was

removed by vacuum filtration and the excessive thionyl chloride was evaporated at 60 ^{o}C under vacuum using rotary evaporator. After further dried under vacuum at room temperature for 24 h, the Krytox® acid with acyl chloride functional group (3.0 g, 1.2 mmol) in 7 mL of methyl nonafluorobutyl ether was added to a 50 mL of two-neck round bottomed flask equipped with a condenser and a magnetic stirring bar. 1-Pyrenemethanol (0.33 g, 1.43 mmol) in 7 mL of chloroform was then added to the flask by a syringe, followed by the addition pyridine (0.094 g, 1.2 mmol). The reaction mixture was stirred at 60 ^{o}C for 20 h under nitrogen atmosphere. The residual solvents were removed by evaporation, and the crude product was precipitated in methanol several times. After being dried under vacuum at room temperature for 24 h, bright yellowish oil was obtained with 58 % yield.

5.2.3. Preparation of boron nitride nanoflaskes noncovalentely functionalized with PFPE-Pyrene (FBN)

BN (0.1 g) and PFPE-Pyrene (0.1 g) were sonicated in 100 mL of methyl nonafluorobutyl ether for 10 h. The dispersed mixture was

centrifuged at 3000 rpm for 15 min three times and the supernant was collected. After the residual solvent was removed by evaporation, slightly yellow powder was obtained with 5 % of yield.

5.2.4. Preparation of composite gel polymer electrolytes (GPEs)

FBN was added to 10 wt% of PVH in acetone and the mixture was sonicated for 3 h. The amount of FBN was controlled as 0.1, 0.2, 0.5, and 1.0 wt% of the PVH. The dispersion was cast onto a glass plate using a doctor blade and dried at ambient condition. The obtained membrane was peeled from the glass plate and further dried at 60 ^{o}C under high vacuum for several days. The membrane was then immersed in 1.0 M LiTFSI in EC:DEC (1:1 vol%) for 24 h inside a glove box to prepare gel polymer electrolyte.

5.2.5. Cell fabrication and electrochemical characterization

The ionic conductivities of GPEs at 25 ^{o}C were determined using complex impedance spectroscopy with a Zahner Electrik IM6

apparatus in the frequency range of 0.1 Hz to 1.0 MHz with 10 mV of AC amplitude. The samples for the measurements were prepared by sandwiching the GPEs between two stainless-steel electrodes in a 2032 coin cell. The ionic conductivity (σ) was calculated from the following equation (2):

$$\sigma = (1/R) \times (d/A) \quad (2)$$

where R is electrolyte resistance obtained from the impedance spectrum, d is the thickness of electrolyte, and A is the area of the electrode. Li^+ transference number ($t$$Li^+$) was determined by DC polarization/AC impedance combination method at 25 ^oC. The GPEs were sandwiched between two non-blocking lithium metal disks to form a symmetrical Li/GPE/Li in 2032 coin cell. The cell was polarized by a constant DC voltage of 10 mV and following current values were monitored until steady-state current was observed. The initial and steady-state resistances of the cell were also measured. From this method, $t$$Li^+$ was determined by the following equation (3):

$$t\mathrm{Li}^+ = [I_s \times (V - I_i \times R_i)] / [I_i \times (V - I_s \times R_s)] \quad (3)$$

where V is constant DC voltage applied to the cell and R_i and R_s are initial and steady-state resistances, respectively. I_i and I_s are initial and steady-state currents, respectively. Glavanostatic charge/discharge test was carried out to evaluate dendrite-suppressing behavior at 25 ^oC. Time evolution of voltage profiles was measrured on a symmetric lithium cell during repetitive charge/discharge cycles, where the cell was cycled under constant current density of 1.0 mA cm^{-2} and the polarity was reversed for every 3 h. Charge/discharge cycling test of lithium metal battery was performed with WBCS3000 battery cycler (WonATech). $LiFePO_4$ (80 wt%, LG Chem, Ltd) was used as cathode active materials and dispersed in *N*-methyl-2-pyrrolidone (NMP) with carbon black (10 wt%) and PVdF (10 wt%). The resultant slurry was deposited and cast onto an aluminium current collector using a doctor blade. The residual NMP was completely removed under vacuum condition at 120 ^oC for 24 h. The obtained cathode sheet, lithium metal, and GPE were punched into disk shapes and assembled together in 2032 coin cell to form Li/GPE/$LiFePO_4$ cell. All components were assembled in argon filled glove box (H_2O < 0.5 ppm, O_2 < 0.5 ppm). Charge/discharge cycling test of the lithium metal

battery was performed at cutoff voltages of 2.5–4.2 V *vs.* Li/Li^+ at 25 ^oC with C-rates of 1.0 C and 10 C, where the 1.0 C rate corresponds to a current density of 170 mA g^{-1}. Rate capability of $Li/GPE/LiFePO_4$ cell was also tested at the same cutoff voltages at 25 ^oC by varying the current densities.

5.2.6. Characterization

^{19}F NMR spectra were recorded on a JeolJNM-LA400 spectrometer (400 MHz) with LFG. $CDCl_3$ (containing TMS as a reference, Cambridge Isotope Laboratories), mixed with methyl nonafluorobutyl ether, was used as a solvent. The Fourier transform infrared (FT-IR) spectra were recorded in the absorption mode on Nicolet 6700 spectrophotometer with a resolution of 4 cm^{-1} in the vibrational frequency range from 400 to 4000 cm^{-1}. Field-emission scanning electron microscopy (FE-SEM) was performed on a JEOL JSM-6700F with an accelerating voltage of 10 kV. Transmission electron microscopy (TEM) was performed on a LIBRA 120 with an accelerating voltage of 120 kV. TEM specimens were prepared by drop casting of 0.1 wt % dispersion in acetone on carbon-coated grid.

The morphology of FBN was observed using atomic force microscopy (AFM, Asylum Research MFP-3D) in tapping-mode under ambient condition. The X-ray diffraction (XRD) spectra were obtained using Rigaku SmartLab (Cu Kα) spectrometers. Raman spectra were collected on a T64000 Triple Raman spectrometer (HORIBA) equipped with a 532 nm Ar laser source. The mechanical properties were measured using a universal testing machine (UTM, LS1SC, LLOYD Instruments). UTM specimens were prepared following the ASTM standard D638 (Type V specimens dog-bone shaped samples). The tensile properties of the membrane samples were measured with a gauge length and cross head speed of 15 mm and 5 mm min^{-1}, respectively. At least five specimens for each sample were tested and their average values were used. The amount of liquid electrolyte uptake was determined by measuring their changes in weight before and after immersion in the liquid electrolyte for 24 h. The electrolyte uptake value is calculated as follows:

$$\text{Electrolyte uptake (\%)} = [(W_{wet} - W_{dry})/W_{dry}] \times 100 \quad (1)$$

where W_{dry} and W_{wet} is the weight of membrane before and after

immersion in liquid electrolyte, respectively.

5.3. Results and Discussion

In order to increase the surface area and compatibility with P(VdF-*co*-HFP) (PVH) GPE matrix, PFPE-functionalized BNNFs (FBN) were prepared *via* sonication-assisted exfoliation and noncovalent functionalization of nano-sized BN powder by PFPE-functionalized pyrene (PFPE-Pyrene) molecules. PFPE-Pyrene was synthesized by esterification between PFPE-COOH and 1-pyrenemethanol as shown in Figure 5.1. Carboxylic acid group of PFPE-COOH was activated by thionyl chloride and subsequently reacted with 1-pyrenemethanol. The structure of products in each step was characterized by FT-IR spectroscopy (Figure 5.2). The wavenumbers of carbonyl (C=O) peaks of PFPE-COOH, PFPE-COCl, and PFPE-Pyrene are slightly changed as the reaction proceeds, indicating the successful conversion. Furthermore, PFPE-Pyrene has C=C strecthing peaks from aromatic pyrene moieties. Figure 5.3 shows ^{19}F NMR spectra of PFPE-COOH, PFPE-COCl, and PFPE-Pyrene. PFPE-COOH has a peak at -132 ppm that is associated with a fluorine atom adjacent to the carbonyl group.

This fluorine peak is shifted as the reaction proceeds (-126 ppm and -133 ppm for PFPE-COCl and PFPE-Pyrene, respectively).

FBN was prepared *via* sonication-assisted exfoliation and noncovalent functionalization of BN powder by PFPE-Pyrene as shown in Figure 5.4. Stacked BN layers are exfoliated during the sonication process and the electron-deficient BN surface is noncovalently functionalized by electron-rich PFPE-pyrene at the same time. Nano-sized BN was used for the preparation of FBN as shown in Figure 5.5 to utilize its large surface area and good dispersion behavior in the polymer matrix. The exfoliation state of FBN was confirmed by AFM and HR-TEM analyses. As shown in Figure 5.6(a), the thickness of FBN is about 3–4 nm that is much decreased from that of pristine BN (40-60 nm), indicating that pristine BN layers are exfoliated during the sonication-assisted noncovalent functionalization. As shown in HR-TEM image in Figure 5.6(b), several fringes were observed at folded edges of FBN layers and their thicknesses are in the range of 3–4 nm on average, indicating that FBN has exfoliated 9–12 BN layers, as also estimated from the AFM result. Figure 5.7 shows TEM images and electron energy loss spectra of BN and FBN. Both BN and FBN have B and N signals from the

BN. In addition, FBN has O and F signals from PFPE chains, indicating the successful noncovalent functionalization. Since the amount of PFPE chains in the FBN is relatively small compared to that of BN in the FBN, thick, aggregated FBN layers were intentionally chosen for the analysis (Figure 5.7(b)). Figure 5.8 shows Raman spectra of BN, FBN, and PFPE-Pyrene. The band at 1367 cm^{-1} indicates E_{2g} phonon mode of B-N, which appears in both BN and FBN spectra. In the case of FBN, Raman bands from PFPE chain are also observed, indicating that PFPE chains were successfully attached to the BN surface. The bands at 1067/1072 cm^{-1} and 1299 cm^{-1} correspond to symmetric CF_2 and CF_3 strecthing modes of PFPE chain, respectively. The two bands at 1400 and 1610 cm^{-1} are attributed to the aromatic C=C stretching mode of pyrene moieties. The TGA profiles in Figure 5.9 provide additional information on FBN composition. BN shows good thermal stability without any weight loss up to 700 ^{o}C, while the weight of FBN continuously decreases due to the decomposition of PFPE-pyrene which is noncovalently attached to the BN. The final weigtht loss of FBN at 700 ^{o}C is found to be about 4.7 wt%. Since the non-zero char yield of PFPE-pyrene at 700 ^{o}C is ascribed to the presence of aromartic pyrene moieties, it can

be estimated that the amount of noncovalently attached PFPE-pyrene is slightly larger than 4.7 wt%.

Composite membranes (CFBNs) were fabricated *via* simple blade casting of the mixture of PVH and FBN in acetone on a glass plate, wherein the FBN content was controlled as 0.1, 0.2, 0.5, and 1.0 wt% of the PVH (Figure 5.10). After dried at ambient condition and subsequently under vacuum at 60 ^{o}C, large area, porous CFBNs with thickness of 6–9 μm could be obtained, which were further immersed in liquid electrolyte (1M LiTFSI in EC:DEC (1:1 vol%)) to prepare GPEs (G-CFBNs) (Figure 5.10(a)-5.10(c)). It is worth noting that the porous structure of CFBNs is automatically generated during the membrane fabrication process without the addition of any porogen or non-solvent. This should be ascribed to the different compatibility of FBN with the PVH matrix and the acetone solvent (Figure 5.10(d)). The PVH is fully soluble in acetone, while the FBN having very hydrophobic PFPE chains is not soluble and even cannot be dispersed in acetone. However, when the FBN was mixed with PVH, FBN was found to maintain its dispersity in acetone for 1 h (Figure 5.11), indicating that there is partial miscibility between the PVH and the PFPE chains in FBN, possibly because they are all fluorinated

polymers. The partial miscibility behaviours between the fluorinated polymers were reported by others before.[32] This delicate increase of the miscibility of FBN in acetone solution containing PVH can produce the more or less homogeneous solution for the casting process, while the autonomous phase separation between PVH matrix containing acetone insoluble FBN can produce the porous structure during the membrane casting process. It is well known that the porous structures in the membrane can be easily prepared in the casting process using the phase separation behaviour between the molecules.[33, 34] Although other porous membranes were induced by the non-solvent effect, it would be postulated that non-soluble filler can also induce the phase separation forming the porous structures. Therefore, when PVH membranes were prepared without FBN, only dense membrane without any pores were obtained, while when the content of FBN was increased, the pore size of the porous CFBNs gradually increases possibly due to the increasing phase separation between the FBN/PVH and the acetone (Figure 5.12).

We investigated the multifunctional properties of FBN in G-CFBN by analysing the electrochemical and mechanical properties of G-CFBN, PVH-based GPE without FBN (G-PVH), and liquid

electrolyte/separator (LE-Celgard) (Figure 5.13). The content of FBN in G-CFBN was fixed as 0.5 wt% of the PVH matrix, which exhibits the highest ionic conductivity (Figure 5.14). The ionic conductivity of G-CFBN increases as the FBN content increases from 0 wt% (G-PVH) to 0.5 wt%, due to the increase of electrolyte uptake. The incorporation of FBN into PVH matrix facilitates the electrolyte uptake by eliminating the crystallinity of the PVH as well as generating the porous structure (Figure 5.12 and Figure 5.15).[15] The subsequent decrease in electrolyte uptake of G-CFBN, with the FBN content higher than 0.5 wt%, is found to decrease the ionic conductivity. This could be attributed to the presence of crystallinity of the PVH matrix limiting the effective electrolyte uptake at a FBN content of 1.0 wt% (Figure 5.15),[15, 35] which originates from the inhomogeneous dispersion of excess FBN.[35] The ionic conductivity of G-CFBN is thus limited by the marginal content of FBN (0.5 wt%), however, it should be noted that its optimum ionic conductivity is about twice higher than that of the conventional LE-Celgard (Figure 5.16(a)). Meanwhile, a GPE (G-CBN), prepared from PVH and incompatible pristine BN (0.5 wt%), shows the crystallinity of the PVH matrix and a dense film structure without pores, which

significantly suppress the electrolyte uptake and thereby lead to much lower ionic conductivity as compared to the G-CFBN (Figure 5.17 and Figure 5.18).

The anion-trapping ability of FBN was evaluated by measuring the t_{Li+} of G-CFBN, G-PVH, and LE-Celgard, using DC polarization/AC impedance combination method (Figure 5.16(a) and Figure 5.19). As the fluoropolymer chains in G-PVH can interact with anions in the electrolyte by utilizing their high dielectric constant (11.38) and electron-withdrawing functional groups, the G-PVH without the FBN already exhibits larger t_{Li+} value than the LE-Celgard.[36, 37] While the anion-trapping ability of BN in electrolytes has not yet been reported, the surface functionalization of BN by the interaction between electron-deficient B atoms in BN and Lewis bases has been reported previously.[25, 26] The t_{Li+} value of G-CFBN (0.62) higher than that of the G-PVH (0.41) clearly demonstrates that the FBN in G-CFBN still can work as a Lewis acid to trap the anions of the electrolyte, although the empty B p_z orbital is partially filled with delocalized lone pair electrons in the N p_z orbital.[20, 25] The anion-trapping behaviour of FBN in G-CFBN could be further supported by Raman spectroscopy of the GPEs (Figure 5.20). The content of Li^+-

uncoordinated $TFSI^-$, corresponding to the band at 742 cm^{-1}, in G-CFBN is found to be higher than that in G-PVH, which indicates that the FBN interacts with the $TFSI^-$ and thus dissociates it from the Li^+-coordinated state.[38] Such interaction between the FBN and $TFSI^-$ also contributes to the wider electrochemical stability window of G-CFBN than the G-PVH by lowering the extent of anion oxidation at high potential (Figure 5.21).[38, 39] Therefore, with the small content of FBN, the G-CFBN exhibits much improved overall electrochemical properties including the ionic conductivity and t_{Li+}, which are important in controlling the Li dendrite formation by alleviating the anion depletion-induced large electric fields near the Li anode.[11]

2D nanomaterials are known to have the effective reinforcement ability in the composites *via* efficient interfacial interactions with polymer matrices using their large surface area.[22, 23] The slight incorporation of FBN into the PVH matrix also significantly enhances the mechanical strength (Figure 5.16(b)). Young's modulus (110 GPa) and tensile strength (53 MPa) of CFBN, analysed by universal testing machine (UTM), are 4.4 and 3.2 times larger than those of PVH, respectively (Figure 5.22). In addition, the Young's modulus of the CFBN is 70 times higher than that of the Celgard, while their tensile

strengths are close to each other. Theoretically, high shear modulus (G) of GPEs, larger than 7 GPa, is considered as an important physical parameter for impeding the Li dendrite growth.[12] The G of the CFBN can be estimated from the equation, $G = E/[2(1 + v)]$, where E and v are the Young's modulus and Poisson's ratio, respectively.[40] Since the v typically ranges from –1 to 0.5,[40] the CFBN should possess G higher than at least 36.7 GPa. The E values of GPEs after the equilibrated uptake of liquid electrolyte could not be measured by the UTM due to the excessively slippery surfaces. However, it might be informative that we could obtain 27.4 GPa of E for the G-CFBN from repeated measurements when the electrolyte uptake was intentionally limited to about 60 % by controlling the uptake time (Figure 5.23). Thus, the G-CFBN as a GPE could provide a large mechanical modulus for suppressing the Li dendrite growth.

Based on the largely enhanced ionic conductivity, t_{Li+}, and mechanical modulus of G-CFBN, we performed galvanostatic Li plating/stripping cycling tests on symmetric Li/Li cells with G-PVH, G-CFBN, and LE-Celgard at a high current density of 1 mA cm^{-2} (Figure 5.16(c)). The Li/G-PVH(11 μm thickness)/Li cell shows a short circuit induced by Li dendrite growth, which is characterized by

the sharp rise in voltage hysteresis with the cycle time and the sudden drop after 178 h. The short circuit time of the Li/G-PVH/Li cell is shorter than that of Li/LE-Celgard/Li cell even when the G-PVH (24 μm) has similar thickness with the Celgard (25 μm) (Figure 5.24), because the non-porous structure and crystallinity of the PVH could cause limited, inhomogeneous electrolyte uptake, resulting in the facilitated Li dendrite growth by non-uniform Li^+ flux near the Li anode.[41] However, the Li/Li cell with G-CFBN of much thinner thickness (8 μm), exhibits a much smaller overpotential in the voltage hysteresis and longer cycling stability over 1940 h without a short circuit than those with G-PVH and LE-Celgard, which should be attributed to all the desirable properties of high ionic conductivity, high t_{Li+}, and large mechanical modulus of the G-CFBN. The excellent compatibility between the G-CFBN and Li electrode is also supported by the smooth Li electrode surface morphology after the short circuit (Figure 5.25).[15, 16] Despite extensive efforts *via* various strategies, the Li dendrite suppression, especially at high current densities (>1 mA cm^{-2}), still remains a challenge.[42] As compared with representative results across recently published studies, the G-CFBN clearly exhibits comparable or somewhat superior Li dendrite-

suppressing ability at a high current density of 1 mA cm^{-2} (Figure 5.16(d) and Table 5.1 for details). Therefore, it is shown here that a promising GPE for dendrite-free LMBs can be prepared *via* a simple and effective approach of utilizing 2D BNNFs as a multifunctional additive.

We further evaluated the practical applicability of G-CFBN in LMBs using a Li metal anode and a $LiFePO_4$ (LFP) cathode. The Li/G-CFBN/LFP cell shows superior rate capability in comparison with the Li/LE-Celgard/LFP cell especially at a high C-rate of 5.0 C (Figure 5.26(a) and Figure 5.27), mainly due to the higher ionic conductivity and t_{Li+} of the G-CFBN than those of the LE-Celgard (Figure 5.16(a)).[38] As shown in the long-term cycling performance at 1.0 C (Figure 5.26(b) and Figure 5.28), the cell with G-CFBN also exhibits higher capacity retention (88 %) than that with LE-Celgard (74 %) after 300 cycles. In addition, overpotential values of the Li/G-CFBN/LFP cell are much smaller than those of Li/LE-Celgard/LFP cell in voltage–capacity profiles (Figure 5.28), indicating that problematic electrode polarization is significantly suppressed by the G-CFBN. Upon disassembling the cells after the cycling, Li metal surface in the cell with G-CFBN shows somewhat porous but smooth

morphology, while that in the cell with LE-Celgard shows noticeable large cracks and pinholes with roughness (Figure 5.29), demonstrating that the dendrite growth is much suppressed by the G-CFBN compared to the LE-Celgard. This should be attributed to the synergistic combination of superior mechanical modulus[40] and excellent electrochemical properties[16, 42] of the G-CFBN. The controlled Li plating/stripping behaviour eventually leads to the formation of stable SEI layer and thereby achieves better long-term cycling performance.[42] The more stable SEI formation for the cell with the G-CFBN is further verified from the electrochemical impedance spectroscopy (EIS) of each cell before and after cycling (Figure 5.30), presenting smaller interfacial resistance ($R_{int} = R_{SEI} + R_{ct}$) values of the Li/G-CFBN/LFP cell as compared to the Li/LE-Celgard/LFP cell. Moreover, it is noteworthy that the Li/G-CFBN/LFP cell exhibits outstanding cycling performance over 500 cycles even when the C-rate reaches 10 C (Figure 5.26(c) and Figure 5.31); to our knowledge, this can be considered as an unprecedented high-rate long-term cycling performance compared with other reports in the literature There have been a few reports on the LMBs operated under high C-rates over 10 C. Such reports are summarized in Table 5.2, but it is

very difficult to evaluate their cycle performance precisely because the cells in the literature were not operated over 20 cycles. In our case, capacity is retained as 96 % and 82 % even after 200 and 500 cycles, respectively. To the best of our knowledge, this is the longest operation of LMB with great capacity retention at 10 C rate ever reported. In contrast, the Li/LE-Celgard/LFP cell exhibits very poor cycling performance at 10 C (Figure 5.32). The outstanding long-term cycling stability at high C-rates, combined with intrinsic good thermal stability of the CFBN matrix (Figure 5.33), can eventually lead to realization of safe, long cycle life and high rate LMBs with the G-CFBN.

5.4. Conclusions

In summary, we have demonstrated that the PFPE-functionalized 2D BNNFs (FBN) additive can provide multifunctional properties to a PVH-based GPE for LMB applications. Even with the marginal content of FBN, the GPE containing FBN (G-CFBN) exhibits greatly enhanced overall physical properties, including ionic conductivity, t_{Li+}, and mechanical modulus. Such high ionic conductivity, high t_{Li+}, and

high mechanical modulus make the G-CFBN strongly resistant against the Li dendrite formation and growth by providing both alleviated Li^+ concentration gradient and mechanically robust blocking layer. The G-CFBN in symmetric Li/Li cells shows unprecedentedly long short circuit time of 1940 h at a high current density of 1 mA cm^{-2}. The G-CFBN also works efficiently in Li/LFP batteries, where they can be reversibly cycled maintaining high discharge capacity for more than 500 cycles, even at a high 10 C rate. We believe that the present work provides insight into the design and preparation of dendrite-suppressing GPEs for LMB applications including next-generation Li/S and Li/Air batteries, by taking advantages of the multifunctional properties of 2D BNNFs. In particular, the Lewis acidity of BNNFs in GPEs could exhibit additional polysulfide trapping ability for controlling the polysulfide dissolution in Li/S batteries; such studies are underway.

5.5. References

[1] K. Zhang, G. H. Lee, M. Park, W. J. Li and Y. M. Kang, *Adv. Energy Mater.* **2016**, *6*, 1600811.

[2] W. Xu, J. L. Wang, F. Ding, X. L. Chen, E. Nasybutin, Y. H. Zhang and J. G. Zhang, *Energy Environ. Sci.* **2014**, *7*, 513-537.

[3] D. Lin, Y. Liu, Y. Cui, *Nat. Nano* **2017**, *12*, 194-206.

[4] Y. Lu, Z. Tu and L. A. Archer, *Nat. Mater.* **2014**, *13*, 961-969.

[5] S. Choudhury and L. A. Archer, *Adv. Electron. Mater.* **2016**, *2*, 1500246.

[6] F. Ding, W. Xu, G. L. Graff, J. Zhang, M. L. Sushko, X. Chen, Y. Shao, M. H. Engelhard, Z. Nie, J. Xiao, X. Liu, P. V. Sushko, J. Liu and J.-G. Zhang, *J. Am. Chem. Soc.* **2013**, *135*, 4450-4456.

[7] E. Kazyak, K. N. Wood and N. P. Dasgupta, *Chem. Mater.* **2015**, *27*, 6457-6462.

[8] D. C. Lin, Y. Y. Liu, Z. Liang, H. W. Lee, J. Sun, H. T. Wang, K. Yan, J. Xie and Y. Cui, *Nat. Nanotechnol.* **2016**, *11*, 626-632.

[9] S. O. Tung, S. Ho, M. Yang, R. L. Zhang and N. A. Kotov, *Nat. Commun.* **2015**, *6*, 6152.

[10] Q. W. Pan, D. M. Smith, H. Qi, S. J. Wang and C. Y. Li, *Adv. Mater.* **2015**, *27*, 5995-6001.

[11] J. N. Chazalviel, *Phys. Rev. A* **1990**, *42*, 7355-7367.

[12] C. Monroe and J. Newman, *J. Electrochem. Soc.* **2005**, *152*, A396-A404.

[13] A. Varzi, R. Raccichini, S. Passerini and B. Scrosati, *J. Mater. Chem. A* **2016**, *4*, 17251-17259.

[14] Q. Lu, Y.-B. He, Q. Yu, B. Li, Y. V. Kaneti, Y. Yao, F. Kang and Q.-H. Yang, *Adv. Mater.* **2017**, 1604460.

[15] H. T. T. Le, D. T. Ngo, R. S. Kalubarme, G. Cao, C.-N. Park and C.-J. Park, *ACS Appl. Mater. Interfaces* **2016**, *8*, 20710-20719.

[16] D. Zhou, R. L. Liu, Y. B. He, F. Y. Li, M. Liu, B. H. Li, Q. H. Yang, Q. Cai and F. Y. Kang, *Adv. Energy Mater.* **2016**, *6*, 1502214.

[17] Y. S. Zhu, S. Y. Xiao, Y. Shi, Y. Q. Yang, Y. Y. Hou and Y. P. Wu, *Adv. Energy Mater.* **2014**, *4*, 1300647.

[18] S. Choudhury, R. Mangal, A. Agrawal and L. A. Archer, *Nat. Commun.* **2015**, *6*, 10101.

[19] L. Long, S. Wang, M. Xiao and Y. Meng, *J. Mater. Chem. A* **2016**, *4*, 10038-10069.

[20] Q. H. Weng, X. B. Wang, X. Wang, Y. Bando and D. Golberg, *Chem. Soc. Rev.* **2016**, *45*, 3989-4012.

[21] K. S. Novoselov, V. I. Fal'ko, L. Colombo, P. R. Gellert, M. G. Schwab and K. Kim, *Nature* **2012**, *490*, 192-200.

[22] T. Kuilla, S. Bhadra, D. H. Yao, N. H. Kim, S. Bose and J. H. Lee, *Prog. Polym. Sci.* **2010**, *35*, 1350-1375.

[23] A. Pakdel, Y. Bando and D. Golberg, *Chem. Soc. Rev.* **2014**, *43*, 934-959.

[24] K. H. Oh, D. Lee, M. J. Choo, K. H. Park, S. Jeon, S. H. Hong, J. K. Park and J. W. Choi, *ACS Appl. Mater. Interfaces* **2014**, *6*, 7751-7758.

[25] S. Y. Xie, W. Wang, K. A. S. Fernando, X. Wang, Y. Lin and Y. P. Sun, *Chem. Commun.* **2005**, 3670-3672.

[26] Y. Lin, T. V. Williams and J. W. Connell, *J. Phys. Chem. Lett.* **2010**, *1*, 277-283.

[27] M. T. F. Rodrigues, K. Kalaga, H. Gullapalli, G. Babu, A. L. M. Reddy and P. M. Ajayan, *Adv. Energy Mater.* **2016**, *6*, 1600218.

[28] M. T. Li, W. S. Zhu, P. F. Zhang, Y. H. Chao, Q. He, B. L. Yang, H. M. Li, A. Borisevich and S. Dai, *Small* **2016**, *12*, 3535-3542.

[29] K. Yan, H. W. Lee, T. Gao, G. Y. Zheng, H. B. Yao, H. T. Wang, Z. D. Lu, Y. Zhou, Z. Liang, Z. F. Liu, S. Chu and Y. Cui, *Nano Lett.* **2014**, *14*, 6016-6022

[30] L. Shi, A. Xu and T. S. Zhao, *ACS Appl. Mater. Interfaces* **2017**, *9*, 1987-1994.

[31] W. Luo, L. H. Zhou, K. Fu, Z. Yang, J. Y. Wan, M. Manno, Y. G. Yao, H. L. Zhu, B. Yang and L. B. Hu, *Nano Lett.* **2015**, *15*, 6149-6154.

[32] M.-P. Gelin and B. Ameduri, *J. Polym. Sci. Part A. Polym. Chem*. **2003**, 41, 160-171.

[33] H.-S. Jeong, J. H. Kim and S.-Y. Lee, *J. Mater. Chem*. **2010**, 20, 9180-9186.

[34] H.-S. Jeong, J. H. Noh, C.-G. Hwang, S. H. Kim and S.-Y. Lee, *Macromol. Chem. Phys*. **2010**, 211, 420-425.

[35] Y. Zhu, F. Wang, L. Liu, S. Xiao, Z. Chang and Y. Wu, *Energy Environ. Sci.* **2013**, *6*, 618-624.

[36] C. S. Kim and S. M. Oh, *Electrochim. Acta* **2000**, *45*, 2101-2109.

[37] J. Shim, J. S. Lee, J. H. Lee, H. J. Kim and J. C. Lee, *ACS Appl. Mater. Interfaces* **2016**, *8*, 27740-27752.

[38] N.-S. Choi, S.-W. Ryu and J.-K. Park, *Electrochim. Acta* **2008**, *53*, 6575-6579.

[39] X. M. Hao, J. Zhu, X. Jiang, H. T. Wu, J. S. Qiao, W. Sun, Z. H. Wang and K. N. Sun, *Nano Lett.* **2016**, *16*, 2981-2987.

[40] X.-B. Cheng, T.-Z. Hou, R. Zhang, H.-J. Peng, C.-Z. Zhao, J.-Q. Huang and Q. Zhang, *Adv. Mater.* **2016**, *28*, 2888-2895.

[41] G. Y. Zheng, C. Wang, A. Pei, J. Lopez, F. F. Shi, Z. Chen, A. D. Sendek, H. W. Lee, Z. D. Lu, H. Schneider, M. M. Safont-Sempere, S. Chu, Z. N. Bao and Y. Cui, *ACS Energy Lett.* **2016**, *1*, 1247-1255.

Table 5.1. Summary of recent literature reports on galvanostatic cycling test.

Type	**Materials**	**Current density (mA cm^{-2})**	**Charge/ discharge time (h)**	**Temp. (^{o}C)**	**Short circuit time (h)**	**Ref.**
GPE	PVdF-HFP/FBN	1.0	3	25	1940	Present study
GPE /Separator	PVdF-HFP /A-LLTO/m-SiO_2	0.48	2	25	1922	S1
	PVdF-HFP /Epoxy resin	1.0	3	25	> 600	S2
	PVdF-HFP/ Nanoporous Al_2O_3/PVdF-HFP	0.2	3	25	> 1000	S3
	PVdF/Hollow SiO_2/ Crosslinked TPGDA	1.0	3	25	> 200	S4
	Silica/ PEO oligomer	1.0	3	25	> 100	S5

	Nanoporous Al_2O_3 membrane	1.0	1	25	> 1560	S6
	Poly(*p*-phenylene benzobisoxazole) nanofiber	0.38	3	25	> 700	S7
SPE	Crosslinked PEG-POSS	0.3 0.5 1.0	3	90	> 2600 1212 441	S8
	PEO/LLZO	0.5	0.5	25	> 1000	S9
	Crosslinked PE-PEO/PEG	0.26 0.4 0.7 1.0	3	90	275 96 50 27	S10
	PS-*b*-PEO	0.02	4	85	180	S11
Li coating /Additive	Li/Al_2O_3	1.0	0.25	25	> 600	S12
	Li/PI-ZnO	1.0	1	25	> 200	S13
	Li/PVdF/Nafion	1.1	1	25	> 200	S14

Li coating /Additive	Li/GO	0.5	3	25	7.5	S15
	Li/Kimwipe paper	2.0	3	25	> 1000	S16
	Li/Li_3PO_4	1.0	1	25	> 300	S17
	Li/rGO	1.0	1	25	> 222	S18
	Li/RTIL	1.0	0.25	25	> 190	S19
	Li/LiF	1.0	4	25	> 1750	S20

A-LLTO: Perovskite-structured aluminum-doped lithium lanthanum titanate; m-SiO2: modified SiO2, PEO: poly(ethylene oxide); TPGDA: tripropylene glycol diacrylate; POSS: polyhedral oligomeric silsesquioxane; LLZO: garnet-type $Li_{6.4}La_3Zr_2Al_{0.2}O_{12}$; PE: polyethylene; PS: polystyrene; RTIL: room-temperature ionic liquid

References for Table 5.1.

(S1) H. T. T. Le, D. T. Ngo, R. S. Kalubarme, G. Cao, C.-N. Park and C.-J. Park, *ACS Appl. Mater. Interfaces* 2016, **8**, 20710-20719.

(S2) Q. Lu, Y.-B. He, Q. Yu, B. Li, Y. V. Kaneti, Y. Yao, F. Kang and Q.-H. Yang, *Adv. Mater.* 2017, 1604460.

(S3) Z. Y. Tu, Y. Kambe, Y. Y. Lu and L. A. Archer, *Adv. Energy Mater.* 2014, **4**, 1300654.

(S4) D. Zhou, R. Liu, Y.-B. He, F. Li, M. Liu, B. Li, Q.-H. Yang, Q. Cai and F. Kang, *Adv. Energy Mater.* 2016, **6**, 1502214.

(S5) S. Choudhury, R. Mangal, A. Agrawal and L. A. Archer, *Nat. Commun.* 2015, **6**, 10101.

(S6) Z. Tu, M. J. Zachman, S. Choudhury, S. Wei, L. Ma, Y. Yang, L. F. Kourkoutis and L. A. Archer, *Adv. Energy Mater.* 2017, 1602367.

(S7) X. M. Hao, J. Zhu, X. Jiang, H. T. Wu, J. S. Qiao, W. Sun, Z. H. Wang and K. N. Sun, *Nano Lett.* 2016, **16**, 2981-2987.

(S8) Q. W. Pan, D. M. Smith, H. Qi, S. J. Wang and C. Y. Li, *Adv. Mater.* 2015, **27**, 5995-6001.

(S9) K. Fu, Y. H. Gong, J. Q. Dai, A. Gong, X. G. Han, Y. G. Yao, C. W. Wang, Y. B. Wang, Y. N. Chen, C. Y. Yan, Y. J. Li, E. D. Wachsman and L. B. Hu, *Proc. Natl. Acad. Sci. USA* 2016, **113**, 7094-7099.

(S10) Q. Zheng, L. Ma, R. Khurana, L. A. Archer and G. W. Coates, *Chem. Sci.* 2016, **7**, 6832-6838.

(S11) N. S. Schauser, K. J. Harry, D. Y. Parkinson, H. Watanabe and N. P. Balsara, *J. Electrochem. Soc.* 2015, **162**, A398-A405.

(S12) E. Kazyak, K. N. Wood and N. P. Dasgupta, *Chem. Mater.* 2015,

27, 6457-6462.

(S13) Y. Y. Liu, D. C. Lin, Z. Liang, J. Zhao, K. Yan and Y. Cui, *Nat. Commun.* 2016, **7**, 10992.

(S14) J. Luo, R.-C. Lee, J.-T. Jin, Y.-T. Weng, C.-C. Fang and N.-L. Wu, *Chem. Commun.* 2017, **53**, 963-966.

(S15) Y. J. Zhang, X. H. Xia, X. L. Wang, C. D. Gu and J. P. Tu, *RSC Adv.* 2016, **6**, 66161-66168.

(S16) C.-H. Chang, S.-H. Chung and A. Manthiram, *Adv. Sustainable Syst.* 2017, **1**, 1600034.

(S17) L. Wang, Q. Wang, W. Jia, S. Chen, P. Gao and J. Li, *J. Power Sources* 2017, **342**, 175-182.

(S18) D. Lin, Y. Liu, Z. Liang, H.-W. Lee, J. Sun, H. Wang, K. Yan, J. Xie and Y. Cui, *Nat. Nano* 2016, **11**, 626-632.

(S19) A. Basile, A. I. Bhatt and A. P. O'Mullane, *Nat. Commun.* 2016, **7**, 11794.

(S20) S. Choudhury and L. A. Archer, *Adv. Electron. Mater.* 2016, **2**, 1500246.

Table 5.2. Summary on cycle performance of LMBs containing GPE from recent literature reports.

Materials	**C-rate**	**Cycle number**	**Cathode (theoretical capacity)**	**Capacity retention (%)**	**Initial capacity /final capacity (mAh g^{-1})**	**Ref.**
PVdF-HFP/FBN	10 C	500	$LiFePO_4$ (170 mAh g^{-1})	82	100/82	Present study
Nonwoven PTFE/poly(methyl ethyl α-cyanoacrylate)	10 C	5	$LiNi_{0.5}Mn_{1.5}O_4$ (147 mAh g^{-1})	93	70/65	S21
PVdF-HFP /PU/PMMA/SiO_2	10 C	13	$LiFePO_4$ (170 mAh g^{-1})	91	137/125	S22
PVdF-HFP /Epoxy resin	20 C	6	$LiFePO_4$ (170 mAh g^{-1})	91	80/73	S23

PTFE: polytetrafluoroethylene; PU: polyurethane; PMMA: Poly(methyl methacrylate)

References for Table 5.2.

(S21) J. Chai, J. Zhang, P. Hu, J. Ma, H. Du, L. Yue, J. Zhao, H. Wen, Z. Liu, G. Cui and L. Chen, *J. Mater. Chem. A* 2016, **4**, 5191-5197.

(S22) Z. He, Q. Cao, B. Jing, X. Wang and Y. Deng, *RSC Adv.* 2017, **7**, 3240-3248.

(S23) Q. Lu, Y.-B. He, Q. Yu, B. Li, Y. V. Kaneti, Y. Yao, F. Kang and Q.-H. Yang, *Adv. Mater.* 2017, 1604460.

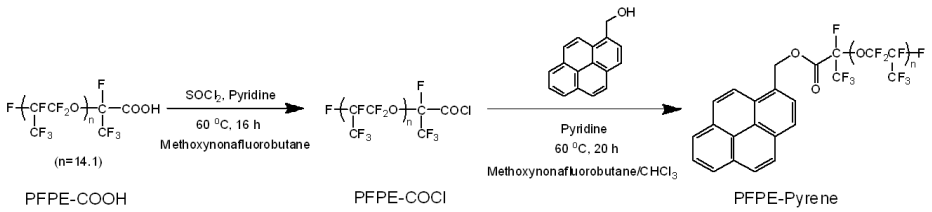

Figure 5.1. Synthesis of PFPE-Pyrene.

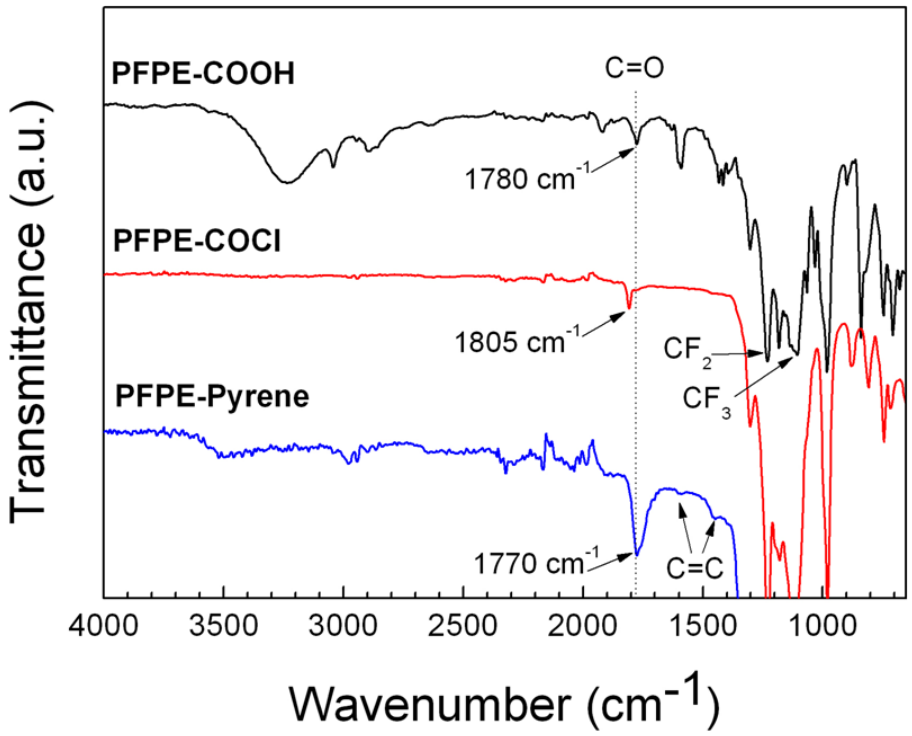

Figure 5.2. FT-IR spectra of PFPE-COOH, PFPE-COCl, and PFPE-Pyrene.

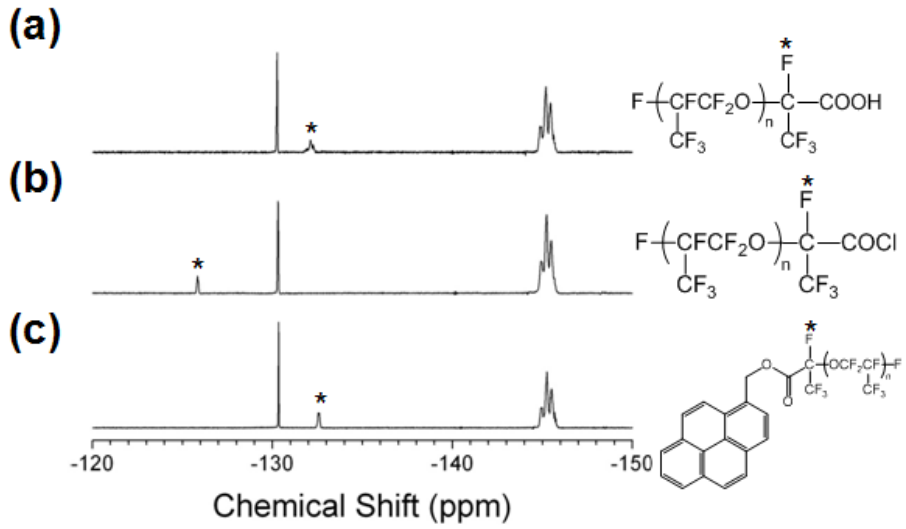

Figure 5.3. ^{19}F-NMR spectra of PFPE-COOH, PFPE-COCl, and PFPE-Pyrene.

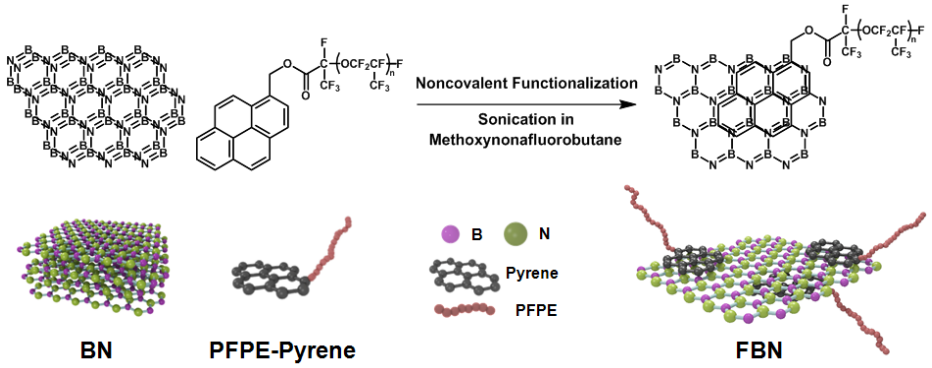

Figure 5.4. Preparation of FBN *via* sonication-assisted noncovalent functionalization.

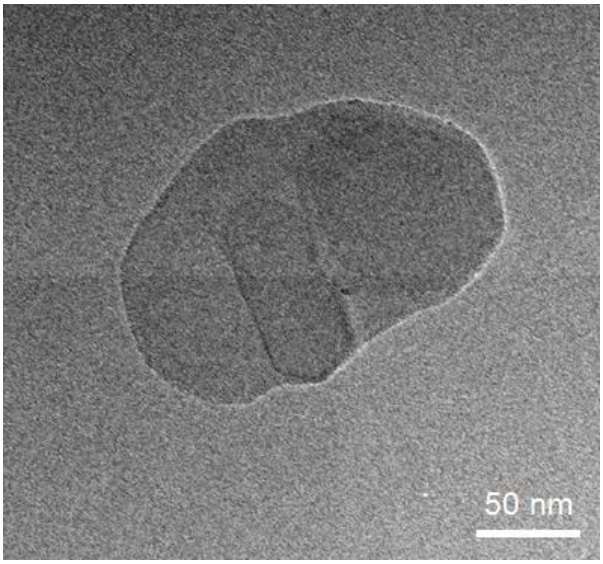

Figure 5.5. HR-TEM image of BN.

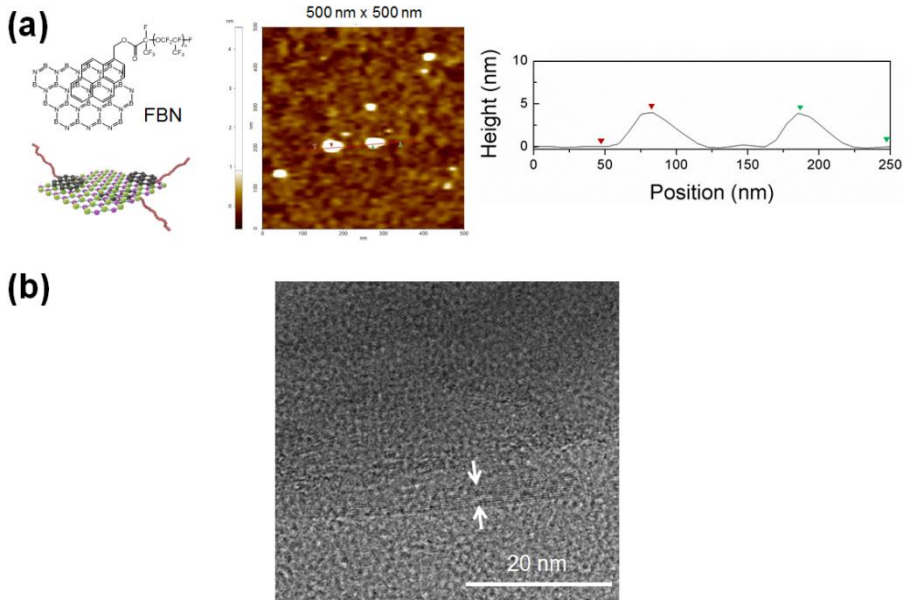

Figure 5.6. (a) AFM topography image and line-scan profile and (b) HR-TEM image of FBN.

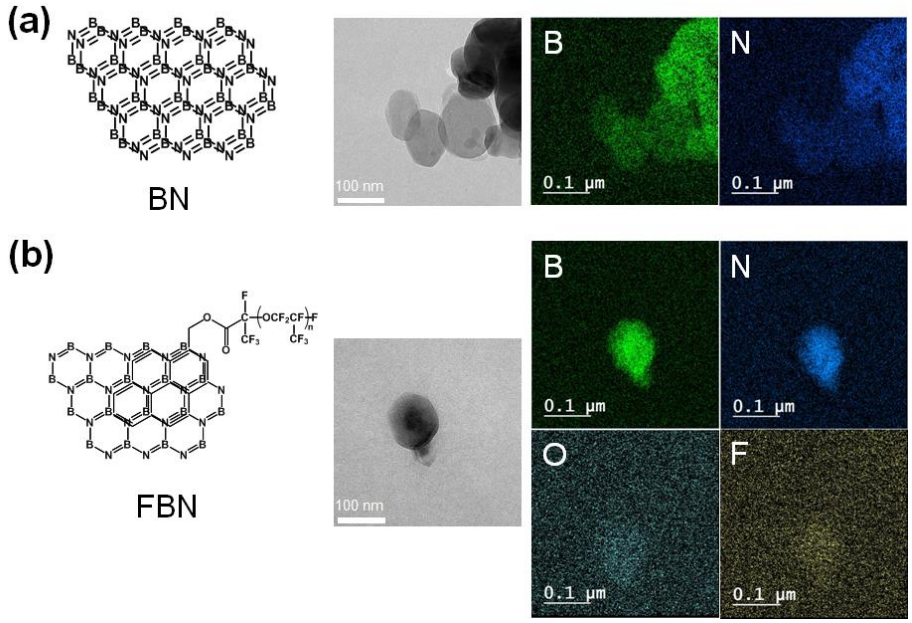

Figure 5.7. TEM images and electron energy loss spectra of (a) BN and (b) FBN.

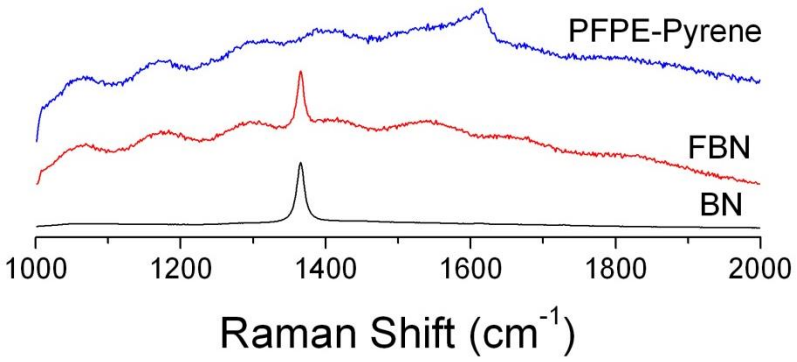

Figure 5.8. Raman spectra of BN, FBN, and PFPE-Pyrene.

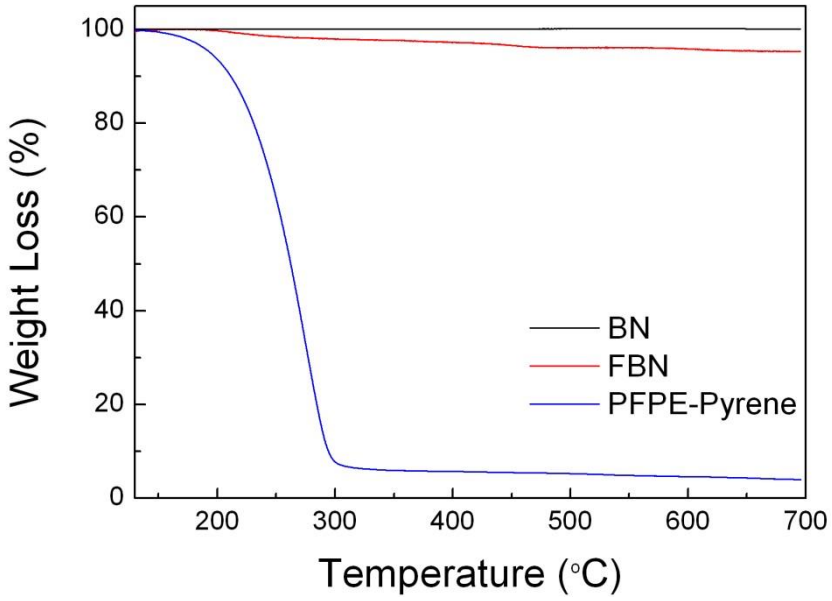

Figure 5.9. TGA profiles of BN, FBN, and PFPE-Pyrene.

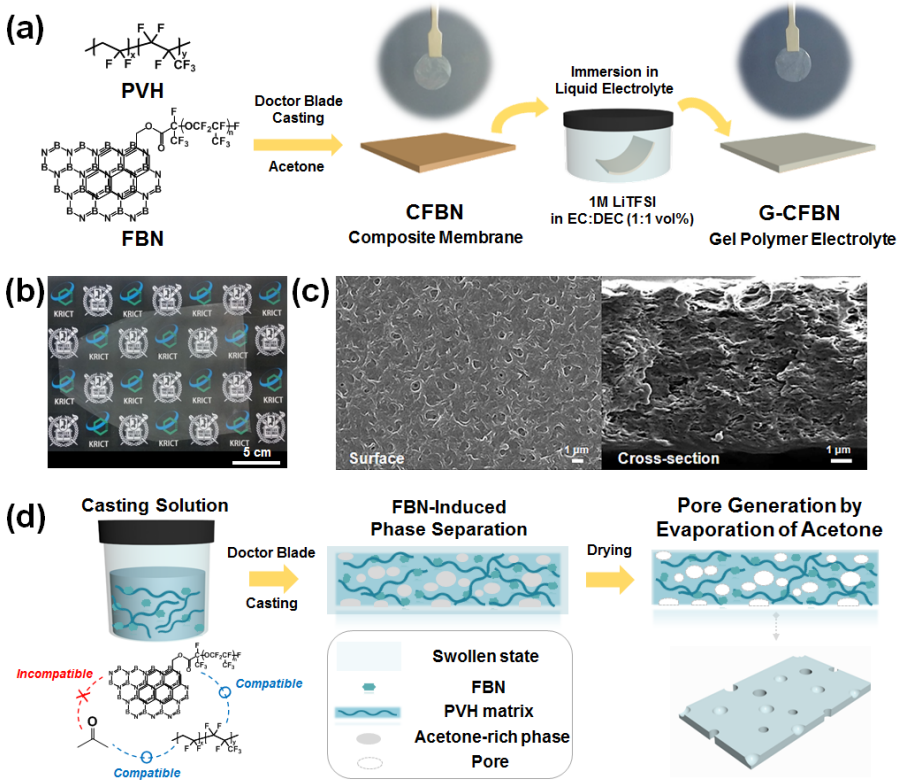

Figure 5.10. (a) Schematic illustration of the overall procedure for preparation of G-CFBN, (b) photograph of CFBN (0.5 wt% FBN), (c) surface (left) and cross-sectional (right) SEM images of CFBN (0.5 wt% FBN), and (d) suggested mechanism on autonomous pore formation of CFBN by FBN-induced phase separation.

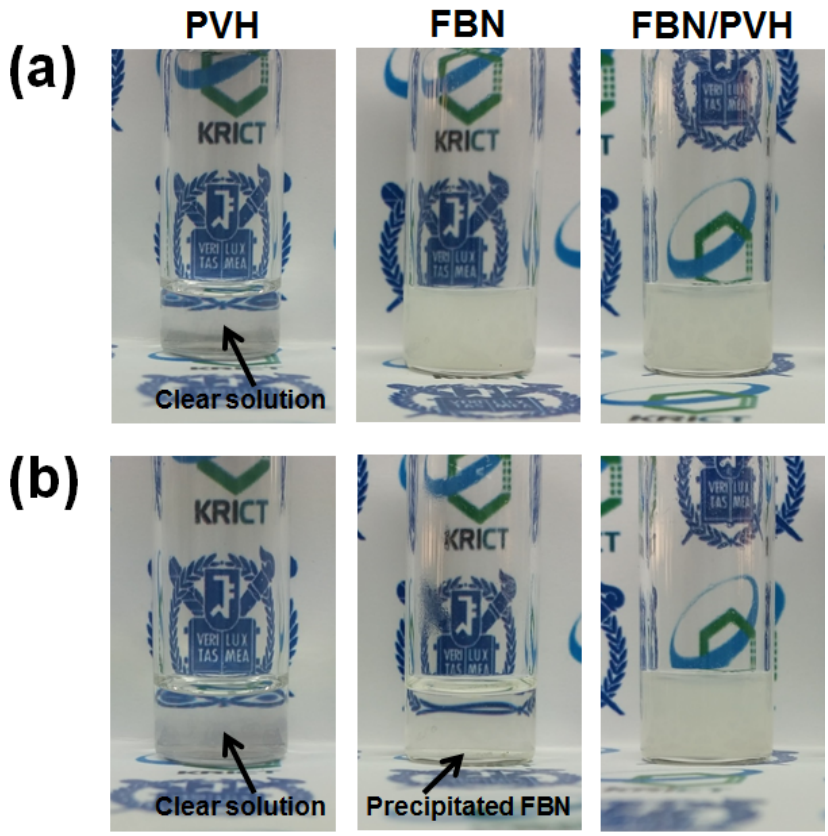

Figure 5.11. Dispersion state of PVH, FBN, and FBN/PVH (left to right) in acetone (a) right after sonication and (b) after 1 h.

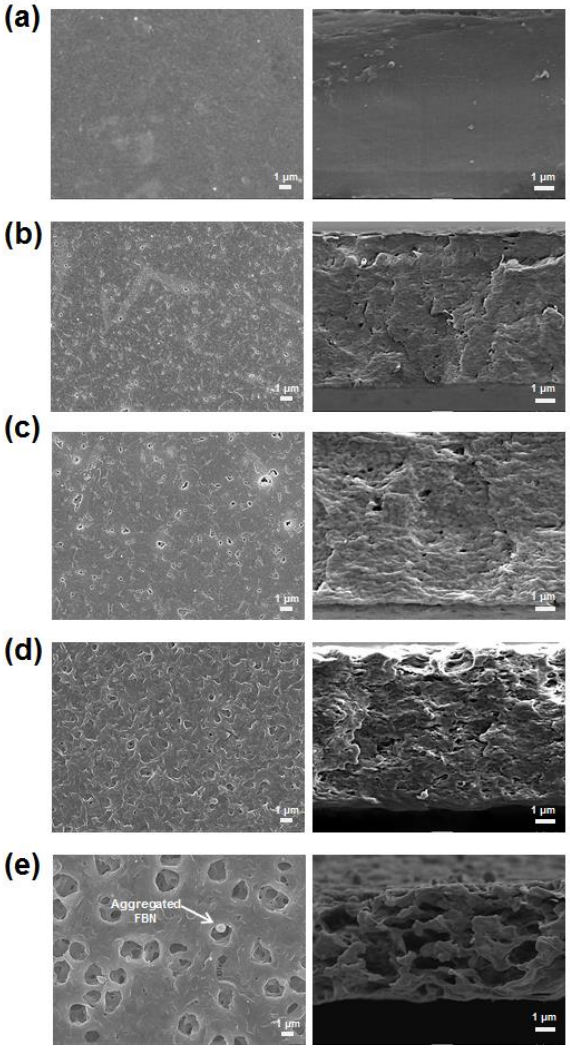

Figure 5.12. Surface (left) and cross-sectional (right) SEM images of (a) PVH, and CFBNs with (b) 0.1 wt%, (c) 0.2 wt%, (d) 0.5 wt%, and (e) 1.0 wt% of FBN.

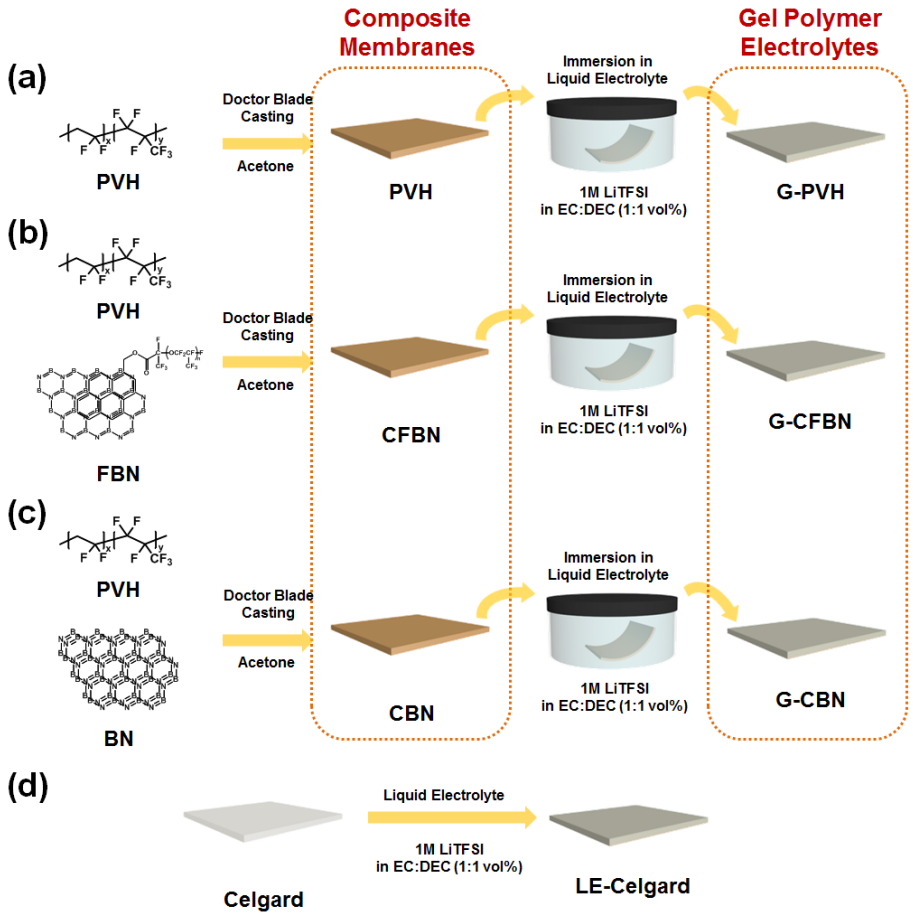

Figure 5.13. Schematic illustration of preparation of (a) G-PVH, (b) G-CFBN, (c) G-CBN, and (d) LE-Celgard.

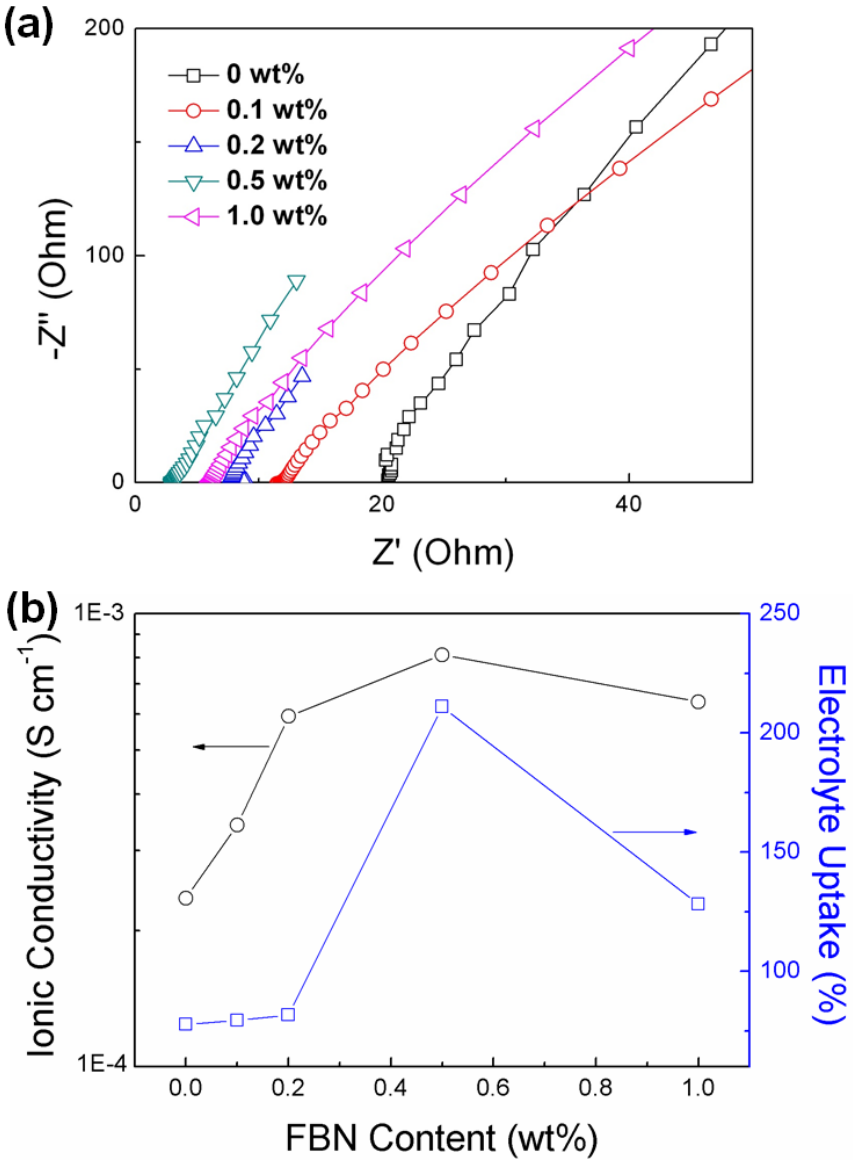

Figure 5.14. (a) Electrochemical impedance spectra and (b) ionic conductivities of G-CFBNs with 0, 0.1, 0.2, 0.5, and 1.0 wt% of FBN.

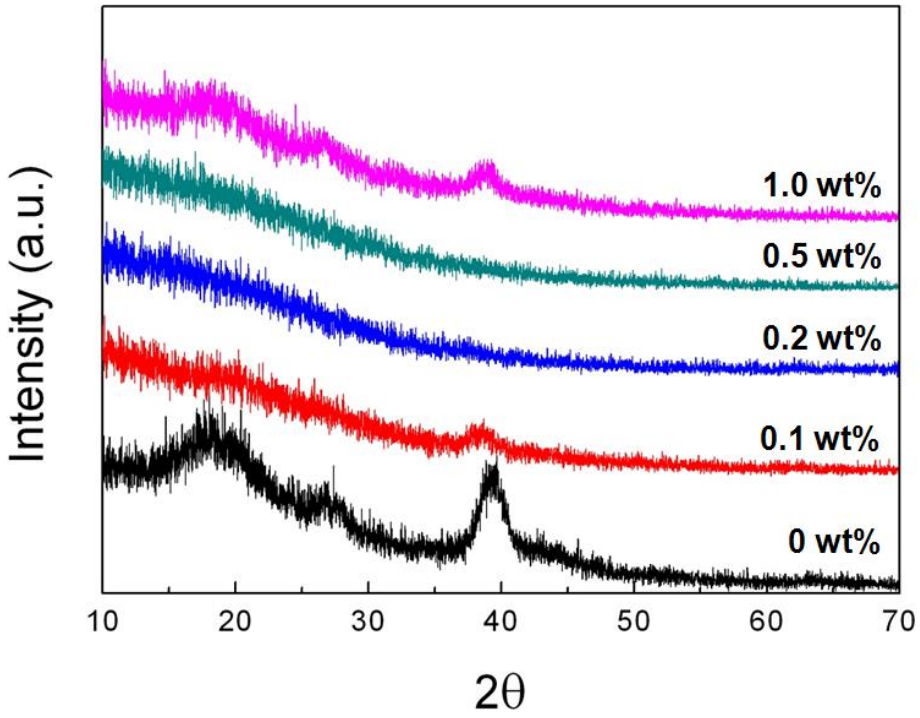

Figure 5.15. XRD patterns of CFBNs with 0, 0.1, 0.2, 0.5, and 1.0 wt% of FBN.

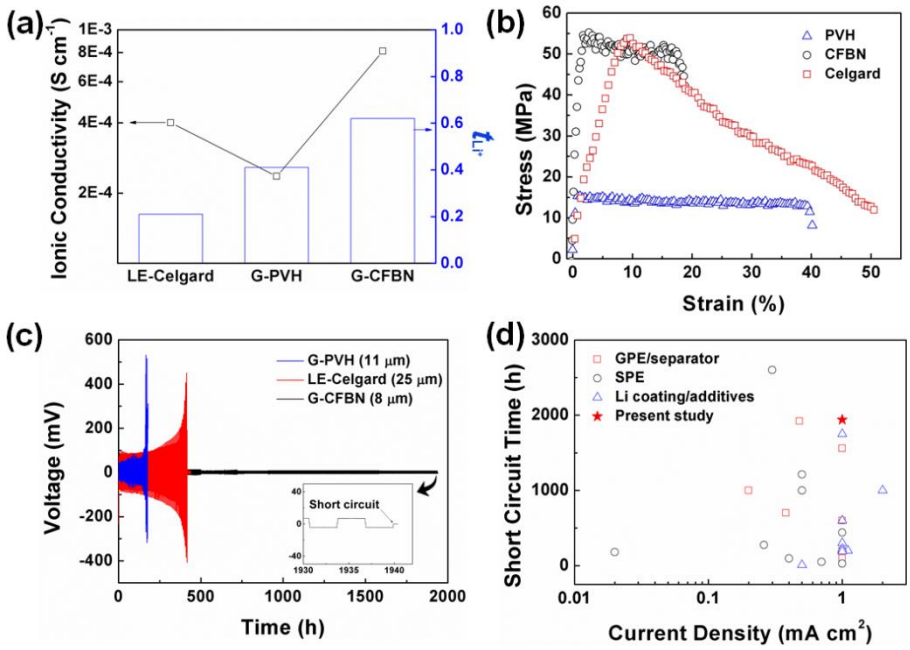

Figure 5.16. (a) Ionic conductivity and Li^+ transference number (t_{Li+}) of LE-Celgard, G-PVH, and G-CFBN at 25 ^oC, (b) Stress-strain curves of PVH, CFBN, and Celgard, (c) galvanostatic cycling profiles of symmetric Li/Li cells with LE-Celgard, G-PVH, and G-CFBN at a current density of 1.0 mA cm^{-2} at 25 ^oC, and (d) short circuit time of G-CFBN compared with other state of the art dendrite-suppressing strategies at various current densities.

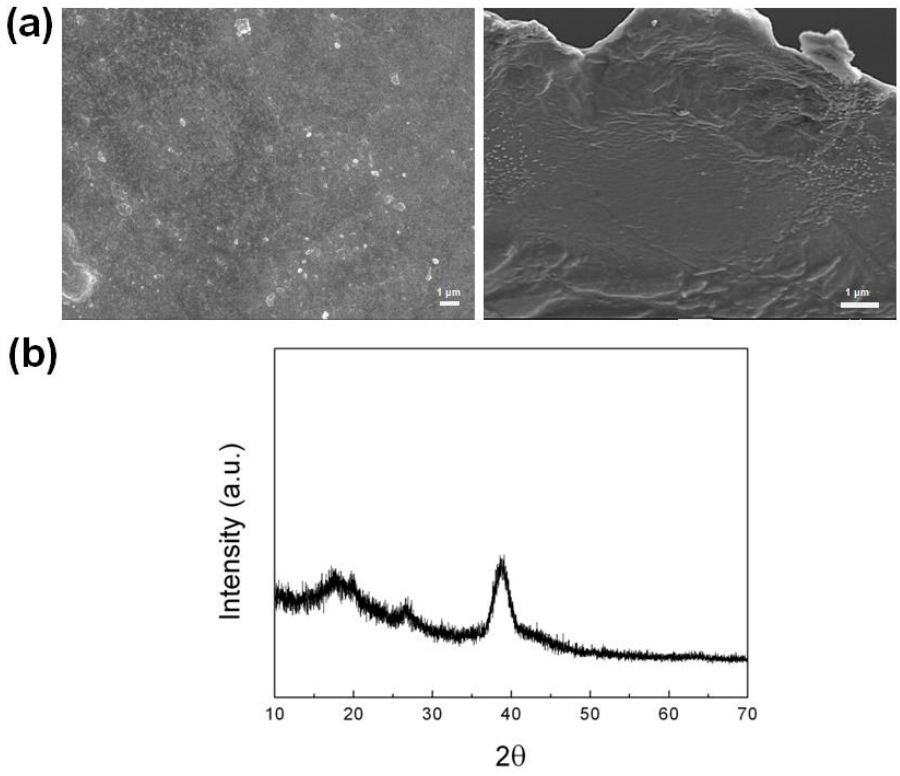

Figure 5.17. (a) Surface (left) and cross-sectional (right) SEM images and (b) XRD pattern of CBN with 0.5 wt% of BN.

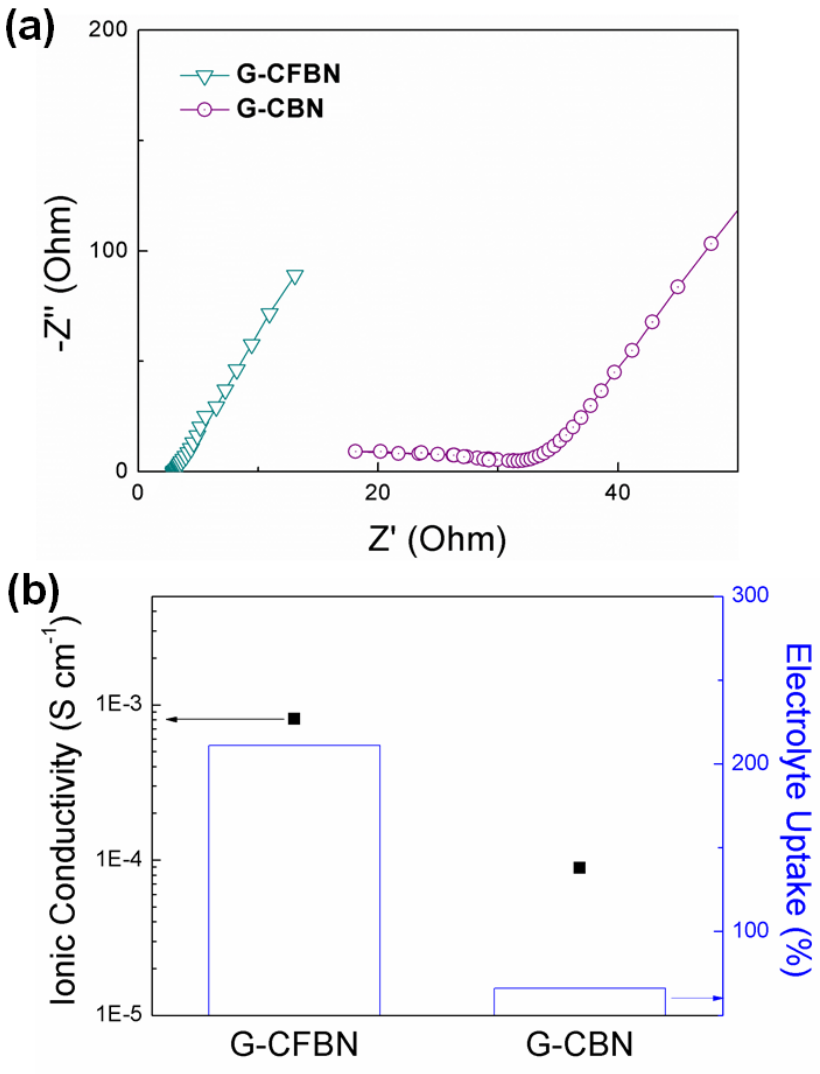

Figure 5.18. (a) Electrochemical impedance spectra and (b) ionic conductivity and electrolyte uptake values of G-CFBN and G-CBN.

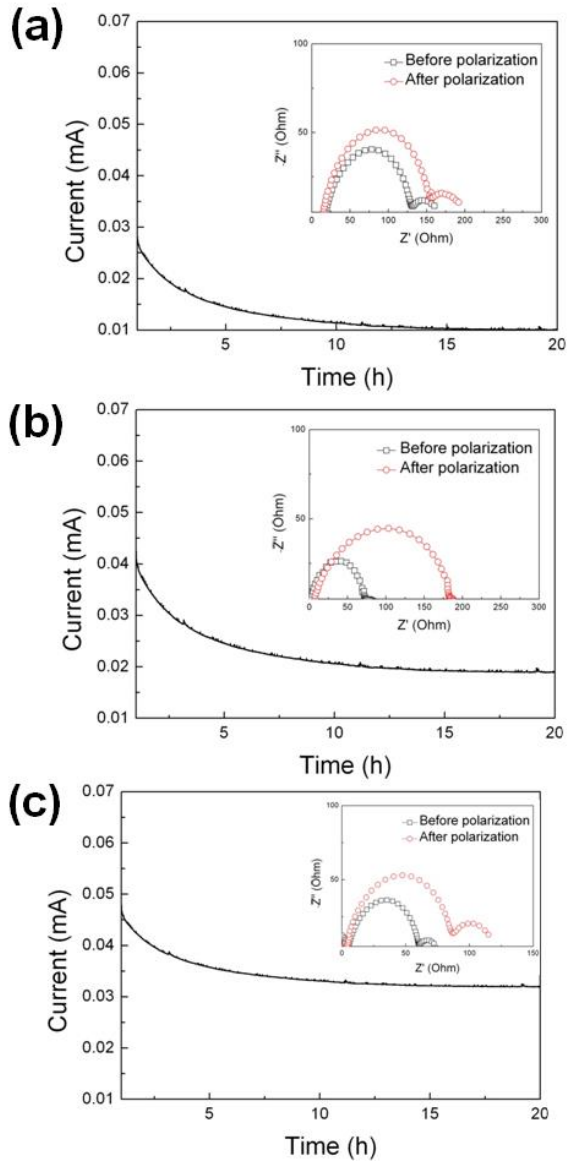

Figure 5.19. Chronoamperometric curves of Li/electroltyes/Li cells, where the electrolytes are (a) LE-Celgard, (b) G-PVH, and (c) G-CFBN, respectively.

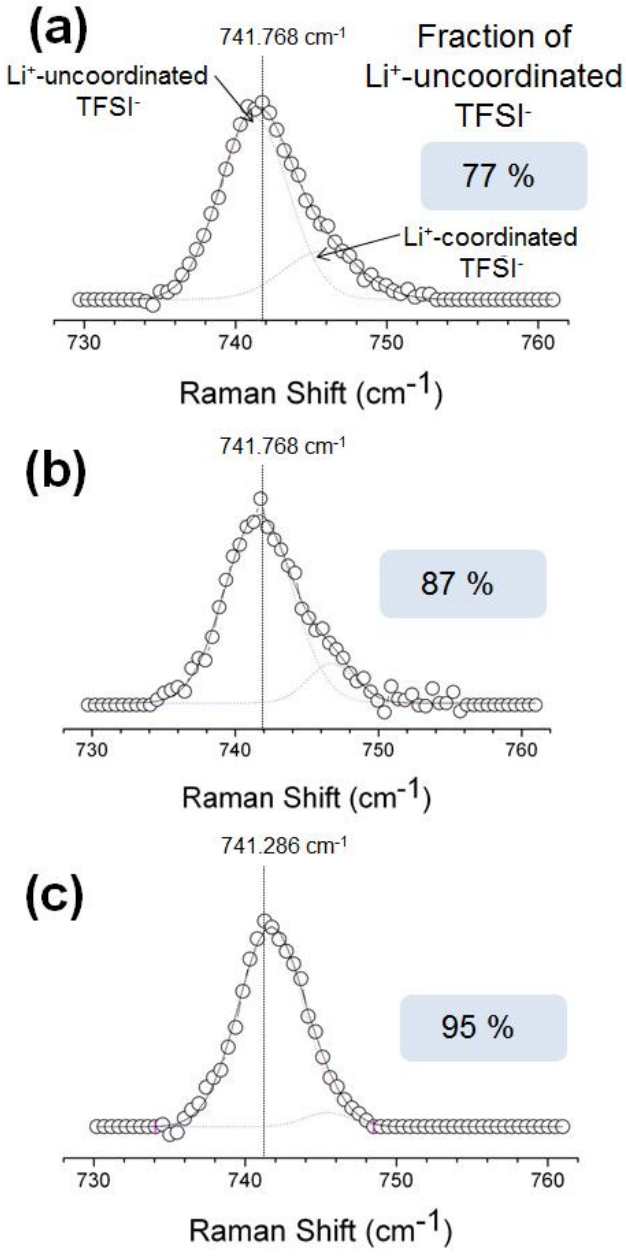

Figure 5.20. Raman spectra of (a) LE-Celgard, (b) G-PVH, and (c) G-CFBN.

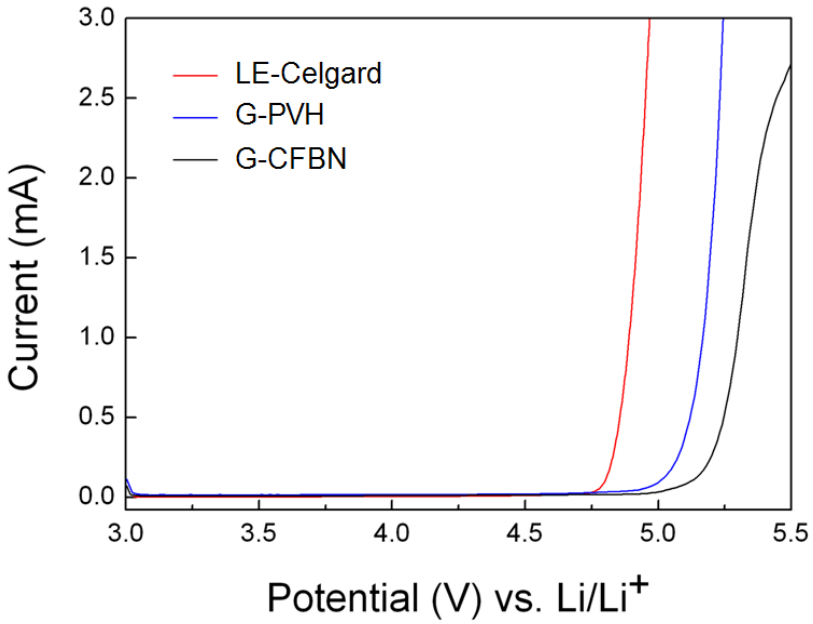

Figure 5.21. Linear sweep voltammograms of LE-Celgard, G-PVH, and G-CFBN at 25 ^{o}C (scan rate: 1.0 mV s^{-1}).

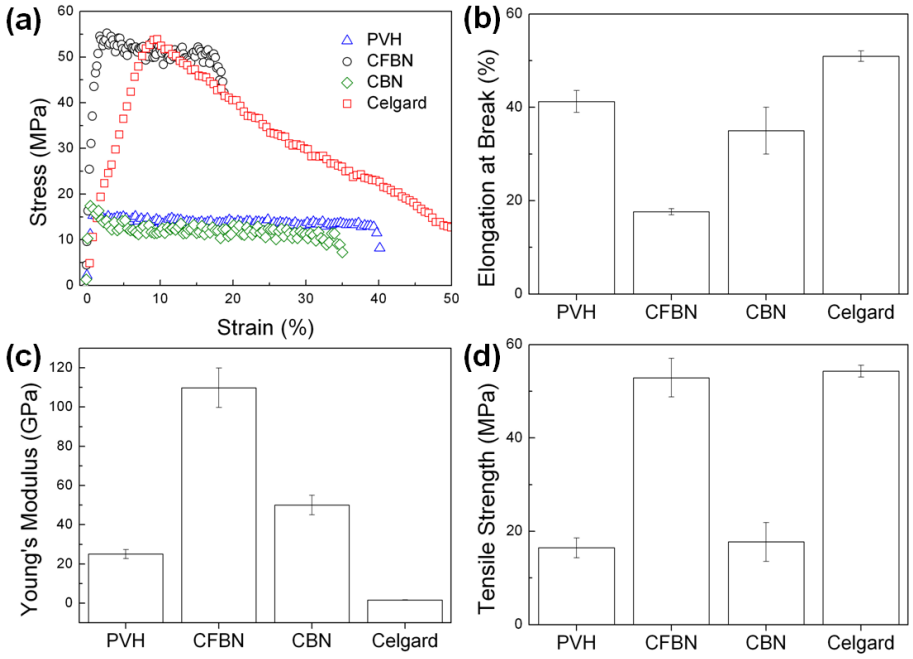

Figure 5.22. UTM results of PVH, CFBN, CBN, and Celgard. (a) Stress-strain curves, (b) elongation at break, (c) Young's modulus, and (d) tensile strength.

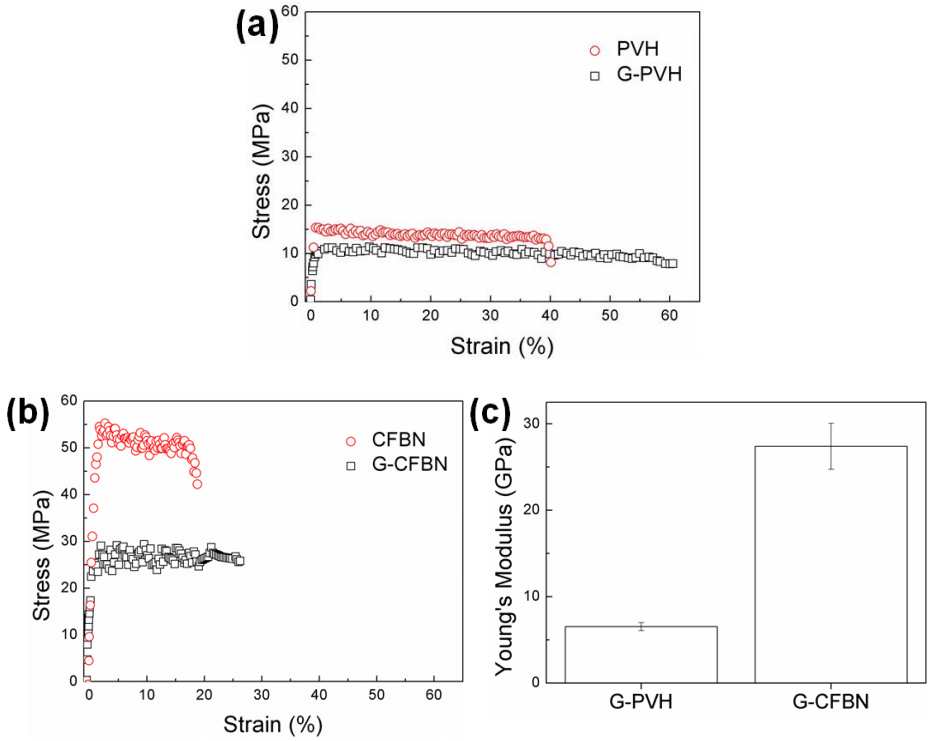

Figure 5.23. Stress-strain curves of (a) PVH/G-PVH and (b) CFBN/G-CFBN and (c) Young's modulus of G-PVH and G-CFBN, where electrolyte uptake of G-PVH and G-CFBN is controlled as 60 %.

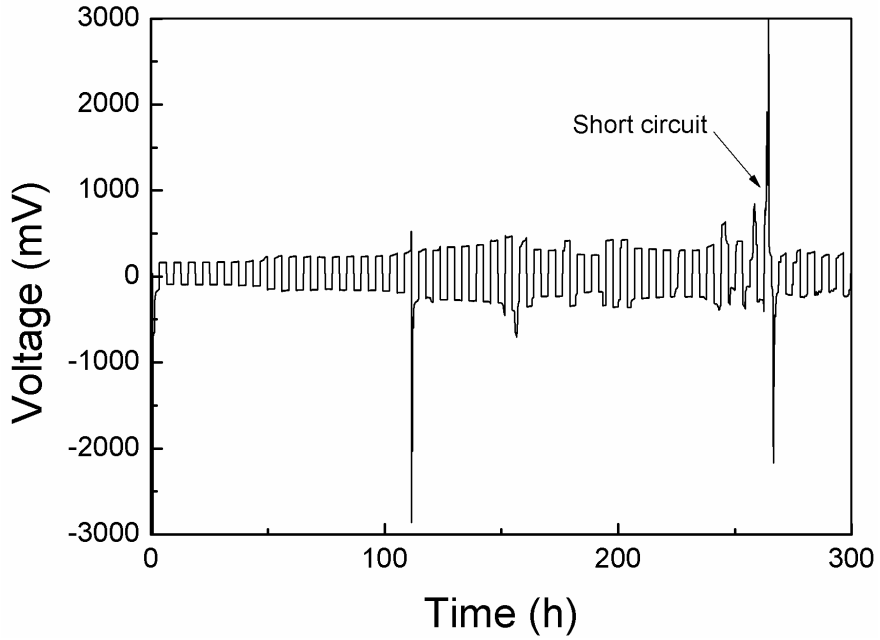

Figure 5.24. Galvanostatic cycling profiles of symmetric Li/Li cells with G-PVH (thickness = 24 um) at a current density of 1.0 mA cm^{-2} at 25 ^{o}C.

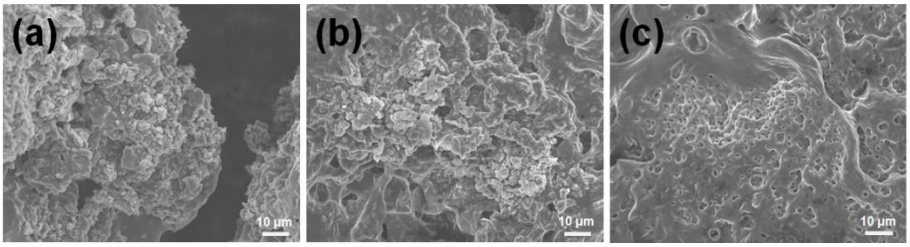

Figure 5.25. SEM images of Li metal surface of Li/electrolytes/Li cells after short circuit in galvanostatic cycling test at a current density of 1.0 mA cm^{-2} at 25 ^{o}C, where the electrolytes are (a) G-PVH, (b) LE-Celgard, and (c) G-CFBN.

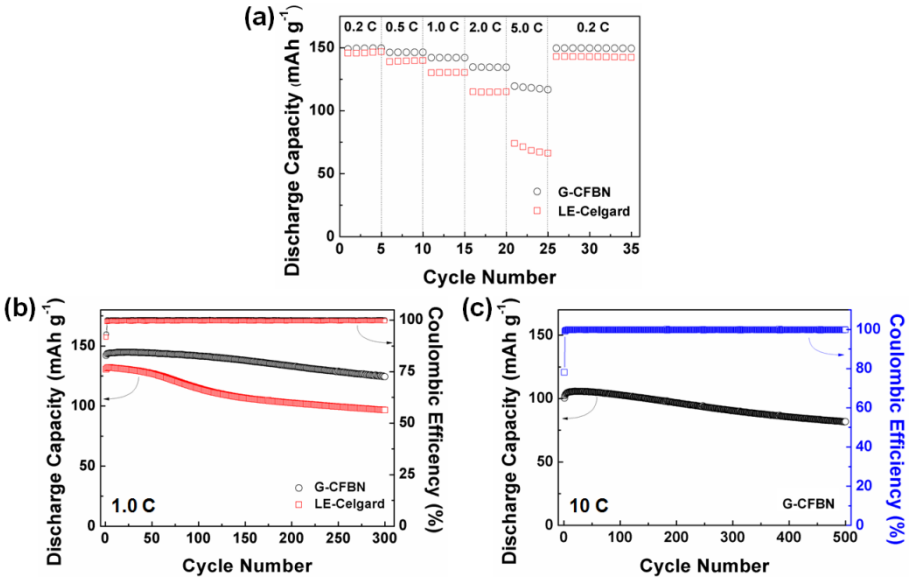

Figure 5.26. Electrochemical performance of Li/electrolyte/$LiFePO_4$ cells cycled at 25 ^{o}C, where the electrolytes are G-CFBN and LE-Celgard. (a) Rate capability of the cells at various C-rates, (b) long-term cycling performance of the cells at 1.0 C, and (c) long-term cycling performance of the cell with G-CFBN at 10 C.

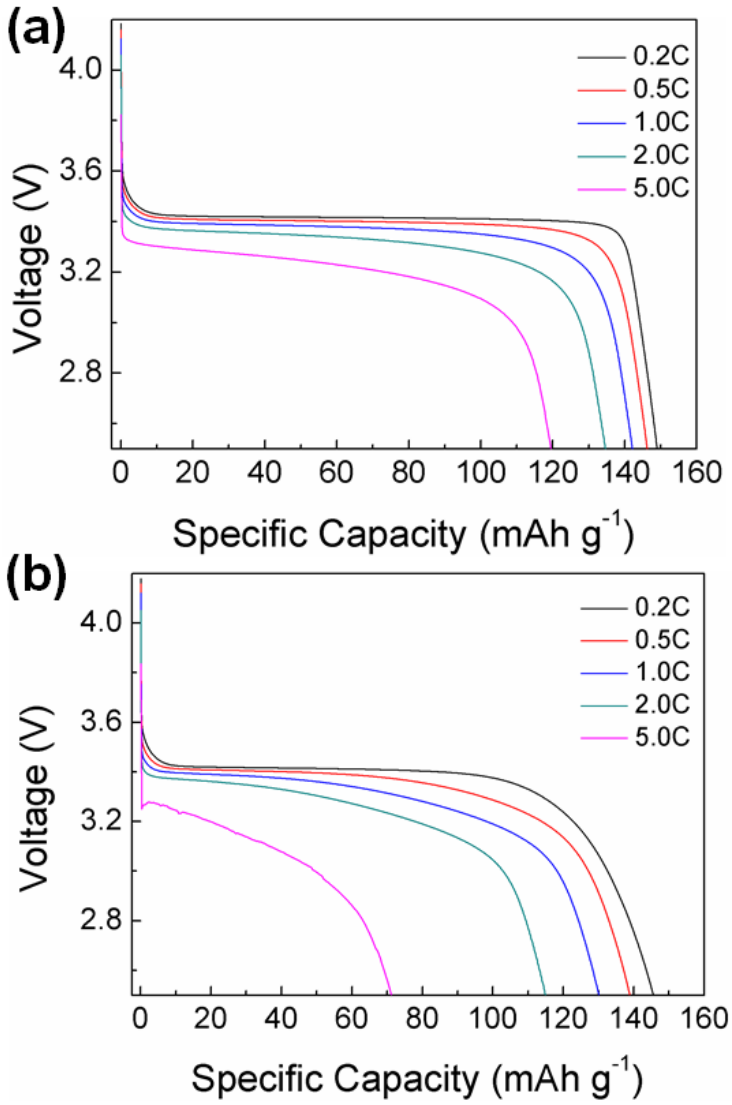

Figure 5.27. Voltage-discharge capacity curves of Li/electrolytes/$LiFePO_4$ cells cycled at 25 ^{o}C with various C-rates, where the electrolytes are (a) G-CFBN and (b) LE-Celgard.

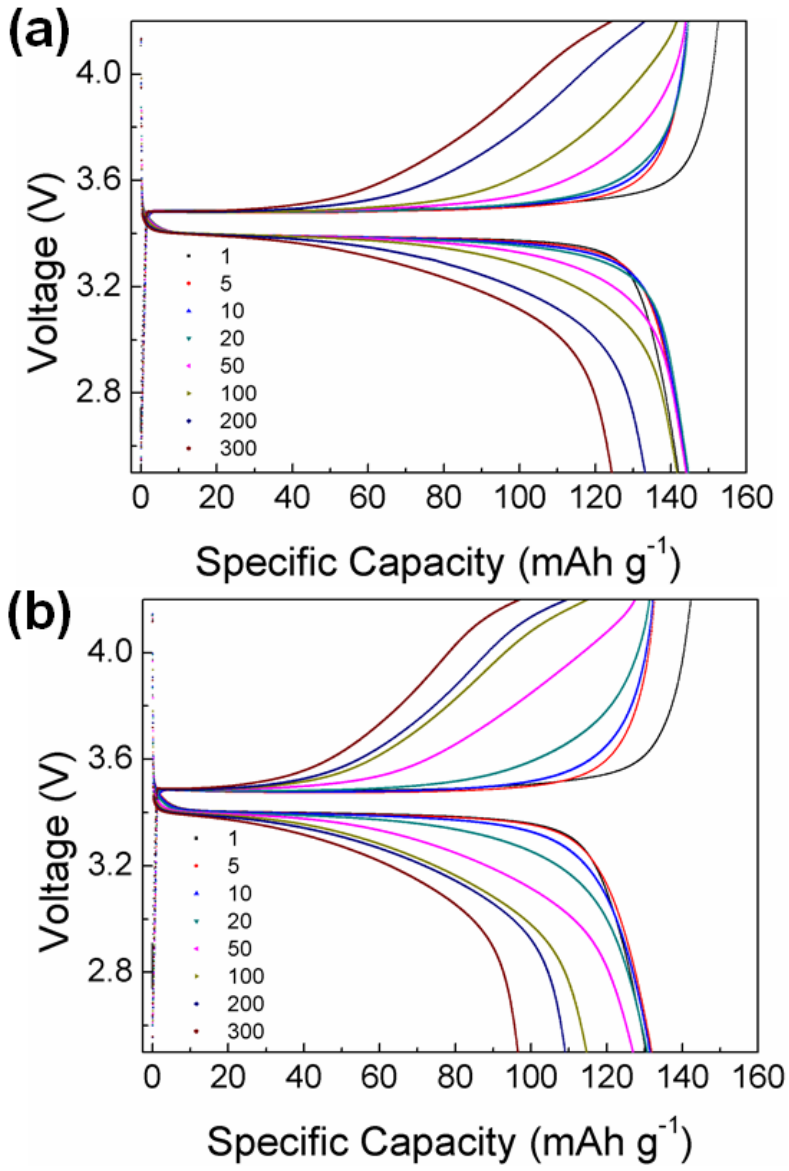

Figure 5.28. Voltage-capacity curves of Li/electrolytes/$LiFePO_4$ cells cycled at 25 ^{o}C with 1.0 C, where the electrolytes are (a) G-CFBN and (b) LE-Celgard.

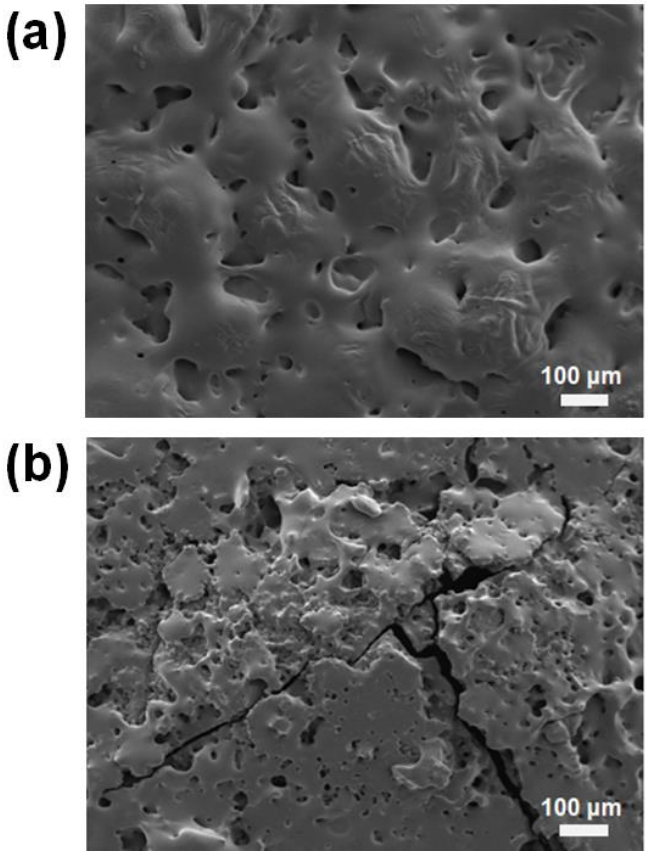

Figure 5.29. SEM images of Li metal surface of Li/electrolytes/$LiFePO_4$ cells cycled at 25 ^{o}C with 1.0 C after 300 cycles, where the electrolytes are (a) G-CFBN and (b) LE-Celgard.

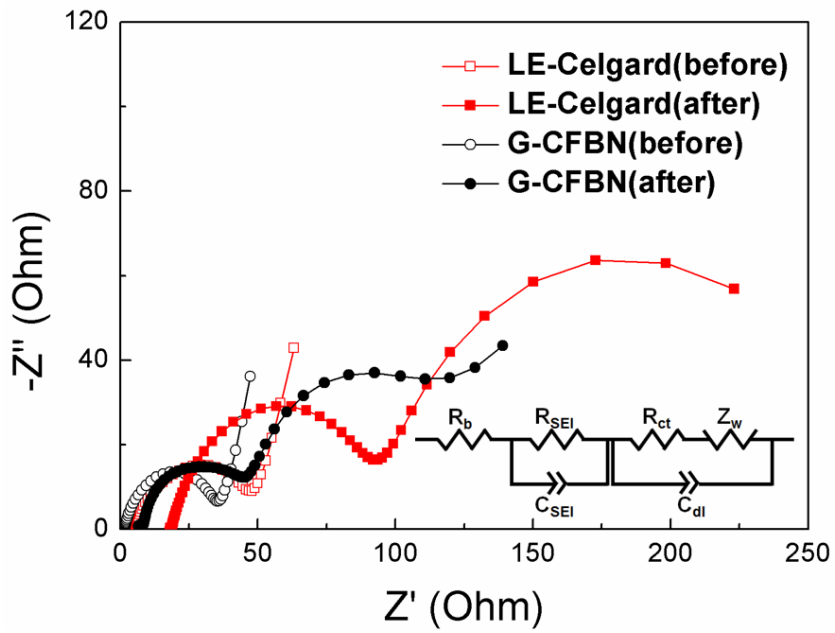

Figure 5.30. Electrochemical impedance spectra of Li/electrolytes/$LiFePO_4$ cells cycled at 25 ^{o}C with 1.0 C before and after 300 cycles, where the electrolytes are G-CFBN and LE-Celgard.

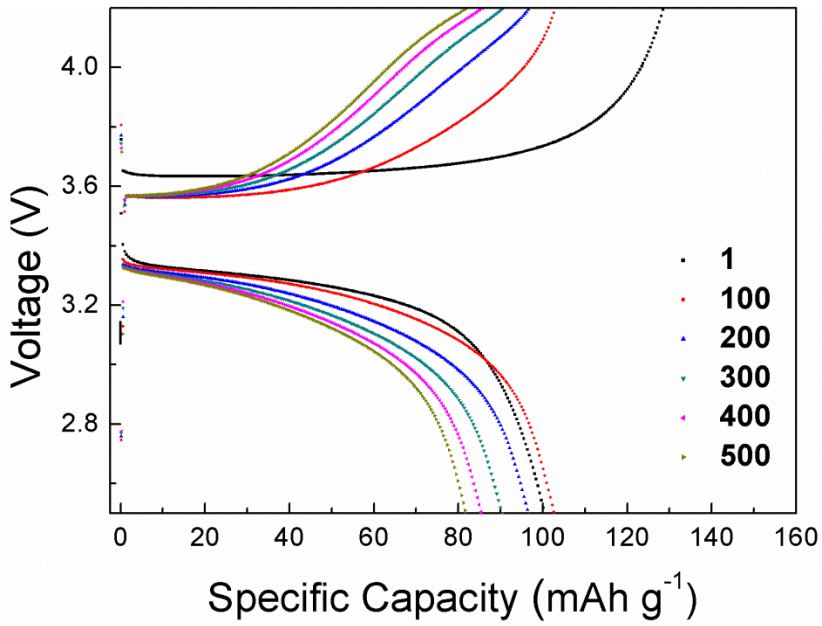

Figure 5.31. Voltage-capacity curves of Li/G-CFBN/$LiFePO_4$ cell cycled at 25 ^{o}C with 10 C.

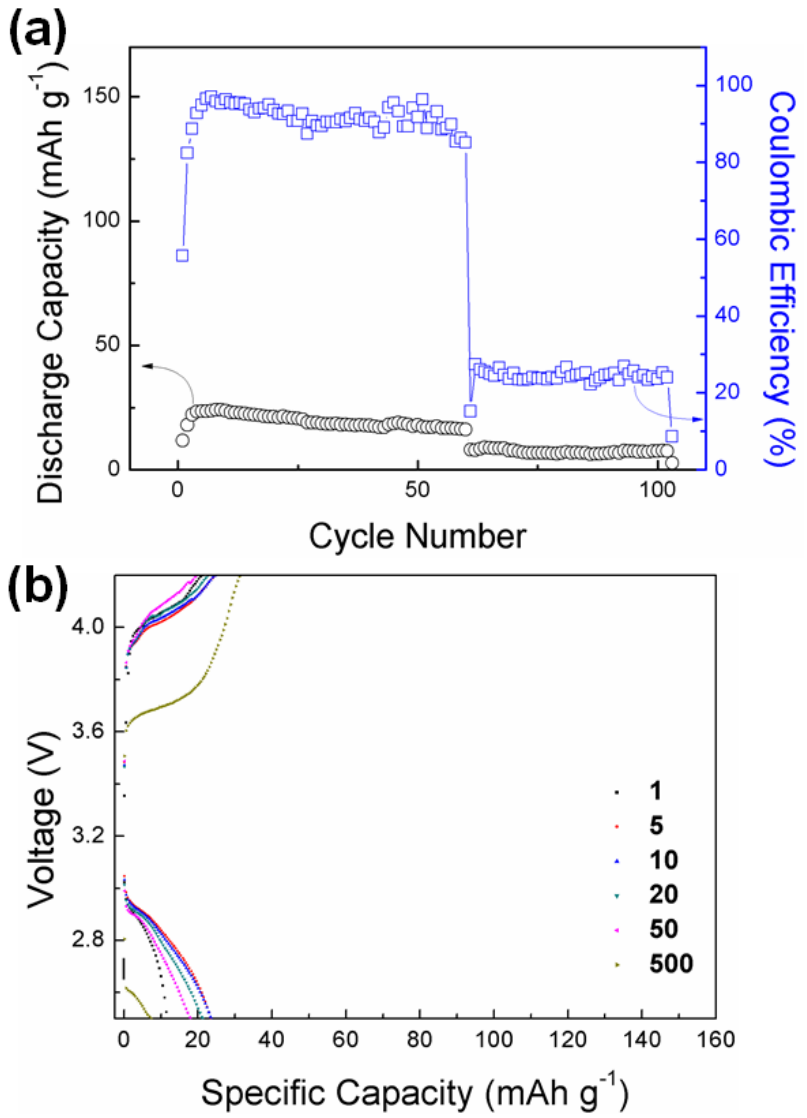

Figure 5.32. (a) Long-term cycling performance and (b) voltage-capacity curves of Li/LE-Celgard/$LiFePO_4$ cell cycled at 25 ^{o}C with 10 C.

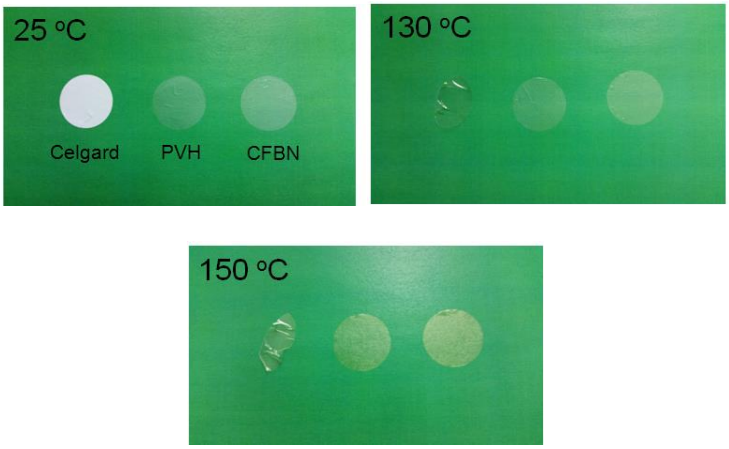

Figure 5.33. Thermal stability of Celgard, PVH, and CFBN at 25 ^{o}C, 130 ^{o}C, and 150 ^{o}C.

초 록

본 논문은 이온 전도성 고분자와 다기능성 충진제의 합성과 분석 및 리튬 이차 전지용 고분자 전해질로의 응용에 대하여 기술하였다. 첫째, 가역적 첨가−분절 연쇄이동 (Reversible addition–fragmentation chain transfer, RAFT) 중합법을 이용하여 폴리에틸렌글리콜 메틸 에테르 메타크릴레이트 (PEGMA)와 폴리헤드랄 올리고머릭 실세스퀴옥산 (POSS) 기반 단량체로 구성된 유/무기 복합 가지형 공중합체를 합성하고, 이를 고체상 고분자 전해질로 응용하였다. 대조군으로서 같은 구성의 선형 공중합체를 합성하여 고분자의 구조가 물리적, 전기화학적 특성에 미치는 영향을 분석하였다. POSS의 우수한 기계적 강화 특성으로 인하여 고온에서도 전해질의 안정성과 기계적 강도가 유지되었다. 해당 유/무기 복합 가지형 공중합체에 기반한 고체상 고분자 전해질은 같은 구성의 선형 공중합체보다 약 3 배 가량 높은 이온 전도도 (1.6×10^{-4} S/cm, 60 °C)를 보였는데, 이는 가지형 구조로 인해 생성되는 자유 부피로 인하여 고분자 사슬의 유동성이 향상되기 때문이다.

둘째, 산 촉매 기반 가수분해/축합 반응을 이용하여 이온

전도성 폴리에틸렌글리콜을 함유하는 가지형 폴리실록산(polysiloxane)을 합성하고, 이를 싸이올-엔 클릭 반응을 이용하여 자연 유래 테르펜 (terpene) 중 리모넨(limonene)과 제라니올 (geraniol)로 가교한 고체상 고분자 전해질을 제조하였다. 테르펜 가교제의 구조, 전해질의 물리적 상태 및 리튬 금속 음극의 형상이 다양한 전기 화학적 특성에 미치는 영향을 분석하였다. 선형의 제라니올 가교제가 도입된 전해질의 이온 전도도가 고리형의 리모넨 가교제가 도입된 전해질의 이온 전도도보다 더 높았고, 이는 고리형 구조의 가교제가 입체 장애 및 고리 스트레인 (ring strain)이 더 큰 것에서 기인한다. 이러한 고체상 고분자 전해질과 리튬 파우더 음극의 조합으로 수지상 리튬의 성장이 저해되어 우수한 전지 성능을 구현할 수 있었다.

셋째, 이온 전도성 폴리에틸렌글리콜과 음이온을 트랩(trap)하는 붕소 작용기를 함유하는 코어-쉘 (Core-shell) 구조의 실리카 입자를 제조하고 이를 고체상 고분자 전해질의 충진제 (filler)로 이용하였다. 충진제의 양과 붕소의 존재 여부가 전해질의 다양한 물리적, 전기 화학적 특성에 미치는 영향을 분석하였다. 해당 코어-쉘 실리카 충진제는 전해질의 기계적 강도와 열적 안정성을 향상시켰다. 쉘에 포함된 붕소는

이온 전도도와 리튬 이온 운반율을 모두 향상시켰고, 이는 음이온을 트랩하는 붕소가 리튬염의 해리도를 증가시켰기 때문이다. 전해질에 분산되어 있는 실리카 충진제가 계면 부반응을 방지하는 보호층 역할을 하여 리튬 금속 음극과의 계면 적합성도 개선 되었다.

넷째, 초음파 분산 기반의 비공유결합 개질 (Sonication-assisted noncovalent functionalizatoni) 방법을 이용하여 과불소폴리에테르 (Perfluoropolyether, PFPE)로 개질된 이차원의 질화붕소 (Boron nitride, BN)를 합성하고 이를 겔 고분자 전해질을 위한 다기능성 충진제로 사용하였다. 전해질 성분인 고분자, 충진제, 용매간의 상분리로 인해 포로젠 (porogen)이나 비용매 없이도 자동적으로 기공이 형성되었다. 소량 (0.5 wt%)의 충진제의 도입만으로도 충진제가 없는 겔 고분자 전해질 및 상용화된 폴리올레핀 기반 분리막보다 우수한 이온 전도도, 리튬 이온 운반율 및 기계적 강도를 보였다. 또한, 해당 첨가제의 도입으로 인한 기계적 강도와 전기 화학적 특성의 향상으로 인해 수지상 리튬의 성장이 효과적으로 억제되었고, 이는 전지 성능의 향상으로 이어졌다. 해당 충진제를 함유하는 겔 고분자 전해질은 높은 전류 밀도 (1 mA cm^{-2})에서도 1940 시간 정도의 전례 없는 긴 단락

시간을 보였다.

주요어: 리튬 이차 전지, 고체상 고분자 전해질, 겔 고분자 전해질, 가역적 첨가-분절 연쇄이동, 폴리헤드랄 올리고머릭 실세스퀴옥산, 테르펜, 싸이올-엔 클릭 반응, 수지상 리튬, 코어-쉘 실리카, 붕소, 질화붕소

학 번: 2013-30986